Spring 2021

Fabrication of 304L stainless steel and aluminum parts by laser foil printing and process automation

Chia-Hung Hung

Department: Mechanical and Aerospace Engineering

FABRICATION OF 304L STAINLESS STEEL AND ALUMINUM PARTS BY LASER FOIL PRINTING AND PROCESS AUTOMATION

by

CHIA-HUNG HUNG

A DISSERTATION

Presented to the Graduate Faculty of the

MISSOURI UNIVERSITY OF SCIENCE AND TECHNOLOGY

In Partial Fulfillment of the Requirements for the Degree

DOCTOR OF PHILOSOPHY

in

MECHANICAL ENGINEERING

2021

Approved by:

Ming C. Leu, Advisor
Frank Liou
K. Chandrashekhara
Heng Pan
Ronald J. O'Malley

PUBLICATION DISSERTATION OPTION

This dissertation consists of the following four articles, formatted in the style used by the Missouri University of Science and Technology:

Paper I, "Enhanced Mechanical Properties for 304L Stainless Steel Parts Fabricated by Laser-Foil-Printing Additive Manufacturing", was published in Journal of Manufacturing Processes", and can be found on pages 11-33.

Paper II, "Aluminum Parts Fabricated by Laser-Foil-Printing Additive Manufacturing: Processing, Microstructure, and Mechanical Properties", was published in *Materials* and can be found on pages 34-55.

Paper III, "The Effect of Laser Welding Modes on Mechanical Properties and Microstructure of 304L Stainless Steel Parts Fabricated by Laser-Foil-Printing Additive Manufacturing", was published in International *Journal of Advanced Manufacturing Technology* and can be found on pages 56-80.

Paper IV, "Development and Experimental Study of an Automated Laser-Foil-Printing Additive Manufacturing System", has been submitted to CIRP Annals Manufacturing Technology and can be found on pages 81-98.

ABSTRACT

This work presents research conducted on a novel metal additive manufacturing process, called Laser Foil Printing (LFP), to fabricate metal parts with various geometries layer by layer using metal foil as the feedstock. To investigate the processability and characteristics of LFP for fabricating metal parts, the materials included 304L stainless steel and Al-1100 aluminum alloy. The LFP process parameter windows for both 304L and Al-1100 were determined, and the optimal process parameters with stable formation of the melt pools were selected to fabricate dense metal parts. The microstructure and properties of LFP-fabricated parts were characterized and analyzed using tensile testing, scanning electron microscopy, electron backscattered diffraction, and ANOVA analysis. The mechanical properties of fabricated parts were compared with those of parts fabricated by the Laser Powder Bed Fusion (L-PBF) process. The results showed that the 304L parts fabricated by LFP were 10-20% higher in strength and ductility than those fabricated by L-PBF due to the finer grains formed by faster cooling in LFP. Also, oxidation in LFP-fabricated parts was less compared with that in L-PBF fabricated parts because of smaller surface area in metal foil compared with metal powder. The density (> 99.3%) of Al-1100 aluminum alloy parts fabricated by LFP was much higher than the density (< 90%) of Al-1100 parts fabricated by L-PBF because of no air gaps in foil like those in powder particles. A fully automated LFP system was constructed and used to automatically fabricate 304L parts with various geometries. The parts' dimensional accuracies and their mechanical properties were measured. These parts exhibited higher tensile strength than those fabricated by other laser additive manufacturing technologies.

ACKNOWLEDGMENTS

I would like to show my highest gratitude to my advisor, Dr. Ming C. Leu, for providing me the opportunity to work on a research and development project towards the completion of my Ph.D. in Mechanical Engineering. His rigorous and passionate enthusiasm for research has significantly improved my research approach to allow me to conduct research more carefully and thoroughly to achieve success.

Besides my advisor, I am grateful to the rest of my committee: Prof. Frank Liou, Prof. K. Chandrashekhara, Prof. Heng Pan, and Prof. Ronald J. O'Malley to provide valuable and helpful suggestions for my research.

I would like to thank Dr. Hai-Lung Tsai for providing me the exchange student program to let me start my foreign research journey and provides professional suggestions and helps on my doctoral research.

I would like to thank Dr. Ming C. Leu and the Department of Mechanical Engineering at the Missouri University of Science and Technology for funding my Ph.D. in Mechanical Engineering through the Research Assistantship and Teaching Assistantship. The financial support allowed me to focus on pursuing my highest education degree and work with highly-skilled genius from all over the world.

Last but not least, I would like to dedicate this work to my family and my friends for their devoted love and resolute support when I pursued in my doctoral education. Their sacrifices and patient allowed me to focus on research and complete my doctoral degree.

TABLE OF CONTENTS

Page

PUBLICATION DISSERTATION OPTION iii

ABSTRACT iv

ACKNOWLEDGMENTS v

LIST OF ILLUSTRATIONS x

LIST OF TABLES xiv

SECTION

1. INTRODUCTION 1

1.1. BACKGROUND AND MOTIVATION 1

1.2. METAL ADDITIVE MANUFACTURING 3

1.2.1. Additive Manufacturing of Stainless Steel 3

1.2.2. Additive Manufacturing of Aluminum Alloys. 5

1.2.3. Laser Welding Modes in Additive Manufacturing 6

1.3. RESEARCH OBJECTIVES 7

1.4. SCIENTIFIC AND TECHNICAL CONTRIBUTIONS 8

1.5. ORGANIZATION OF DISSERTATION 9

PAPER

I. ENHANCED MECHANICAL PROPERTIES FOR 304L STAINLESS STEEL PARTS FABRICATED BY LASER-FOIL-PRINTING ADDITIVE MANUFACTURING 11

ABSTRACT 11

1. INTRODUCTION 12

2. EXPERIMENTAL 15

2.1. SELECTIVE LASER MELTING (SLM) 15

2.2. LASER FOIL PRINTING (LFP) 16

2.3. CHARACTERIZATION 19

3. RESULTS AND DISCUSSION 21

4. CONCLUSIONS 29

ACKNOWLEDGEMENTS 30

REFERENCES 30

II. ALUMINUM PARTS FABRICATED BY LASER-FOIL-PRINTING ADDITIVE MANUFACTURING: PROCESSING, MICROSTRUCTURE, AND MECHANICAL PROPERTIES 34

ABSTRACT 34

1. INTRODUCTION 35

2. PROCESS OVERVIEW AND EXPERIMENTAL SETUP 37

2.1. LASER FOIL PRINTING (LFP) 37

2.2. CHARACTERIZATION 40

3. RESULTS AND DISCUSSION 42

4. CONCLUSIONS 50

ACKNOWLEDGEMENTS 52

REFERENCES 52

III. THE EFFECT OF LASER WELDING MODES ON MECHANICAL PROPERTIES AND MICROSTRUCTURE OF 304L STAINLESS STEEL PARTS FABRICATED BY LASER-FOIL-PRINTING ADDITIVE MANUFACTURING 56

ABSTRACT 56

1. INTRODUCTION 57

2. PROCESS OVERVIEW AND EXPERIMENTAL SETUP 60

2.1. LASER FOIL PRINTING (LFP) 60

2.2. CHARACTERIZATION 64

3. RESULTS AND DISCUSSION 65

3.1. SINGLE-TRACK LASER WELDING 65

3.2. MICROSTRUCTURE CHARACTERIZATION 66

3.3. MECHANICAL PROPERTIES 69

3.4. CRYSTALLOGRAPHIC TEXTURE CHARACTERIZATION 70

4. CONCLUSION 75

ACKNOWLEDGEMENTS 76

REFERENCES 76

IV. DEVELOPMENT AND EXPERIMENTAL STUDY OF AN AUTOMATED LASER-FOIL-PRINTING ADDITIVE MANUFACTURING SYSTEM 81

ABSTRACT 81

1. INTRODUCTION 81

2. PROCESS OVERVIEW, CONSTRUCTED SYSTEM AND EXPERIMENTAL MEASUREMENTS 84

2.1. OVERVIEW OF LASER FOIL PRINTING (LFP) PROCESS AND SYSTEM 84

2.2. AUTOMATED LASER FOIL PRINTING PROCESS STEPS 85

2.3. EXPERIMENTAL MEASUREMENTS 86

3. RESULTS AND DISCUSSION 88

3.1. MECHANICAL POLISHING 88

3.2. TEST PARTS' GEOMETRIES AND DIMENSIONS 89

3.3. MECHANICAL PROPERTIES 90

4. CONCLUSION 95

ACKNOWLEDGEMENTS 96

REFERENCES 96

SECTION

2. CONCLUSIONS AND FUTURE WORK 99

2.1. CONCLUSIONS 99

2.2. FUTURE WORK 101

BIBLIOGRAPHY 103

VITA 107

LIST OF ILLUSTRATIONS

SECTION Page

Figure 1.1 As-fabricated three-dimensional Zr-based Metallic Glass parts by LFP 2

Figure 1.2 As-fabricated samples by LFP: (a) a model of Gateway Arch in St. Louis; (b) a logo of Missouri University of Science and Technology; (c) a cylinder with gradient lateral surfaces; and (d) a sensor-embedded cylinder with rotating gradient lateral surfaces..... 3

PAPER I

Figure 1. Schematic illustrations of the two steps in SLM for the processing of each layer: (a) powder feeding; (b) selective powders melting. 16

Figure 2. Schematic illustration of the LFP system. 17

Figure 3. Schematic illustrations of the five steps in LFP for the processing of each layer: (a) foil feeding; (b) spot welding; (c) pattern welding; (d) contour cutting; (e) excess foil removing. 18

Figure 4. (a) Side-view of a part made by LFP and SLM showing how the horizontal and vertical tensile specimens were extracted and (b) dimensions of the tensile specimen. 20

Figure 5. OM images of the cross-sections: (a) SLM-H; (b) SLM-V; (c) LFP-H; and (d) LFP-V. 22

Figure 6. XRD patterns of SLM and LFP parts. 23

Figure 7. Corresponding SEM images and EBSD patterns of the grain distribution for (a, b) SLM-H; (c, d) SLM-V; (e, f) LFP-H; and (g, h) LFP-V. 24

Figure 8. The number of grains vs. grain size of (a) SLM-H; (b) SLM-V; (c) LFP-H; and (d) LFP-V; (e) the cumulative area ratio vs. grain size in the EBSD patterns. 25

Figure 9. Tensile stress-strain curves of the SLM and LFP parts in the horizontal (H) and vertical (V) directions. 26

Figure 10. SEM images showing the fracture surfaces of the tensile specimens: (a,b) SLM-V; (c,d) LFP-H. 28

Figure 11. Heat-dissipation mechanism of (a) LFP and (b) SLM. 29

PAPER II

Figure 1. Schematic illustration of the LFP system. 38

Figure 2. Schematic illustrations of the five steps in LFP for the processing of each layer: (a) foil feeding; (b) spot welding; (c) pattern welding; (d) contour cutting; (e) excess foil removing. 39

Figure 3. (a) Al-1100 alloys fabricated by LFP; (b) side view of a part fabricated by LFP showing how the X-axis direction and Z-axis direction tensile specimens were extracted; (c) dimensions of the tensile specimen. 40

Figure 4. (a) Cross-sectioned OM images in Y-Z plane at different levels of power density (MW/cm^2), volumetric energy input (J/mm^3), and scanning speed (mm/s); (b) width and (c) depth vs. VEI at the different levels of power density: 6.3 MW/cm^2 (Green); 6.6 MW/cm^2 (red); 7.0 MW/cm^2 (blue). 44

Figure 5. Tensile properties of the annealed and LFPed aluminum specimens in the laser scanning (LFP-X) and part building (LFP-Z) directions. 45

Figure 6. OM images of the etched surface of (a) annealed aluminum part; (b) LFP-fabricated part in X-Y plane; (c) LFP-fabricated part in Y-Z plane. Yellow dashed lines in (a) represent the grain boundary; red dashed lines in (b) & (c) represent the boundry of melt pool; the red arrows in (b) & (c) represent the grain growth direction; green arrows represent the laser scanning direction in (b). 47

Figure 7. (a) SEM image of a pore of LFP-fabricated specimen and (b) its EDS mapping of oxygen content. 48

Figure 8. SEM images showing the fracture surface of the tensile aluminum specimens: (a) annealed; (b) LFP-X. 48

Figure 9. EBSD patterns of (a) X-Y plane of LFP-fabricated aluminum part and (b) Y-Z plane; (c) annealed aluminum part. 51

PAPER III

Figure 1. The LFP system constructed and used in the research. 61

Figure 2. Schematic illustrations of the six steps in the LFP process for the fabrication of each layer: (a) foil feeding; (b) spot welding; (c) pattern welding; (d) contour cutting; (e) excess foil removing; and (f) surface flattening. 62

Figure 3. (a) side view of a 304L SS part fabricated by LFP showing how tensile specimens were extracted along the laser scanning direction (X) and layer building direction (Z); (b) dimensions of the tensile specimen. 63

Figure 4. Single-track surface morphology (X-Y plane) OM images at a laser power of 400 W and the scan speed of (a) 100 mm/s, (b) 200 mm/s, (c) 300 mm/s, and (d) 400 mm/s; the corresponding cross-section morphology (Y-Z plane) SEM images are shown in (e)-(h). 68

Figure 5. Polished cross-section OM images of (a) conduction mode and (b) keyhole mode; etched cross-section OM images of (c) conduction mode and (d) keyhole mode; etched cross-sectional SEM images in the Y-Z plane of (e) conduction mode and (f) keyhole mode. 68

Figure 6. Dendritic microstructure of (a) conduction-mode welded AM part and (b) keyhole-mode welded AM part in the Y-Z plane; cellular microstructure of (c) conduction-mode part and (d) keyhole-mode part in the X-Y plane. 72

Figure 7. Tensile properties of the LFP-fabricated parts using keyhole-mode and conduction-mode welding in the laser scanning direction (X) and in the part building direction (Z). 73

Figure 8. Band contrast and EBSD patterns of (a) & (b): conduction mode in the X-Y plane; (c) & (d): conduction mode in the Y-Z plane; (e) & (f): keyhole mode in the X-Y plane; (g) & (h): keyhole mode in the Y-Z plane. 74

Figure 9. EBSD patterns of a single melt pool using (a) the keyhole-mode and (b) conduction-mode laser welding. 75

PAPER IV

Figure 1. The automated Laser Foil Printing (LFP) system. 85

Figure 2. Key LFP process steps: (a) foil feeding, (b) spot welding, (c) pattern welding, (d) contour cutting, (e)excess foil removal, and (f) surface polishing. 87

Figure 3. The dimensions of the tensile bar. The measurement unit is mm. 88

Figure 4. Surface profiles of a built layer at two different locations: (a, c) after contour cutting, and (b, d) after mechanical polishing. 92

Figure 5. A rectangular plate with an internal channel. 93

Figure 6. A rectangular plate with notches and rounded corners. 93

Figure 7. Stress-strain curves of eight LFP fabricated tensile specimens 94

Figure 8. Ultimate tensile strength vs. ductility of 304 SS parts fabricated by LFP, L-PBF and DED processes. 95

LIST OF TABLES

SECTION Page

Table 1.1. Literature on L-PBF of 304L stainless steel. 5

PAPER I

Table 1. Characteristics of lasers used in this study. 19

Table 2. Tensile and micro-hardness test results of the SLM and LFP parts. 27

PAPER III

Table 1. Properties of 304L SS and laser beam 63

Table 2. ANOVA analysis of tensile properties 73

PAPER IV

Table 1. Measurements for the rectangular plate with an internal channel. 93

Table 2. Measurements for the rectangular plate with notches and rounded corners. 94

Table 3. Tensile properties of LFP test specimens. 94

1. INTRODUCTION

1.1. BACKGROUND AND MOTIVATION

Additive manufacturing (AM) has been widely used in industry [1], particularly for fabricating three-dimensional (3D) parts with complex-shaped geometries that are otherwise too difficult to make by conventional machining processes [2]. According to the ASTM F42 Committee [3], AM processes can be generally divided into seven categories: vat photopolymerization, material jetting, binder jetting, material extrusion, powder-bed fusion, sheet lamination, and directed energy deposition. The flexibility of the AM process has allowed many different materials (e.g., Ti-6Al-4V, 304L, 316L, IN718, and aluminum alloys) to be fabricated [4]. Currently, most AM metal parts are fabricated by the laser powder bed fusion (L-PBF) processes, also known as the selective laser melting (SLM) process.

This dissertation work utilizes a newly developed laser additive manufacturing process, called Laser Foil Printing (LFP), to fabricate metal parts layer by layer using metal foil as the feedstock. LFP is a laminated object manufacturing process developed at the Missouri University of Science and Technology. The LFP process has been used to build three-dimensional parts of Zirconium-based amorphous metals [5] and crystalline metal of AISI1010 carbon steel [6] with different geometries as shown in Figures. 1.1 and 1.2. It uses a dual-laser system to weld each layer of metal foil onto the substrate or a previously fabricated layer and then cut the cross-sectional contour for the fabrication of each layer. In this process, the thickness of foil can be tens of micrometers to hundreds of micrometers. The cooling rate of melt pool using the foil as the feedstock is high enough

to generate fine crystalline grain structures or even amorphous structures if desired [7-10] because the heat energy of the melt pool can be conducted away very efficiently through the foil. Furthermore, the formation of shrinkage pores can be minimized because the usage of foil does not involve high volumetric reduction during the melting and solidification process. However, as a new laser additive manufacturing technology, little research has been conducted on various metal materials. Extensive studies need to be conducted to comprehensively understand the LFP processability with different metallic materials.

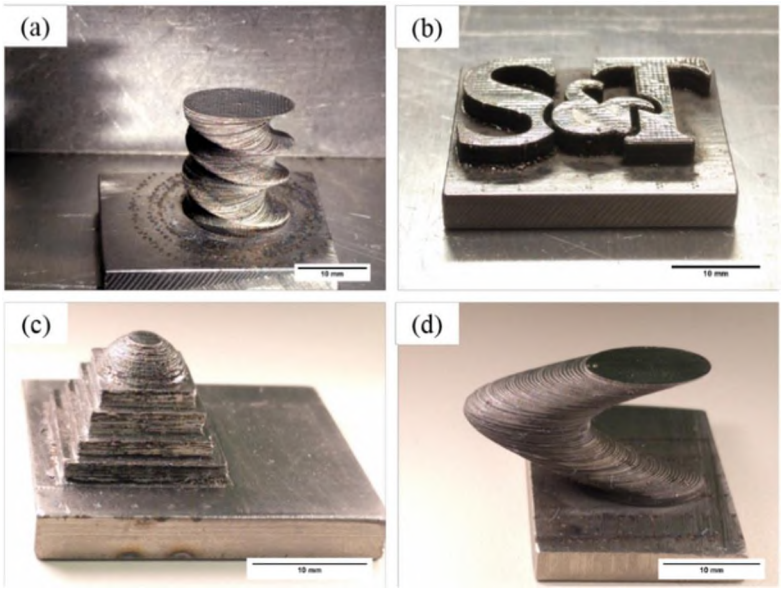

Figure 1.1. As-fabricated three-dimensional Zr-based Metallic Glass parts by LFP [5].

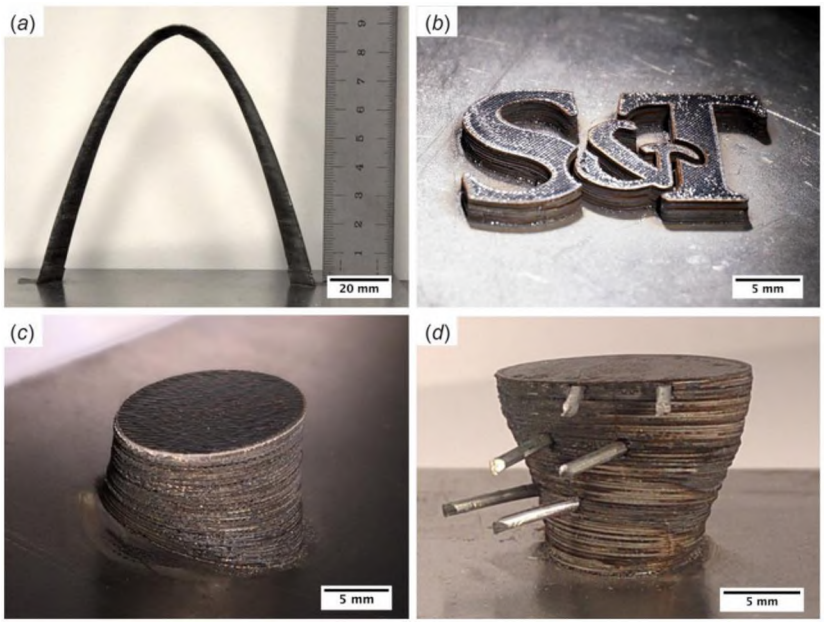

Figure 1.2. As-fabricated samples by LFP: (a) a model of Gateway Arch in St. Louis; (b) a logo of Missouri University of Science and Technology; (c) a cylinder with gradient lateral surfaces; and (d) a sensor-embedded cylinder with rotating gradient lateral surfaces [6].

1.2. METAL ADDITIVE MANUFACTURING

1.2.1. Additive Manufacturing of Stainless Steel. 304L stainless steel (304L SS) has been widely used in industry because of high corrosion resistance and high weldability [11]. In the laser additive manufacturing (LAM) community, extensive studies have been done on the fabrication of 304L SS components and its characterization from powder properties to part properties of LAM-fabricated parts. Those studies investigating the mechanical properties of parts fabricated by the Laser Powder-Bed Fusion (L-PBF) process, also known as the Selective Laser Melting (SLM) process, using 304L SS powder as the feedstock are summarized in Table 1.1 [12-15]. From this table, the highest yield strength (YS), ultimate tensile strength (UTS), ductility of the L-PBF part were 485 MPa, 712 MPa, and 61%, respectively, which can provide a meaningful

reference for mechanical properties comparison between LFP and L-PBF processes. In Table 1.1, the maximum laser power is 220 W. Note that the laser power is normally limited to less than 400 W in order to avoid possible powder blown away by the recoil pressure in case of using a high-power laser. However, depending upon design applications and process parameters, high-power lasers may be employed to increase the processing speed. Moreover, the powder-bed layer thickness in L-PBF is usually limited to 20-100 μm due to concerns on the balling behavior and formation of pores [16,17]. The powder bed used in L-PBF may include a mixture of particles ranging from a few nanometers to tens of micrometers. The powder size distribution can have significant effects on powder melting, powder-bed densification, pore formation, and consequently the quality of manufactured parts. There is no universal powder size distribution that can result in the best possible mechanical properties. Actually, powder size distribution for most commercially available powders is considered to be proprietary by the company that sells the powders. Furthermore, due to the porous nature of the powder bed with gaps between particles, the thermal conductivity of the metal powder bed is significantly lower than that of the bulk material of the same metal [18-20]. The formation of pores is inherently formed in the L-PBF process due to ~40% volumetric reduction during the melting and solidification process. Additionally, the cost of powder is much more expensive and the purchase of powder is limited to a few vendors. The combination of low laser power, small powder-bed thickness, and high powder cost leads to a slow production rate with an expensive cost for the L-PBF process. Moreover, the balling and spattering behavior can occur due to the porous nature of powder bed, which could lead to the formation of voids or pores in the part [16,21,22]. Because powder and foil have

different materials properties, we will use multiple material characterization techniques to conduct rigorous comparisons on parts fabricated by using powder and foil as the feedstock in order to understand their differences.

Table 1.1. Literature on L-PBF of 304L stainless steel.

	Laser power (W)	Scanning speed (mm/s)	Layer Thickness (µm)	Density (%)	YS* (MPa)	UTS** (MPa)	Elongation (%)
Abd-Elghany et al., 2012[12]	95	70-90	30-70	81.25-92.9	142	377	11.2
Nguyen et al., 2019 [13]	200	1400	40	99.99	485	712	61
Ghayoor et al., 2020 [14]	105	50-600	30	99	540	660	36
Hou et al., 2020 [15]	220	1100	40	99.9	450	665	68.5

1.2.2. Additive Manufacturing of Aluminum Alloys. Aluminum alloys have been extensively used in aerospace, automotive, and structural applications that require materials having a high strength-to-weight ratio, good thermal conductivity, and fine corrosion resistance [23,24]. Although using additive manufacturing (AM) to create complex-geometry parts of aluminum alloys is attractive, not much research has been conducted [25,26] on aluminum alloys fabricated by AM processes with the exception of AlSi10Mg [27-31]. The addition of silicon in aluminum alloys is done to reduce oxygen absorption and enhance melt pool fluidity. This reduces the oxidation and increases the wettability between successive layers to reduce porosity. Silicon has also been shown to increase the powder flowability in laser powder bed fusion (L-PBF) processes [27,32]. AM of aluminum alloys with low silicon content has not been extensively studied because of laser processing difficulty. AM of aluminum is exacerbated in L-PBF

processes due to the high percentage of volumetric reduction and the poor fluidity of molten metal associated with aluminum powder during solidification, resulting in the high porosity (~10% porosity) of AM-fabricated aluminum parts [33]. Moreover, the large surface area of powder promotes oxidation, which could be detrimental to the part properties [33,34]. Because the laser processing of aluminum alloys to create fully dense parts has been proven difficult to achieve through traditional AM processes, it is necessary to find an alternative AM technology to be able to overcome this laser processing difficulty caused by the unfavorable physical properties of aluminum alloy (e.g., high optical reflectivity, high oxidation tendency, high thermal expansion, and a low percentage of volatile elements) and fabricate dense AM aluminum parts.

1.2.3. Laser Welding Modes in Additive Manufacturing. Depending on the magnitude of laser power density and laser energy input, the laser welding mechanism can be changed from the conduction mode (absorbing laser energy through object's surface) to the keyhole mode (absorbing laser energy through Fresnel reflections) [35]. The former reflects ~60% of incident laser beam at the wavelength of 1.06 μm [36] while the latter can absorb nearly all the laser beam energy [37]. This high laser energy absorption is due to multiple reflections of the laser incident beam and plasma-enhanced coupling effect [38] within a hole at the center of melt pool, where the hole is opened by the recoil pressure of vapor generated from a high laser power density irradiation [39,40].

For laser additive manufacturing processes, single-track melt pools creating by both laser welding modes have been studied on Ti-6V-4V (Ti64) and 316L [41-43] using L-PBF processes. King's [43] experimentally conducted parametric studies on single-track melt pools using both laser welding modes show consistency with an engineering

model from Verhaeghe's research [40]. The L-PBF fabricated Ti64 part using the conduction-mode laser welding has higher formability (less porosity) while higher porosity was reported in the part using the keyhole-mode laser welding [42]. However, even though the keyhole-mode welding has less formability, it has a better combination of strength and ductility due to the microstructure difference between the Ti64 parts made by the two modes [42,44].

No research has investigated the effect of laser welding mode on mechanical properties of 304L SS AM parts. In this dissertation, we investigate laser welding modes (keyhole mode and conduction mode) on the mechanical properties in the LFP process and find factors that make their part properties different through various material characterizations.

1.3. RESEARCH OBJECTIVES

The overall aims of this dissertation work are to understand the LFP-fabricated part properties and processability of the 304L stainless steel and the Al-1100 aluminum alloy, the effect of laser welding mode on mechanical properties in LFP, and the dimensional accuracies and mechanical properties of 304L SS parts fabricated by an automated LFP system. The specific research objectives are as follows:

1. Identify the differences between 304L stainless steel parts fabricated by the laser foil printing and the laser powder bed fusion processes.
2. Investigate the processability of Al-1100 aluminum alloy in the laser-foil-printing process.

3. Understand the effect of laser welding mode on the properties of 304L SS parts fabricated by LFP.
4. Evaluate the dimensional accuracies and mechanical properties of 304L SS parts fabricated by our automated LFP system and compare them to those of 304L parts fabricated by other laser additive manufacturing processes.

1.4. SCIENTIFIC AND TECHNICAL CONTRIBUTIONS

In this dissertation study, the experimental results show that the laser foil printing (LFP) process is a promising laser additive manufacturing technology. The scientific and technical contributions of this research are listed below.

1. Because of foil's natural characteristics, three-dimensional 304L metal parts fabricated by LFP have higher strength and ductility as well as lower material cost compared with those parts fabricated by the commercial laser additive manufacturing community using powder as the feedstock.
2. Despite the unfavorable physical properties of aluminum alloys for laser processing, the LFP parameter windows for Al-1100 aluminum alloy were found and used to fabricate dense aluminum parts (density > 99.3%) using the LFP process, which is beyond the capability of powder bed fusion processes.
3. The 304L parts fabricated by LFP in the conduction mode were more ductile than those fabricated in the keyhole mode with comparable strength, due to their distinctive grain structures.
4. The automated LFP system has been proven that it can be used to automatically fabricate three-dimensional metal parts with various geometries, with the use of

mechanical polishing to remove the elevated edges induced by the UV laser cutting after the laser patterning of each layer.

1.5. ORGANIZATION OF DISSERTATION

The background has been given in Section 1.1-1.4 to explain the objectives of this dissertation and relevant research regarding laser additive manufacturing technologies. The dissertation then includes four published papers addressing the research objectives.

The first paper presents a comprehensive investigation on 304L stainless steel parts fabricated by the laser foil printing (LFP) and laser powder bed fusion (L-PBF) processes. The mechanical properties, grain microstructure, porosity, surface area, and oxygen content of sample parts fabricated by these two processes were measured and compared. The tensile test results showed that the part fabricated by LFP had higher strength than the part fabricated by L-PBF. The grain structures of LFP and L-PBF parts indicated that the grains in LFP parts were finer than the grains in L-PBF parts, which was due to the thermal conductivity difference between foil and powder. The oxygen content of LFP-fabricated part was 75% less than the L-PBF part because of ~10 times smaller surface area of foil compared to powder.

The second paper focused on the investigation of process parameter windows for Al-1100 aluminum alloy to find out a proper laser energy density to stabilize the melt pool formation and create sufficient penetration depth for the fabrication of dense aluminum parts. Dense aluminum parts (>99.3% relative density) were fabricated by the LFP process. The LFP-fabricated aluminum parts were shown to have better tensile strength compared to annealed Al-100 specimens. Strong orientation preference along the

solidification direction and dense subgrain boundaries in the LFP-fabricated samples were observed.

In the third paper, two laser welding modes (keyhole mode and conduction mode) were used to fabricate 304L metal parts using the LFP process. Based on cross-sectional views of parts, the parts fabricated in the conduction mode had higher densities than those fabricated in the keyhole mode. Although the difference of tensile strength between them was insignificant, the conduction-mode parts had higher ductility than the keyhole-mode parts due to the difference between their distinct grain structures.

The fourth paper investigates the characterization of 304L stainless steel parts fabricated by a fully automated LFP system. The results indicated that the dimensional accuracy of LFP-fabricated parts was very good and the mechanical test results showed that these parts had relatively high and repeatable strength and ductility compared to parts fabricated by other laser additive manufacturing processes.

PAPER

I. ENHANCED MECHANICAL PROPERTIES FOR 304L STAINLESS STEEL PARTS FABRICATED BY LASER-FOIL-PRINTING ADDITIVE MANUFACTURING

Chia-Hung Hung, Austin Sutton, Yingqi Li, Yiyu Shen, Hai-Lung Tsai, and Ming C. Leu

Department of Mechanical and Aerospace Engineering, Missouri University of Science and Technology, Rolla, MO, USA, 65409

ABSTRACT

In this study we demonstrate that the mechanical properties of 304L stainless steel (304L SS) parts fabricated by the laser-foil-printing (LFP) additive manufacturing process can be enhanced as compared to parts fabricated by the selective laser melting (SLM) technology. The tensile test results indicate that the LFP fabricated parts achieve ~15% and ~10% higher in yield strength and ultimate tensile strength, respectively, compared to the SLM fabricated parts. This is mainly because the use of foil feedstock in LFP leads to a higher cooling rate during the solidification of molten metal than the use of powder bed in SLM, due to higher thermal conductivity in foils than powders. By using electron backscattered diffraction it is confirmed that the LFP parts have finer grain structures than the SLM parts, implying a higher cooling rate in LFP. The LFP process also produces metal parts with an average oxygen content about 75% less than those by the SLM process, due to ~10 times of surface area per unit volume in powders than foils.

1. INTRODUCTION

Additive manufacturing (AM) has been widely used in industry [1], particularly for fabricating complex-shaped three-dimensional (3D) parts that are otherwise too difficult to make by conventional machining processes [2]. AM processes can be generally divided into seven categories according to the ASTM F42 Committee [3], including vat photopolymerization, material jetting, binder jetting, material extrusion, powder-bed fusion, sheet lamination, and directed energy deposition. Selective laser melting (SLM) is a powder-bed fusion process, while laser-foil-printing (LFP) can be regarded as a sheet lamination process.

SLM is a popular method for producing metallic parts and has commercially available production facilities, while LFP is a recently developed technology that has not been much explored [4]. SLM uses a laser beam to selectively melt metal particles in a powder bed [5], while LFP employs a laser to weld foils together layer-by-layer. In SLM, each layer of the powder-bed thickness is usually limited to 20-100 μm due to concerns on balling behavior and formation of pores [6]. The powder bed includes a mixture of particles ranging from a few nanometers to tens of micrometers. The powder size distribution can have significant effects on powder melting, powder-bed densification, pore formation, and consequently the quality of manufactured parts. There is no universal powder size distribution that can result in the best possible mechanical properties. Actually, powder size distribution for most commercially available powders is considered to be proprietary by the company that sells the powders. In a commercially available SLM machine, the laser power is normally limited to <400W in order to avoid possible

powder blown away by the recoil pressure in case of a high-power laser. However, depending upon designed applications and process parameters, high-power lasers may be employed to increase the processing speed. After laser welding, there is ~40% layer thickness reduction due to powder melting and densification. For each layer, the maximum thickness after densification is usually less than about 110 μm [7]. Due to the porous nature of the powder bed with gaps between particles, thermal conductivity of the metal powder bed is significantly lower than that of the bulk material of the same metal [8−10]. The combination of low laser power, small powder-bed thickness, and low thermal conductivity of the powder bed leads to a slow production rate of the SLM process. Furthermore, it has been shown that balling and spattering behavior can occur due to the porous nature of the powder bed, which could lead to the formation of voids or pores in the part [6,11,12]. Although the existence of pores in the part could be advantageous in certain biomedical applications, such as prosthetic devices and bone scaffolds [13−16], pores may serve as stress concentrators that will reduce the part's strength, causing unexpected or premature failure of the manufactured components [17].

Laminated object manufacturing (LOM) was one of the first commercialized AM technologies in the early 1990s. The LOM sheets of paper or fully-dense polymer were bonded in a layer-by-layer fashion via glues/adhesive materials. Excess materials were then removed through the use of laser scanning the contour in each layer. LOM can be used to build parts from a variety of materials, but the bonding strength is generally weak and depends on the adhesive materials [18,19].

Laser-foil-printing is a laminated object manufacturing process recently developed at the Missouri University of Science and Technology. In this process, a 3D

metal part is built layer-by-layer using a dual-laser system to weld a layer of metal foil on the substrate or a previous layer and then cutting the cross-sectional contour for each layer. The dual-laser system consists of a continuous-wave laser for welding and a pulsed laser for cutting [20]. To facilitate automation, cutting the foil to the desired shape for each layer may be done in advance by laser or other methods before the foils are welded. The thermal conductivity and the corresponding cooling rate of the foil may be high enough to create three-dimensional amorphous structures if desired [21]. In LFP, each layer of foil thickness ranges from tens of micrometers to a few hundred micrometers. As there is no reduction of layer thickness in LFP, the LFP process can be a faster and more efficient way of producing metallic parts than the SLM process. In addition, the possible formation of porosity can be significantly reduced as compared to powder-bed processes.

In this study, 304L stainless steel (304L SS) was selected as the material since it is widely used in industry and has high corrosion resistance and high weldability [22]. The 304L SS parts were built by a homemade LFP system and by a commercial SLM system in an inert shielding gas environment. The tensile properties, micro-hardness, oxygen content, porosity, and microstructures of 304L SS parts fabricated by SLM and LFP were measured and compared with each other. Electron backscattered diffraction (EBSD) was used to identify the phases present, in addition to grain distribution, for the parts manufactured by each process to observe the differences in their microstructures.

2. EXPERIMENTAL

2.1. SELECTIVE LASER MELTING (SLM)

304L SS powders produced by gas atomization (LPW Technology) were used as the feedstock. The particle size distribution was 10% of 19.2 μm, 50% of 27.5 μm, and 90% of 38.3 μm for the cumulative volume. The parts were fabricated on a commercial SLM system (Renishaw AM250) under an argon shielding atmosphere with an oxygen content < 0.1%. The laser system consists of an infrared pulsed laser, a galvano-mirror scanner, and an F-Theta focal lens. The pulsed laser has a central wavelength of 1070 nm, beam quality M^2 of 1.2, maximum pulse repetition rate of 100 kHz, pulse duration of 75 μs, and maximum average power output of 200 W. The laser beam was focused on the surface of the powder bed and the beam diameter was 68.4 μm.

In the processing of each layer, the powders were first spread on the substrate using a recoater blade, as shown in Figure 1(a). The layer thickness (s_1) was 50 μm. Then, a pulsed laser was applied to melt powders in selected regions with a striped scanning strategy (Figure 1(b)). The laser power (P), pulse time interval (t), point distance (D_p), and hatch space (h) were 200 W, 75 μs, 60 μm, and 80 μm respectively. The laser scan speed (v) calculated was 800 mm/s, by dividing the point distance by the pulse time interval. The volumetric energy input (E) calculate was 50 J/mm^3 based on the following equation [23]:

$$E = \frac{P}{v \cdot h \cdot s_1} = \frac{P \cdot t}{D_p \cdot h \cdot s_1} \quad (1)$$

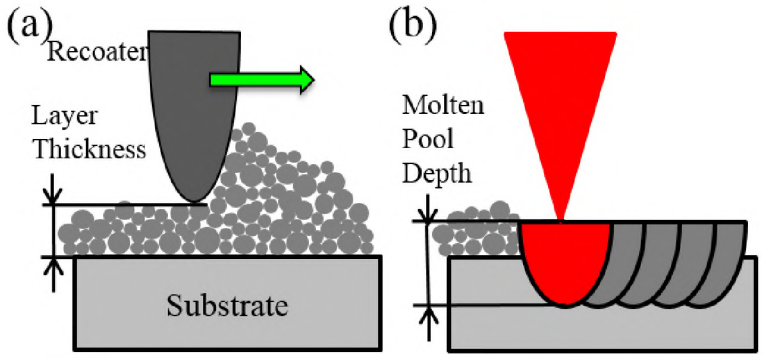

Figure 1. Schematic illustrations of the two steps in SLM for the processing of each layer: (a) powder feeding; (b) selective powders melting.

2.2. LASER FOIL PRINTING (LFP)

304L SS foils were used as the feedstock, and the thickness of each layer was 125 μm. Details of the LFP system can be found in Ref. [19]. In order to facilitate the following discussion and to compare with the SLM system, the LFP system is briefly described below. The laser system consists of a continuous-wave (CW) fiber laser (IPG YLP-1000) for welding and an ultraviolet (UV) pulsed laser for cutting, as schematically shown in Figure 2. The CW fiber laser subsystem includes a beam expander, a galvano-mirror scanner (SCANLAB), and an F-Theta lens. The UV pulsed laser (Coherent AVIA-355X) subsystem includes optical reflection mirrors, a focal lens, and high-precision motor driven stages. The CW fiber laser has a center wavelength of 1070 nm, beam quality factor M^2 of 3.04, and maximum average power output of 1000 W. The focal length of the F-Theta lens is 330 mm, and the spot size is ~160 μm. For the UV laser, its center wavelength, pulse width, maximum pulse repetition rate, and maximum average power output are 355 nm, 30 ns, 100 kHz, and 10 W, respectively. The focus length of the lens is 100 mm and the spot size is 40 μm. Both the CW and UV laser beams are focused on the foil surface.

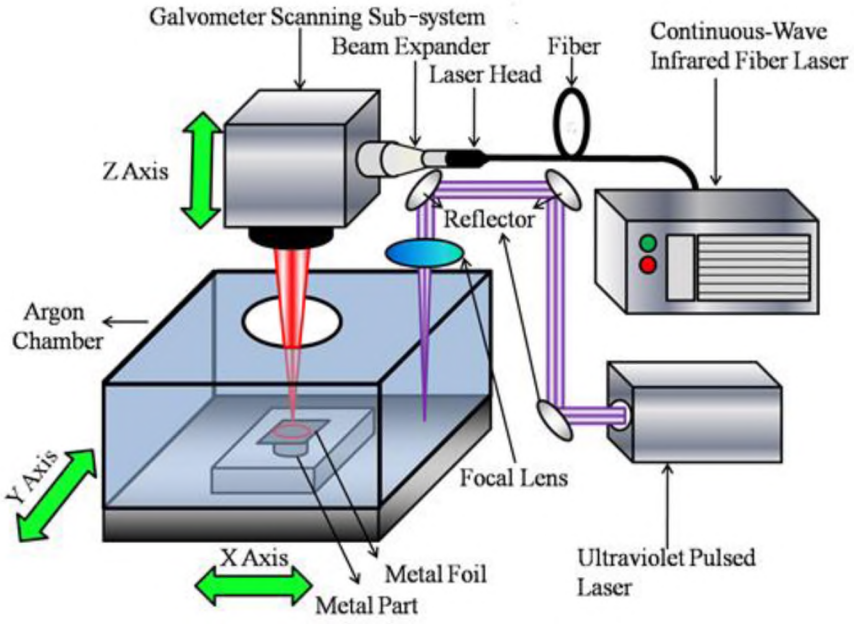

Figure 2. Schematic illustration of the LFP system.

To build a metal part using LFP, five steps are followed for each layer, as illustrated in Figure 3. First, a layer of metal foil is placed on the substrate or the previously welded layer (see Figure 3(a)). Next, spot welding is applied on the metal foil using the CW fiber laser (see Figure 3(b)). The purpose of the spot welding is to fix the foil onto the previous layer to prevent the foil from possible thermal distortion/curving. The third step is pattern welding which uses a raster scan strategy, as shown in Figure 3(c). The foils are welded under an argon shielding atmosphere with an oxygen content of ~1%. The fourth step is to cut the pattern's contour using the UV pulsed laser (see Figure 3(d)). Finally, the excess foil is removed (see Figure 3(e)). Note that the foil can be pre-cut into the desired shape for each layer according to the CAD model of the part and then the foil cross-sections are welded together layer by layer. In this study, for spot welding, the laser power was 400 W, the weld time was 0.5 ms, and the distance between

spots was 1 mm. For pattern welding, the laser power was 400 W, the laser scan speed was 200 mm/s, and the hatch space was 0.1 mm. Thus the laser energy input was 160 J/mm^3 by applying Equation 1. For cutting the pattern's contour, the pulse energy was 0.16 mJ with the pulse frequency of 4 kHz and the cutting speed of 5 mm/s.

Although the processing parameters used in the aforementioned SLM and LFP processes are different, they represent the conditions that can achieve the part density greater than 99% (i.e., <1% porosity) in each process [24]. A summary of characteristics for the three lasers used in this study is given in Table 1. The SLM process uses conduction-mode welding while the LFP process uses keyhole-mode welding [21,25].

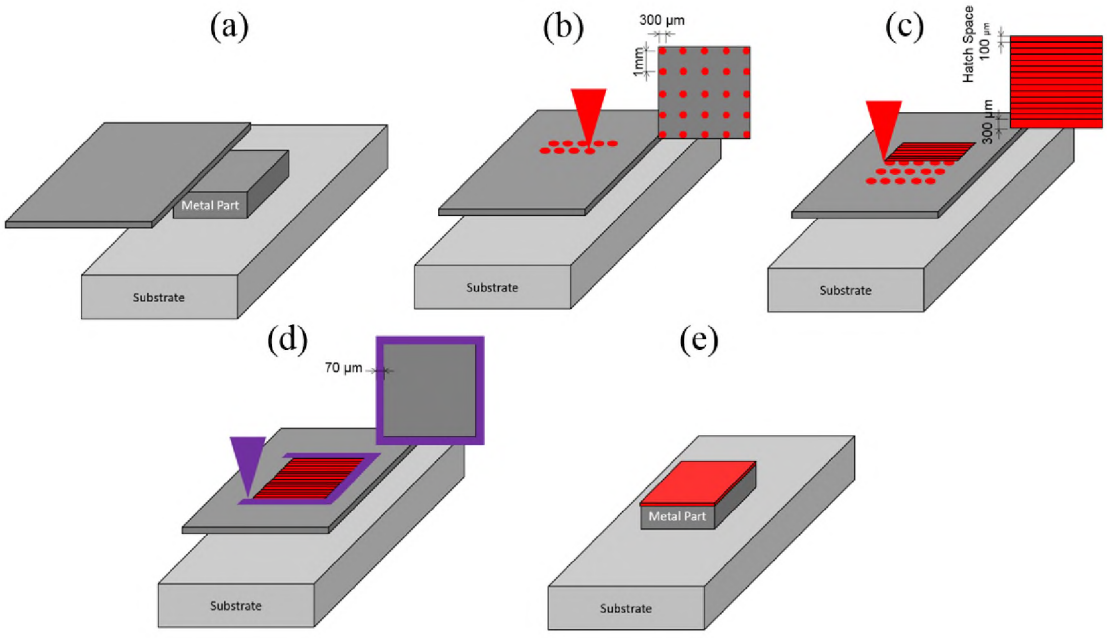

Figure 3. Schematic illustrations of the five steps in LFP for the processing of each layer: (a) foil feeding; (b) spot welding; (c) pattern welding; (d) contour cutting; (e) excess foil removing.

Table 1. Characteristics of lasers used in this study.

Process	SLM	LFP	
Laser Type	SPI SP-200C	IPG YLR-1000	Coherent AVIA-355X
Operational Mode	Modulated Pulse	Continuous-Wave	Solid-State Q-Switched Pulse
Max. Nominal Output Power	200 W	1000 W	10 W
Max. Pulse Repetition Rate	100 kHz	N/A*	100 kHz
Wavelength	1070 nm	1070 nm	355 nm
Pulse Duration	75 µs	N/A*	30 ns
Beam Quality, M^2	1.2	3.04	1.2

*Not Applicable

2.3. CHARACTERIZATION

The parts fabricated by SLM and LFP were cut off from the substrates for purpose of analysis. The oxygen content was measured by carrier gas hot extraction (Leco TC500). The microstructure was characterized by using an optical microscope (OM, Nikon Epiphot 200), an X-ray diffraction instrument (XRD, Philips X'pert MRD), and a scanning electron microscope (SEM, Helios Nanolab 600) equipped with electron backscattered diffraction (EBSD) capability. The specimens for OM, XRD, SEM, and EBSD analyses were polished using standard metallographic techniques with a final polishing step using 0.04 µm silica. The specimens were then electro-etched using 1.5 volts with 70% nitric acid and 30% deionized water. The porosity was determined through calculating the area of pores on OM images of the cross-section with a total area of 7×5 mm2. ImageJ was used to measure the area of pores. The surface area analyzer (NOVAe) was used to measure the surface area of the original powders based on the Brunaue-Emmett-Teller theory. The EBSD patterns had the scanning area of 450×450 µm2 and pixel resolution of 2 µm. The average grain size of EBSD pattern was calculated by following the ASTM E2627-13 standard.

The mechanical properties of the SLM and LFP parts were measured using tensile testing and micro-indentation. For the tensile tests, the tensile strength along the layer

building direction (i.e., the vertical direction, indicated by "V") and the tensile strength along the laser scanning direction (i.e., the horizontal direction, indicated by "H") were both tested, as shown in Figure 4(a), since the horizontal and vertical directions are the two directions in which the part usually has either the highest or lowest strength [26,27]. Tensile test specimens were cut from the fabricated block part using wire electrical discharge machining (EDM) in order to avoid the surface effect on the mechanical properties [28]. The dimensions of the tensile specimen are shown in Figure 4(b), with the thickness of 1 mm. The tensile tests were conducted on an INSTRON machine with a clip-on extensometer at room temperature. The speed of the machine crosshead was maintained at 0.015 mm/mm/min (strain rate per minute). Seven specimens were tested for each direction, and the mean value with one standard deviation was reported. The fracture surfaces after tensile testing were analyzed using SEM (ASPEX-PICA 1020). The micro-hardness was measured using a Vickers micro-hardness tester (Struers, Duramin 5) with 981.2 mN load and 10 s load duration. The reported micro-hardness value was the average of seven measurements with one standard deviation.

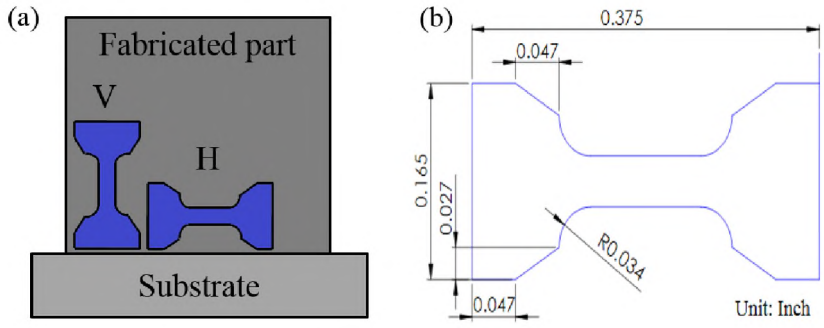

Figure 4. (a) Side-view of a part made by LFP and SLM showing how the horizontal and vertical tensile specimens were extracted and (b) dimensions of the tensile specimen.

3. RESULTS AND DISCUSSION

The oxygen content of each of the powder, the foil, the SLM part and the LFP part was first measured since it could affect the performance of mechanical properties of fabricated part [29]. The oxygen content of the powder is 242 ± 17 ppm. After the SLM processing, the part contains more oxygen content (345 ± 42 ppm). The oxygen content of the foil is 59 ± 1 ppm, which is lower than the powder. After the LFP processing, the oxygen content of the part is increased to 90 ± 35 ppm. Even though the LFP part was built in an argon shielding atmosphere with much higher oxygen content than the atmosphere the SLM part was built in, the LFP part has much lower oxygen content than the SLM part. This is because the surface area per unit volume of the powder (21.9 ± 0.9 μm-1) is much higher (approximately ten times greater) than that of the foil (2.0 μm-1, based on the geometry of the foil), thus the powder has higher tendency to oxidation.

Figure 5 shows the typical optical microscope (OM) images of the horizontal and vertical cross-sections of the SLM part and the LFP part. Pores are observed on both the SLM part and the LFP part. The porosity of the SLM part in the horizontal and vertical direction was measured to be 0.04% and 0.1%, respectively. The LFP part has slightly higher porosity (0.5% in the horizontal direction and 0.28% in the vertical direction) than the SLM part. Although in general a high porosity could deteriorate the mechanical properties [30,31], the parts fabricated by SLM and LFP were both insignificantly affected by porosities due to their values less than 1%.

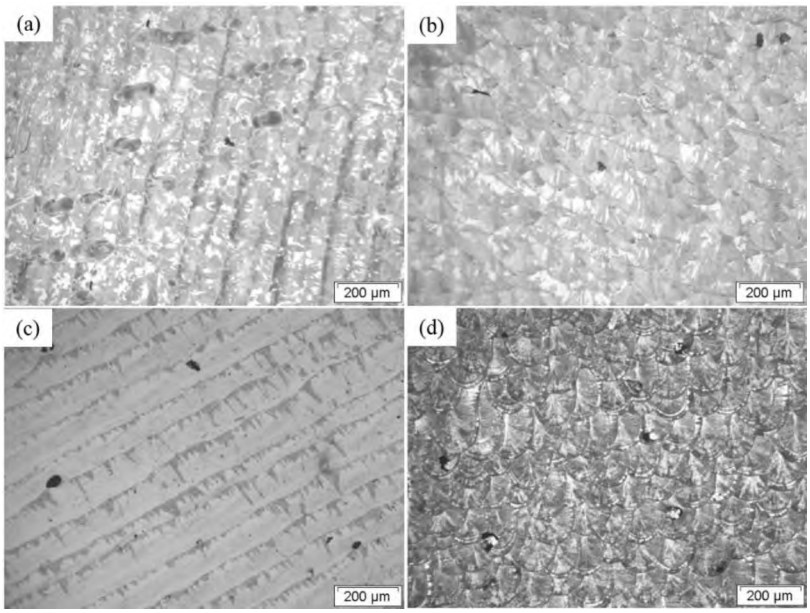

Figure 5. OM images of the cross-sections: (a) SLM-H; (b) SLM-V; (c) LFP-H; and (d) LFP-V.

Figure 6 shows the XRD patterns of the SLM and LFP parts. The SLM part and the LFP part are both composed of austenite phase with face-centered cubic (FCC) crystal structure, although the relative densities of Bragg peaks of the LFP part are different from those of the SLM part.

In addition to the XRD patterns, the EBSD patterns also confirm that both the SLM and LFP parts consist of austenite phase. EBSD was also used to measure the average grain size and grain distribution of the LFP and SLM parts in both horizontal and vertical directions, as shown in Figure 7. The grain boundary is defined by the orientation angle of any grain whose difference is larger than 10° with all of its neighbor grains. The average grain sizes with standard deviations for SLM-H, SLM-V, LFP-H, and LFP-V are 8.9±8, 12±13, 7.9±7, and 9.1±7 µm, respectively, indicating that the LFP part has smaller grains than the SLM part. Based on the SEM images and EBSD patterns in Figure 7, the

edges and the centers of the laser scan tracks can also be identified, and they are marked by yellow arrows and red dashed lines, respectively, to help understand the grain growth behavior during the melt pool solidification. For instance, by comparing the SEM images and EBSD patterns from 7(e) to 7(h), the grains could be seen to have grown from the boundary to the center of the melt pool and the grains at the center are finer than those at the boundaries. The relationships between the grain size and the number of grains in the EBSD patterns are summarized in Figure 8. In Figures 8(a)-(d), the number of grains of the LFP-H whose grain size is smaller than 4 μm is the highest among the four under comparison (SLM-H, SLM-V, LFP-H, and LFP-V). Figure 8(e) presents the cumulative ratio of area of grains versus grain size in the EBSD patterns.

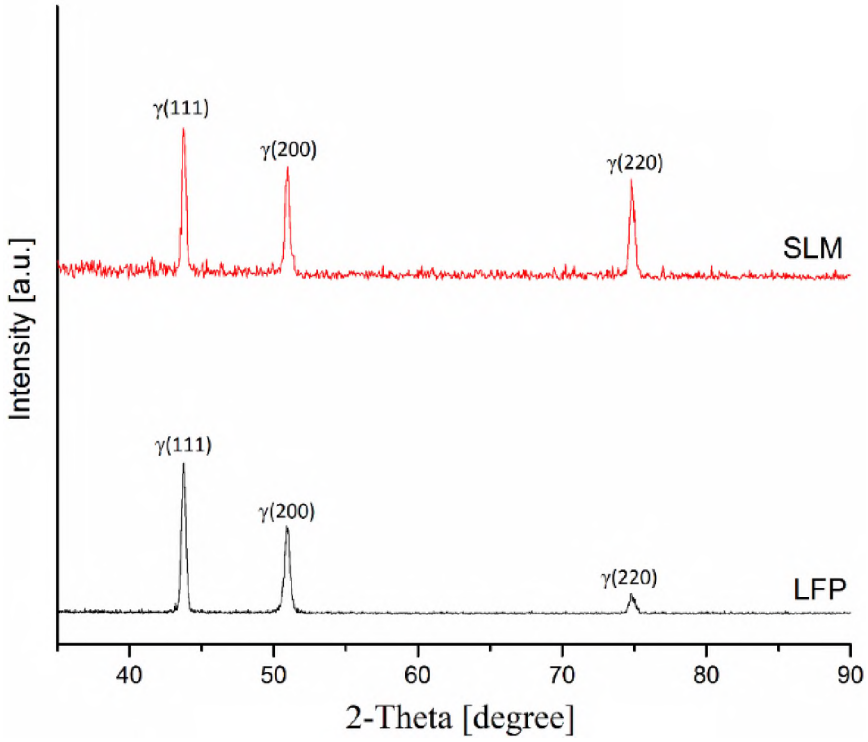

Figure 6. XRD patterns of SLM and LFP parts.

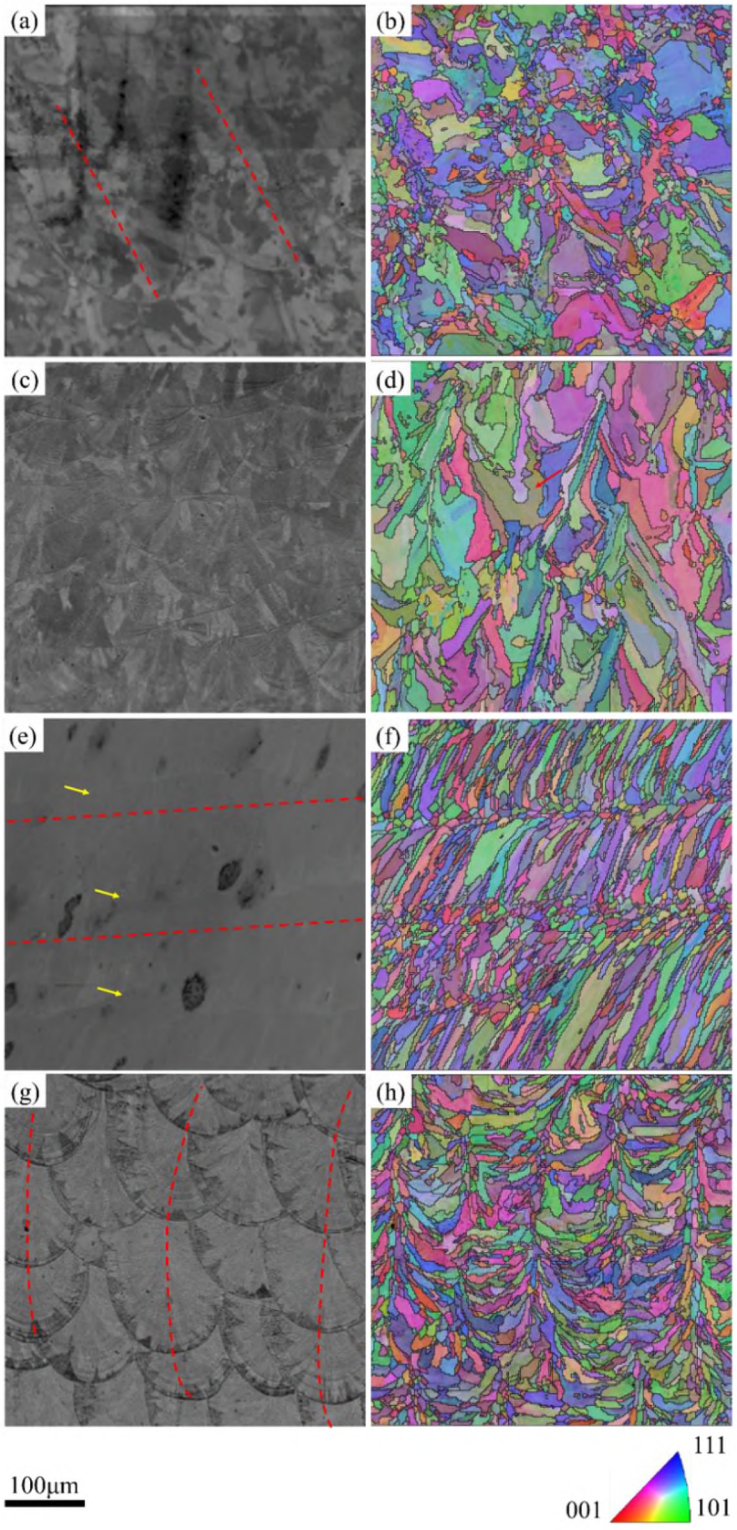

Figure 7. Corresponding SEM images and EBSD patterns of the grain distribution for (a, b) SLM-H; (c, d) SLM-V; (e, f) LFP-H; and (g, h) LFP-V. The red dash lines indicate the center of melt pool having finer grains than the boundaries.

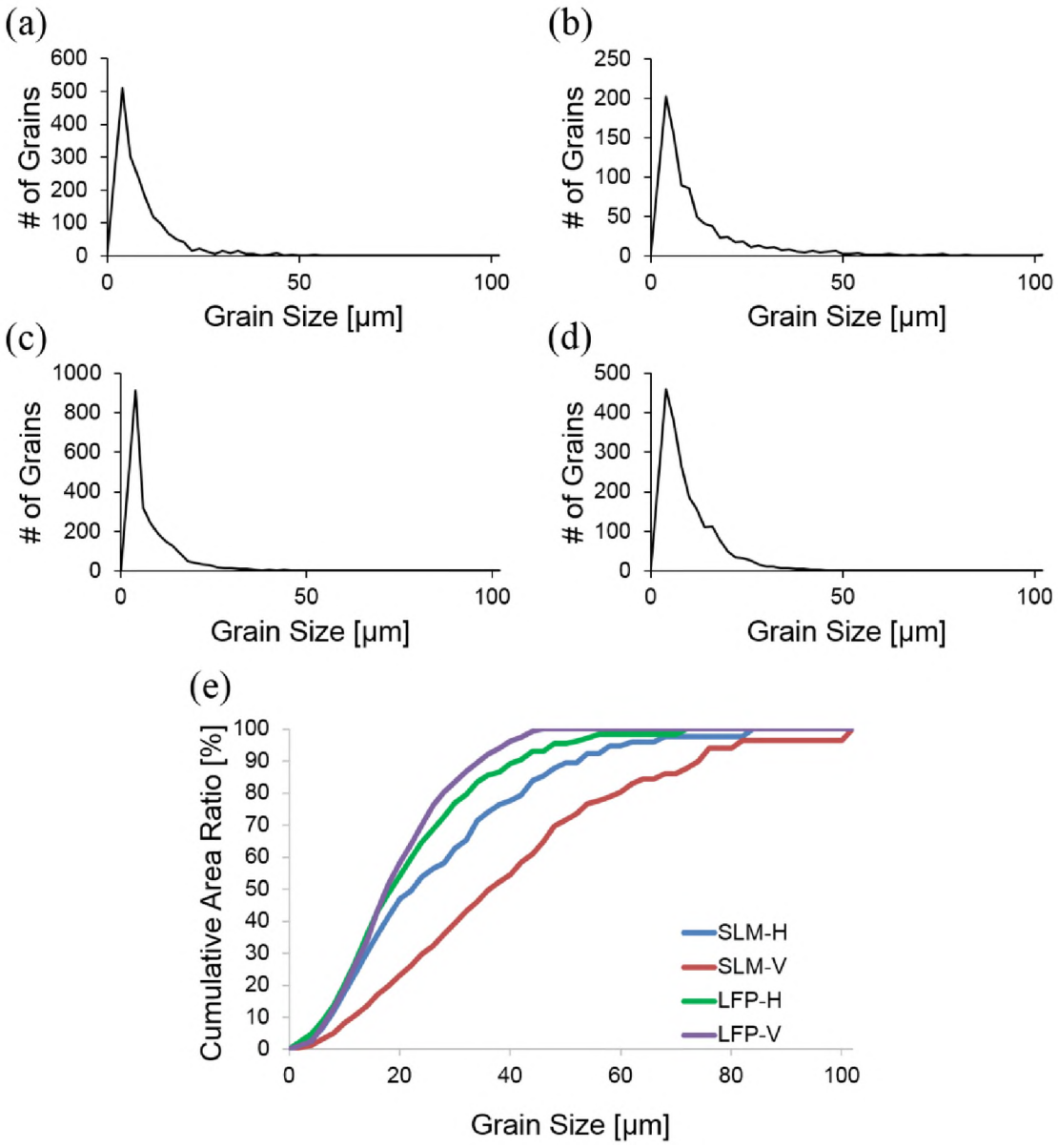

Figure 8. The number of grains vs. grain size of (a) SLM-H; (b) SLM-V; (c) LFP-H; and (d) LFP-V; (e) the cumulative area ratio vs. grain size in the EBSD patterns.

The mechanical properties of the SLM and LFP parts were measured using standard tensile tests. Figure 9 shows representative tensile stress-strain curves for SLM and LFP parts in both vertical and horizontal directions. The average yield strength (YS) and ultimate tensile strength (UTS) with one standard deviation are given in Table 2. The

strength data measured on our SLM parts as shown in this table are comparable to those reported by other researchers [23]. It can be seen that both the SLM part and the LFP part exhibit higher tensile strength along the horizontal direction than the vertical (part building) direction, but lower elongation along the horizontal direction than the vertical direction, which is consistent with the results reported in [27]. The LFP part has higher tensile strength than the SLM part in both the horizontal and vertical directions. In the horizontal direction, the LFP part is ~15% higher in YS and ~10% higher in UTS than the SLM part. In the vertical direction, the LFP part is ~14% higher in YS and ~11% higher in UTS. The micro-hardness of the LFP part is also higher by ~10% than that of the SLM part, as shown in Table 2, which is consistent with the higher tensile strength of the LFP part. However, the LFP part has lower elongation to failure (~13% less in horizontal direction and ~ 20% less in vertical direction) compared to the SLM part.

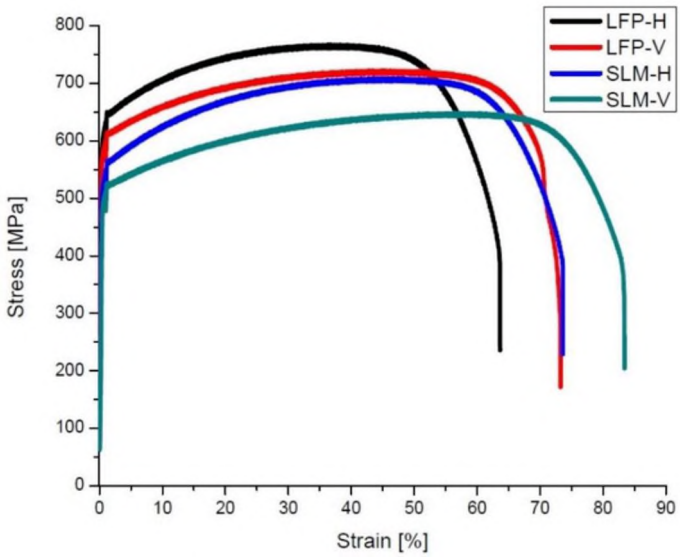

Figure 9. Tensile stress-strain curves of the SLM and LFP parts in the horizontal (H) and vertical (V) directions.

Table 2. Tensile and micro-hardness test results of the SLM and LFP parts.

Process	Orientation	YS (MPa)	UTS (MPa)	Elongation (%)	Hardness (HV)
SLM	H	510 ± 6	699 ± 8	72 ± 3	237 ± 10
SLM	V	488 ± 4	645 ± 4	86 ± 3	229 ± 9
LFP	H	585 ± 3	761 ± 5	64 ±3	260 ± 9
LFP	V	558 ± 13	715 ± 11	72 ± 5	254 ± 7

In tensile tests, the SLM part in the vertical direction exhibits the highest elongation but the lowest strength, while the LFP part in the horizontal direction has the highest strength but the lowest elongation. Thus, the fracture surfaces of the SLM part in the vertical direction and the LFP part in the horizontal direction from the tensile tests were examined and compared using SEM. The results are shown in Figure 10. All fracture surfaces exhibit ductile fracture. The fracture surface of the SLM part in vertical direction contains dimples of ~25 μm in diameter and dense micro-voids, as shown in Figures 10(a) and 10(b), respectively, while the LFP-H part shows a void of ~100 μm and relatively sparse micro-voids, as shown in Figures 10(c) and 10(d), respectively. Micro-voids are indicative of plastic deformation experienced by a ductile material in a typical fracture, and a high density of micro-voids usually indicates good ductility.

The higher strength and lower ductility of the LFP part is mainly contributed by the smaller grain size of the LFP part compared to the SLM part. Di Schino [32] reported that when the grains of 304L become finer, the strength and hardness increase, which is accompanied by a reduction of ductility. This is because smaller grains will increase resistance for motion of dislocations due to more grain boundaries, which impede plastic deformation during the tensile test [33]. In addition, because the average grain size in the vertical direction in both SLM and LFP processes is larger than that in the horizontal

direction, the strength in the horizontal direction is higher than that in the vertical direction. Figure 8 shows that the LFP-H part has the largest amount of fine grains (less than 4 μm), thus it has the highest YS and UTS.

The smaller grain size of the LFP part is attributed to the higher cooling rate of the LFP process than the SLM process. Since powders inevitably have spaces between them, the thermal conductivity of the powder (0.18 W.m−1k−1) is much lower than that of the bulk material (14.92 W.m−1k−1) [7-9]. This prevents the heat from conduction on both sides of the melt pool; see Figure 11. Metal foil has much higher thermal conductivity than metal powder. Even though the laser energy input in the LFP process is greater than that in the SLM process, the higher thermal conductivity of foil results in faster heat removal, thus higher cooling rate [34,35] and smaller grain size.

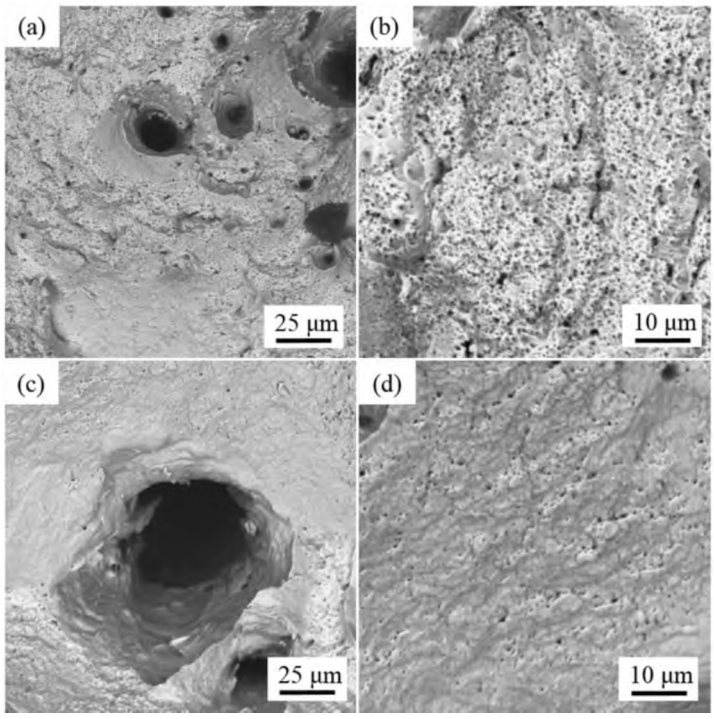

Figure 10. SEM images showing the fracture surfaces of the tensile specimens: (a,b) SLM-V; (c,d) LFP-H.

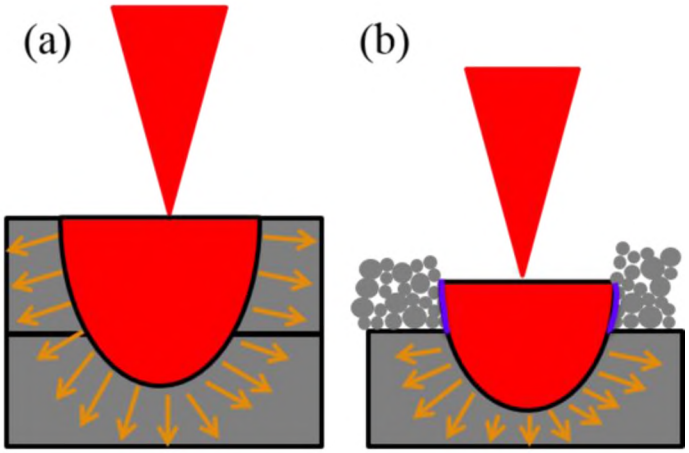

Figure 11. Heat-dissipation mechanism of (a) LFP and (b) SLM.

4. CONCLUSIONS

The mechanical properties of 304L stainless steel parts produced by the LFP process using foils are measured and compared to the parts produced by the SLM process using powders. The comparison shows that the LFP part has higher tensile strength but lower ductility than the SLM part. The higher strength of the LFP part is attributed to the finer grains, which are due to faster heat dissipation leading to higher cooling rates in the LFP process. In both LFP and SLM parts, the part strength in the horizontal (laser scanning) direction is higher than in the vertical (part building) direction. The larger surface area in powder vs. foil leads to higher oxygen content in the SLM part vs. the LFP part.

ACKNOWLEDGEMENTS

This work was supported by the Department of Energy [grant number DE-FE0012272] as well as by the Keith and Pat Bailey Professorship fund from the Missouri University of Science and Technology.

REFERENCES

[1] Frazier WE, Polakovics D, Koegel W. Qualifying of metallic materials and structures for aerospace applications. JOM 2001;53:16–8. doi:10.1007/s11837-001-0171-z.

[2] Thijs L, Verhaeghe F, Craeghs T, Humbeeck J Van, Kruth JP. A study of the microstructural evolution during selective laser melting of Ti-6Al-4V. Acta Mater. 2010;58:3303–12. doi:10.1016/j.actamat.2010.02.004.

[3] ASTM F2792, Standard Terminology for Additive Manufacturing Technologies, ASTM, 2014. doi:10.1520/F2792-10.

[4] Yap CY, Chua CK, Dong ZL, Liu ZH, Zhang DQ, Loh LE, Sing SL. Review of selective laser melting: materials and applications. Appl. Phys. Reviews 2015;2:041101-21. doi:10.1063/1.4935926.

[5] Kruth J, Mercelis P, Van Vaerenbergh J, Froyen L, Rombouts M. Binding mechanisms in selective laser sintering and selective laser melting. Rapid Prototyp. J. 2005;11:26–36. doi:10.1108/13552540510573365.

[6] Li R, Liu J, Shi Y, Wang L, Jiang W. Balling behavior of stainless steel and nickel powder during selective laser melting process. Int. J. Adv. Mfg. Tech. 2012;59:1025–35. doi:10.1007/s00170-011-3566-1.

[7] Spierings AB, Levy G. Comparison of density of stainless steel 316L parts produced with selective laser melting using different powder grades. Proc. SFF Sym. 2009:324-53.

[8] Graves RS, Kollie TG, McElroy DL, Gilchrist KE. The thermal conductivity of AISI 304L stainless steel. Int. J. Thermophys. 1991;12:409–15. doi:10.1007/BF00500761.

[9] Rombouts M, Froyen L, Gusarov A V., Bentefour EH, Glorieux C. Photopyroelectric measurement of thermal conductivity of metallic powders. J. Appl. Phys. 2005;97:1–9. doi:10.1063/1.1832740.

[10] Pujula M, Sánchez-Rodríguez D, Lopez-Olmedo JP, Farjas J, Roura P. Measuring thermal conductivity of powders with differential scanning calorimetry. J. Therm. Anal. Calorim. 2016;125:571–7. doi:10.1007/s10973-016-5274-4.

[11] Liu Y, Yang Y, Mai S, Wang D, Song C. Investigation into spatter behavior during selective laser melting of AISI 316L stainless steel powder. Mater. Des. 2015;87:797–806. doi:10.1016/j.matdes.2015.08.086.

[12] Wang L, Pratt P, Felicelli SD, El Kadiri H, Berry JT, Wang PT, Horstemeyer MF. Pore Formation in Laser-Assisted Powder Deposition Process. J. Mfg. Sci. Eng. 2009;131:51008. doi:10.1115/1.3184087.

[13] Chen SY, Huang JC, Pan CT, Lin CH, Yang TL, Huang YS, Ou CH, Chen LY, Lin DY, Lin HK, Li TH, Jang JSC, Yang CC. Microstructure and mechanical properties of open-cell porous Ti-6Al-4V fabricated by selective laser melting. J. Alloys Compd. 2017;713:248–54. doi:10.1016/j.jallcom.2017.04.190.

[14] Dadbakhsh S, Speirs M, Kruth JP, Van Humbeeck J. Influence of SLM on shape memory and compression behaviour of NiTi scaffolds. CIRP Annals - Mfg. Tech. 2015;64:209–12. doi:10.1016/j.cirp.2015.04.039.

[15] Murphy C, Kolan K, Li W, Semon J, Day D, Leu M. 3D bioprinting of stem cells and polymer/bioactive glass composite scaffolds for tissue engineering. Int. J. Bioprint. 2017;3:53–63. doi:10.18063/IJB.2017.01.005.

[16] Li X, Li W, Rezaei F, Rownaghi A. Catalytic cracking of n-hexane for producing light olefins on 3D printed monoliths of MFI and FAU zeolites. Chem. Eng. J. 2018;333:545–53. doi:10.1016/j.cej.201710.001.

[17] Mower TM, Long MJ. Mechanical behavior of additive manufactured, powder-bed laser-fused materials. Mater. Sci. Eng. A 2016;651:198–213. doi:10.1016/j.msea.2015.10.068.

[18] Gibson I, Rosen D, Stucker B. Additive Manufacturing Technologies. 2015:207-214. doi:10.1007/978-1-4939-2113-3.

[19] Prechtl M, Otto A, Geiger M. Laminated object manufacturing of metal foil-process chain and system technology. AMST'05 Adv. Mfg. Systems and Technology. CISM Int. Centre for Mech. Sci. 2005;486. doi:10.1007/3-211-38053-1_58

[20] Chen C, Shen Y, Tsai HL. A Foil-Based Additive Manufacturing Technology for Metal Parts. J. Mfg. Sci. Eng. 2016;139:24501. doi:10.1115/1.4034139.

[21] Li Y, Shen Y, Chen C, Leu MC, Tsai HL. Building metallic glass structures on crystalline metal substrates by laser-foil-printing additive manufacturing. J. Mater. Process Tech. 2017;248:249–61. doi:10.1016/j.jmatprotec.2017.05.032.

[22] Kwok CT, Lo KH, Chan WK, Cheng FT, Man HC. Effect of laser surface melting on intergranular corrosion behaviour of aged austenitic and duplex stainless steels. Corros Sci. 2011;53:1581–91. doi:10.1016/j.corsci.2011.01.048.

[23] Fayazfar H, Salarian M, Rogalsky A, Sarker D, Russo P, Paserin V, Toyserkani E. A critical review of powder-based additive manufacturing of ferrous alloys: Process parameters, microstructure and mechanical properties. Mater. Des. 2018;144:98-128. doi:10.1016/j.matdes.2018.02.018.

[24] Brown B. Characterization of 304L Stainless Steel By Means of Minimum Input Energy on the Selective Laser Melting Platform. Mechanical and Aerospace Engineering 2015;Master Theses.

[25] Zhou J, Tsai HL, Wang PC. Transport Phenomena and Keyhole Dynamics during Pulsed Laser Welding. J. Heat Transf. 2006;128:680-90. doi:10.1115/1.2194043.

[26] Griffith M, Ensz M, Puskar J, Robino C, Brooks J, Philliber J, Smugeresky J, Hofmeister W. Understanding the microstructure and properties of components fabricated by laser engineered net shaping (LENS). MRS Proceedings 2000;625. doi:10.1557/PROC-625-9.

[27] Guan K, Wang Z, Gao M, Li X, Zeng X. Effects of processing parameters on tensile properties of selective laser melted 304 stainless steel. Mater. Des. 2013;50:581–6. doi:10.1016/j.matdes.2013.03.056.

[28] Wang Z, Palmer TA, Beese AM. Effect of processing parameters on microstructure and tensile properties of austenitic stainless steel 304L made by directed energy deposition additive manufacturing. Acta Mater. 2016;110:226-35. doi:10.1016/j.actamat.2016.03.019.

[29] Conner RD, Maire RE, Johnson WL. Effect of oxygen concentration upon the ductility of amorphous $Zr_{57}Nb_5Al_{10}Cu_{15.4}Ni_{12.6}$. Mater. Sci. Eng. A 2006;419:148-52. doi:10.1016/j.msea.2005.12.009.

[30] Essa K, Jamshidi P, Zou, J, Attallah MM, Hassanin H. Porosity control in 316L stainless steel using cold and hot isostatic pressing. Mater. Des. 2018;138:21-9. Doi:10.1016/j.matdes.2017.10.025.

[31] Baldenebro-Lopez FJ, Gomez-Esparza CD, Corral-Higuera R, Arredondo-Rea SP, Pellegrini-Cervantes MJ, Ledezma-Sillas JE, Martinez-Sanchez R, Herrera-Ramirez JM. Influence of size on the microstructure and mechanical properties of an AISI 304L stainless steel-a Comparison between bulk and fibers. Mater. 2015;8:451–61. doi:10.3390/ma8020451.

[32] Di Schino A, Kenny JM. Grain refinement strengthening of a micro-crystalline high nitrogen austenitic stainless steel. Mater. Lett. 2003;57:1830–4. doi:10.1016/S0167-577X(02)01076-5.

[33] Callister W, Rethwisch D. Materials science and engineering: an introduction. vol. 94. 2007:188-90. doi:10.1016/0025-5416(87)90343-0.

[34] Gil FJ, Ginebra MP, Manero JM, Planell JA. Formation of α-Widmanstätten structure: Effects of grain size and cooling rate on the Widmanstätten morphologies and on the mechanical properties in Ti6Al4V alloy. J. Alloys Compd. 2001;329:142–52. doi:10.1016/S0925-8388(01)01571-7.

[35] Shen Y, Li Y, Chen C, Tsai HL. 3D printing of large, complex metallic glass structures. Mater. Des. 2017;117:213–22. doi:10.1016/j.matdes.2016.12.087.

II. ALUMINUM PARTS FABRICATED BY LASER-FOIL-PRINTING ADDITIVE MANUFACTURING: PROCESSING, MICROSTRUCTURE, AND MECHANICAL PROPERTIES

Chia-Hung Hung[a], Yingqi Li[a], Austin Sutton[a], Wei-Ting Chen[b], Xiangtao Gong[a], Heng Pan[a], Hai-Lung Tsai[a], Ming C. Leu[a]

[a]Department of Mechanical and Aerospace Engineering, Missouri University of Science and Technology, Rolla, MO, USA, 65409

[b]Materials Research Center, Missouri University of Science and Technology, Rolla, MO, USA 65409

ABSTRACT

Additive manufactured aluminum (Al-1100) parts (>99.3% of relative density) were fabricated by our newly developed laser-foil-printing (LFP) processing method. Fabrication of dense aluminum parts was achieved by using a laser energy density of 7.0 MW/cm2 to stabilize the melt pool formation and create sufficient penetration depth with 300 μm thickness foil. The highest yield strength (YS) and ultimate tensile strength (UTS) in the LFP-fabricated samples reached 111 ± 8 MPa and 128 ± 3 MPa, respectively, along the laser scanning direction. These samples exhibited greater tensile strength but less ductility compared to annealed Al-1100 samples. Fractographic analysis showed elongated gas pores in the tensile test samples. Strong crystallographic texturing along the solidification direction and dense subgrain boundaries in the LFP-fabricated samples were observed by using the electron backscattered diffraction (EBSD) technique.

1. INTRODUCTION

The additive manufacturing (AM) process is commonly used to create complex-shaped three-dimensional objects that are difficult to fabricate by traditional machining processes [1]. The flexibility of the AM process has allowed many different materials (e.g., Ti-6Al-4V, 304L, 316L, IN718, and aluminum alloys) to be fabricated [2]. Aluminum alloys have been widely used in aerospace, automotive, and structural applications that require materials having a high strength-to-weight ratio, thermal conductivity, and corrosion resistance [3,4]. Although using the AM technology to create complex-geometry parts of aluminum alloys is attractive, not much research has been conducted [5,6] on aluminum alloys fabricated by AM processes with the exception of AlSi10Mg [7-11]. The addition of silicon in aluminum alloys is done to reduce oxygen absorption and enhance melt pool fluidity. This reduces the oxidation and increases the wettability between successive layers. Silicon has also been shown to increase the powder flowability in powder-bed fusion based AM processes [7,12]. AM of aluminum alloys with low silicon content has not been extensively studied because of processing difficulty. AM of aluminum is exacerbated in powder-bed fusion processes due to the high percentage of volumetric reduction and the poor fluidity of molten metal associated with aluminum powder during solidification, leading to the high porosity (~10% porosity) of the AM-fabricated part [13]. Moreover, the surface area of the powder promotes more oxidation, which could be detrimental to the part properties [13,14]. Therefore, processing aluminum powder to create fully dense parts has been proven difficult to achieve.

The study reported in the present paper uses a different approach known as the laser-foil-printing (LFP) process, which utilizes foil as the feedstock to alleviate the problems associated with powder processing described above. Laser-foil-printing is a laminated object manufacturing process developed at the Missouri University of Science and Technology. It has been used to build 3D-structural parts of Zirconium-based amorphous metals [15] and crystalline metals such as carbon steel and stainless steel [16,17] layer by layer. LFP uses a dual-laser system to weld each layer of metal foil onto the substrate or a previously fabricated layer and then cut the cross-sectional contour for the fabrication of each layer. In this LFP process, the thickness of foil can be tens of micrometers to hundreds of micrometers. The cooling rate of melt pool using the metal foil as the feedstock is high enough to generate fine crystalline grain structures or even amorphous structures if desired [15,17] because the thermal heat of the melt pool can be conducted away efficiently through the foil, instead of powder whose thermal conductivity of powder is significantly lower than the foil [18]. Furthermore, the formation of shrinkage pores can be minimized because the usage of foil does not involve high volumetric reduction during the melting and solidification process.

In this study, Al-1100 is selected as the material in the LFP process since it has the highest thermal conductivity, highest optical reflectivity, highest oxidation tendency, high thermal expansion, and low percentage of volatile elements among the aluminum alloys that are considered not suitable for the powder-bed fusion processes, which is very challenging because of the increase in oxidation layer formation and the difficulty of stabilizing the melt pool formation [13,14]. While the Al-1100 powder has unfavorable physical properties, using foil as the feedstock is ideal for Al-1100 because it circumvents

those aforementioned issues by minimizing the surface exposure, oxidation, and pore formation. The process window of Al-1100 is investigated and optimized through cross-sectioning of samples on a single-layer laser welding with various process parameters. Utilizing the optimized parameters, Al-1100 parts are fabricated by the LFP process. The fabricated samples are investigated by quantifying their mechanical properties through tensile tests and visualization of microstructure using metallography and electron back-scattered diffraction, in comparison to the annealed aluminum samples.

2. PROCESS OVERVIEW AND EXPERIMENTAL SETUP

2.1. LASER FOIL PRINTING (LFP)

Al-1100 (commercial grade pure aluminum, >99% aluminum) foil is used as the feedstock in this study. The thickness of the foil was 150 μm, which is readily available commercially. The LFP system consists of a continuous-wave (CW) fiber laser (IPG YLP-1000) for welding and an ultraviolet (UV) pulsed laser for cutting, as schematically shown in Figure 1. The CW fiber laser subsystem includes a galvo-mirror scanner (SCANLAB) and an F-θ lens. The UV pulsed laser (Coherent AVIA-355X) subsystem includes optical reflection mirrors, a focal lens, and high-precision Aerotech motor-driven stages. The CW fiber laser has a center wavelength of 1070 nm, beam quality factor M2 of 3.04, and maximum average power output of 1000 W. The focal length of the F-θ lens is 330 mm, and the laser spot size (d) is ~160 μm. For the UV laser, its center wavelength, pulse width, and maximum average power output are 355 nm, 30 ns, and 10

W, respectively. The focus length of the lens is 100 mm and the laser spot size is 40 μm. Both the CW and UV laser beams are focused on the foil surface.

To build an aluminum part using the LFP process, five steps are followed for each layer, as illustrated in Figure 2. First, a layer of metal foil is placed onto the substrate or a previously welded layer (see Figure 2(a)). Next, spot welding is applied on the metal foil using the CW fiber laser (see Figure 2(b)). The purpose of spot welding is to fix the foil onto the previous layer to prevent the foil from possible thermal distortion/curving. The third step is pattern welding which uses a meander scan strategy, as shown in Figure 2(c). The foils are welded under an argon shielding atmosphere with an oxygen content of ~1%. The fourth step is to cut the pattern's contour using the UV pulsed laser (see Figure 2(d)). Finally, the excess foil is removed (see Figure 2(e)). Note that the foils can be pre-cut into the shape for each layer according to the CAD file of the part and then the cut foils are welded together layer by layer.

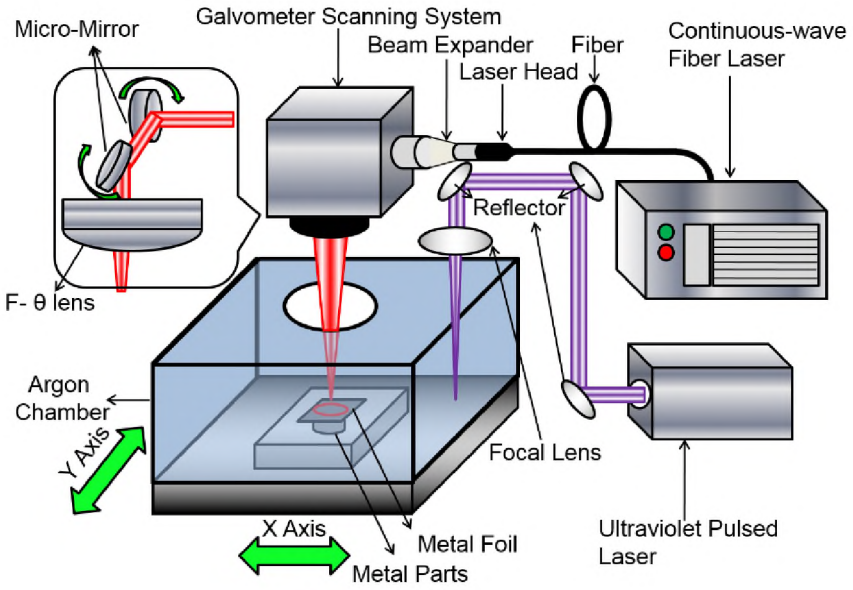

Figure 1. Schematic illustration of the LFP system.

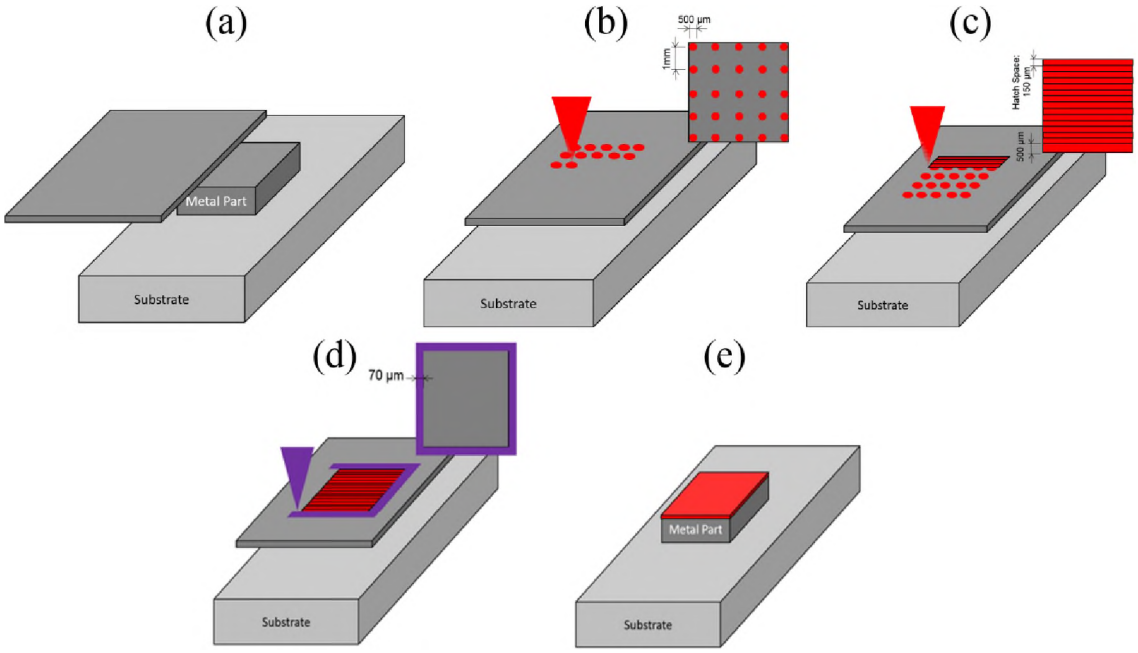

Figure 2. Schematic illustrations of the five steps in LFP for the processing of each layer: (a) foil feeding; (b) spot welding; (c) pattern welding; (d) contour cutting; (e) excess foil removing.

In this study, a 6-mm-thick Al-1100 plate was used as the substrate. To increase the fabrication efficiency, two foils (thickness of 150 µm for each foil) were stacked and welded together at the same time using a single weld, which means a thickness (s1) of 300 µm for every part layer. For spot welding, the laser power was 700 W, the weld time was 7 ms, and the distance between spots was 1 mm. For cutting the pattern's contour, the pulse energy was 0.16 mJ with the pulse repetition rate of 4 kHz and the cutting speed of 1 mm/s. For pattern welding, the process parameters were investigated using various laser powers and speeds with the hatch space (h) of 0.15 mm. The laser power (P) was ranged from 630 to 700 W, the laser scan speed (v) was 100-400 mm/s, and the spot size (d) was 160 µm. The volumetric energy input (VEI) and the power density (Pd) of laser pattern

welding can be calculated using the equations of VEI=P/(v·h·s1) and Pd=8P/(πd2), respectively [19].

The optimal process parameters, with which the melt pools are penetrated to the substrate and stably formed without pores formation, were chosen through a parametric study to build an LFP-fabricated Al-1100 block with the dimensions of 18 mm (length)×12 mm (width)×10 mm (height), as shown in Figure 3. In Figure 3(a), the X-axis is parallel to the laser scanning direction; the Y-axis is perpendicular to the laser scanning direction; the Z-axis is parallel to the layer building direction.

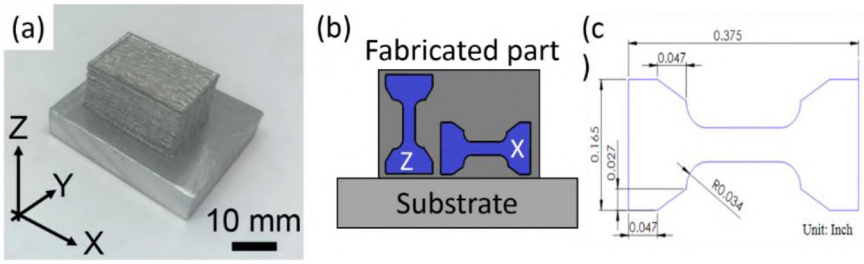

Figure 3. (a) Al-1100 alloys fabricated by LFP; (b) side view of a part fabricated by LFP showing how the X-axis direction and Z-axis direction tensile specimens were extracted; (c) dimensions of the tensile specimen.

2.2. CHARACTERIZATION

The LFP-fabricated aluminum blocks were then cut off from the substrate for analysis. The oxygen determinator (Leco TC500) was used to measure the oxygen content using the carrier-gas hot extraction method. The microstructure and the fracture surface were characterized by using an optical microscope (OM, Nikon Epiphot 200), an X-ray diffraction instrument (XRD, Philips X'pert MRD), and a scanning electron microscope (SEM, Helios Nanolab 600) equipped with electron backscattered diffraction

(EBSD) and energy-dispersive X-ray spectroscopy (EDS) detectors. The specimens for OM and EBSD analyses were polished utilizing standard metallographic techniques using #320 grind paper, 9 μm, 3 μm, or 1 μm diamond suspensions, and 0.04 μm silica. The specimens were etched by immersion in Keller's Reagent (95% deionized water, 2.5% nitric acid, 1.5% hydrochloric acid, and 1% hydrogen fluoride) for revealing the melt pools. The porosity was determined by calculating the area of the pores in OM images of the cross-section with reference to the total area of 63 mm2. The area of pores was measured using ImageJ software [20]. The EBSD patterns had the scanning area of 600×600 μm2 with a step size of 2 μm. The average grain size in each EBSD pattern was calculated by following the ASTM E2627-13 standard [21].

The tensile strengths of the LFP-fabricated Al-1100 specimens were measured along the layer building direction (indicated by "Z") and along the laser scanning direction (indicated by "X"). The tensile specimens as shown in Figure 3(b) were 2 mm thick, and they were cut from the fabricated aluminum blocks using wire electrical discharge machining (EDM) [22]. The tensile tests were conducted on an INSTRON machine with a clip-on extensometer at room temperature at the speed of the machine crosshead of 0.015 mm/mm/min (strain rate per minute). Five LFP-fabricated tensile specimens in both X and Z directions and the annealed aluminum were tested, and the mean value with the standard deviation of each test was reported. The annealed aluminum was fabricated by following the ASTM-B209 standard with annealing heat treatment [23].

3. RESULTS AND DISCUSSION

In order to ascertain the feasible process parameters for building Al-1100 parts using the LFP process, we conducted a parametric study by investigating the effect of depth and width of melt pool with various laser power densities, volumetric energy inputs (VEIs), and laser scanning speeds on Al-1100 alloys. We also examined the specimens' cross-sections, which are shown in Figure 4. The width and depth of melt pools in Figure 4(a) at different levels of VEI, power density, and scanning speed were measured and summarized in Figures 4(b) & 4(c), respectively, along with their standard deviations. Figure 4(a) shows that the power density of 6.3 MW/cm2 is not sufficient to create penetrating and stable melt pools to the substrate even using the slowest scanning speed of 100 mm/s. Based on the large standard deviation of melt pool depth at the laser power density of 6.3 MW/cm2 in Figure 4(c), the melt pool is unstable because the high thermal conductivity of Al-1100 could quickly conduct heat away, causing the situation of lacking laser energy. Therefore, the power density needs to be increased in order to have stable melt pools. As the power increases to 6.6 MW/cm2, the melt pools are stably formed at the VEI of 73 & 147 J/mm3; however, pores are found with higher energy inputs and the top surface becomes rough. As the power density reaches 7.0 MW/cm2, the formation of melt pools is stabilized at the minimum VEI of 52 J/mm3. However, as the VEI increases to 78 J/mm3, micro-pores (marked by yellow circles in Figure 4(a)) are observed at the bottom of the melt pool, which is a typical feature in the keyhole mode of laser welding [24]. In Figure 4(c), the standard deviations of melt pool width and depth at 7.0 MW/cm2 are relatively small in comparison to the other VEIs because the laser

power density is high enough to provide sufficient heat flux for overcoming the high thermal conduction mechanism and stabilizing the formation of melt pools. With the increase in power density, the Marangoni flow of the melt pool could change from the negative surface tension gradient (the molten metal flows from the center toward the edge of the melt pool and causes a small penetration depth) to the positive surface tension gradient (the molten metal flows from the edge toward the center of the melt pool and causes a larger penetration depth) [25]. Therefore, the threshold of power density for producing a stable melt pool is found to be 7.0 MW/cm2. This is the highest threshold of power density reported in the literature among aluminum alloys because Al-1100 does not contain volatile elements (e.g., magnesium, zinc, lithium) that can help stabilizing the formation of melt pools [26-28]. Hereafter, the desirable process parameters of 7.0 MW/cm2, 300 mm/s, and 52 J/mm3 were used to build Al-1100 parts using the LFP process.

The tensile properties of the annealed aluminum and LFP specimens were measured using standard tensile tests. Figure 5 presents the results of tensile testing on the annealed aluminum and the LFP-fabricated specimens in the laser scanning and layer building directions with the yield strength (YS), ultimate tensile strength (UTS), and the elongation at the breaking point with one standard deviation. It can be seen that the strength of the LFP part is higher in both directions than the annealed aluminum. However, the ductility of LFP part is less when compared to the annealed aluminum due to the existence of gas pores shown in Figure 6(b) [29]. In Figure 5, the standard deviation of YS and elongation of the LFP-fabricated parts are larger than the annealed aluminum due to the presence of early failures caused by porosity within the gage section

[29]. Also, Figure 5 reveals higher tensile strength along the laser scanning direction (LFP-X) than the part building direction (LFP-Z), but slightly lower elongation along the laser scanning direction than the layer building direction.

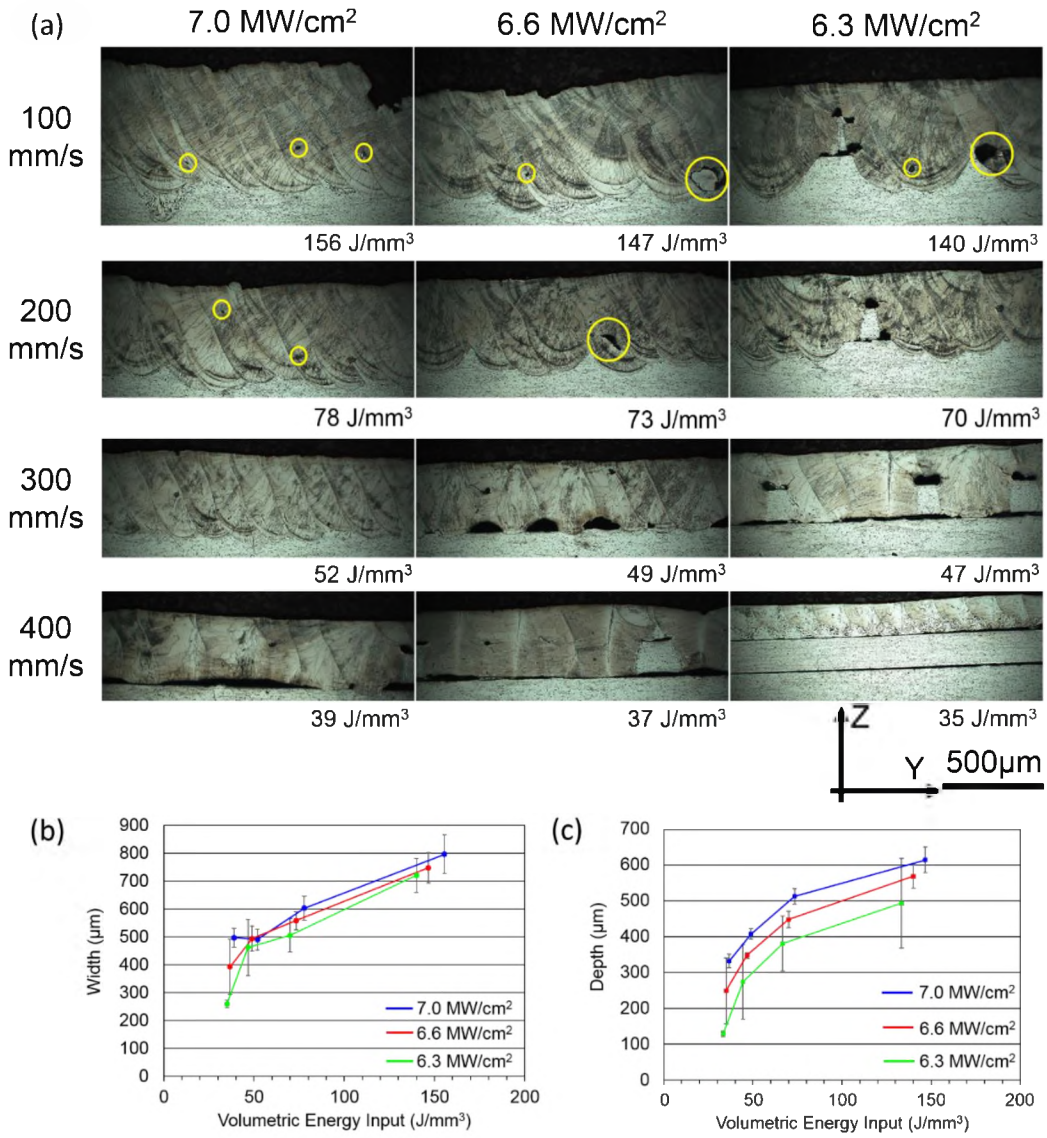

Figure 4. (a) Cross-sectioned OM images in Y-Z plane at different levels of power density (MW/cm^2), volumetric energy input (J/mm^3), and scanning speed (mm/s); (b) width and (c) depth vs. VEI at the different levels of power density: 6.3 MW/cm^2 (Green); 6.6 MW/cm^2 (red); 7.0 MW/cm^2 (blue).

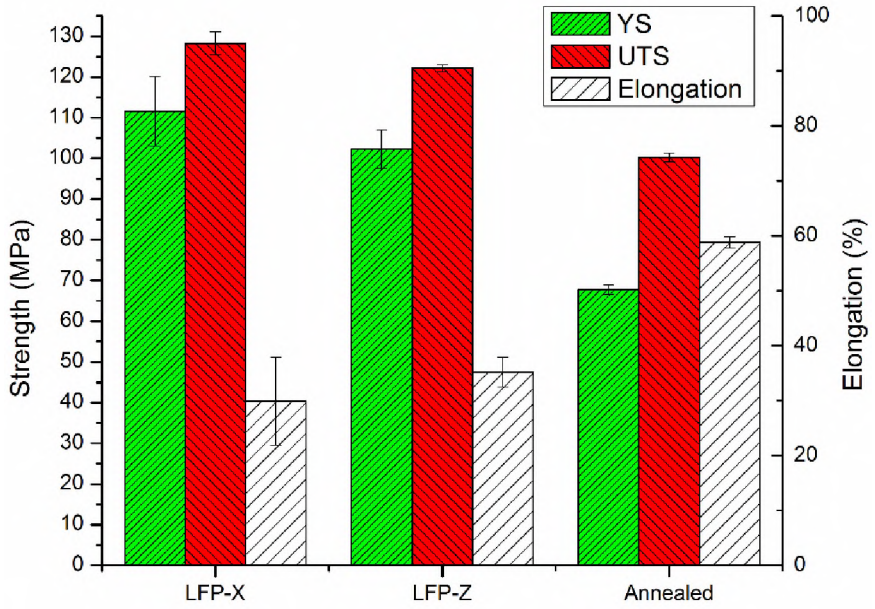

Figure 5. Tensile properties of the annealed and LFPed aluminum specimens in the laser scanning (LFP-X) and part building (LFP-Z) directions.

Since tensile properties are known to be affected by oxygen [30], the oxygen contents were measured. The oxygen contents of the annealed aluminum, foil, and LFP-fabricated part measured were 306 ± 31 ppm, and 73 ± 21 ppm, and 372 ± 59 ppm, respectively. Although the oxygen content of the fabricated part increased ~300 ppm after LFP process, implying oxygen was absorbed by the molten metal during solidification in the build chamber, the oxygen contents between the annealed and LFP-fabricated parts are similar.

The annealed aluminum and LFP-fabricated parts were cross-sectioned and etched for revealing their microstructures and melt pool traces, as shown in Figure 6. The porosities of the annealed aluminum and LFP-fabricated parts are 0.1% and 0.7%, respectively. The geometries of pores within the LFP-fabricated part in Figures 6(b) & 6(c) are dome-shaped and globular. The oxygen content obtained using energy-dispersive

X-ray spectroscopy (EDS) shown in Figure 7(b) is due to the abundant aluminum oxide found at the shell of the pore in Figure 7(a). The geometry and oxidation indicate that the voids are either pores generated from the bubbles of dissolved gas during the solidifying of melt pool at the interface between the solid and solidifying melt pool [31], or due to entrained gas from the gaps between the foil and the substrate [32]. Moreover, the etched surface of an annealed aluminum specimen in Figure 6(a) exhibits typical equiaxed grain boundaries (yellow dashed lines). However, Figures 6(b) and 6(c) pertaining to the X-Y plane and Y-Z plane cross-sections of LFP processed aluminum parts, respectively, contain columnar grains indicative of a high cooling. In Figure 6(b), the growth direction of columnar grains were observed to originate from the edges of melt pool (red dashed lines) toward its center with an angle of ~45 degrees along the laser beam scanning direction (green arrows); the columnar grains in Figure 6(c) grow from the boundary of melt pools (red dashed line) toward its symmetric center line of melt pool as shown in red arrows.

The fracture surface of the annealed aluminum which has the highest ductility of the tensile specimen is compared with the fracture surface of the LFP part which has the lowest ductility of the tensile specimen as shown in Figure 8. The red, green, blue, and purple arrows represent the quasi-cleavage, slip regime, dimple, and elongated gas pore in Figure 8, respectively [33]. Fine and dense dimples are observed in the fracture surface of the annealed aluminum that was the typical fracture feature of the ductile material formed during the microvoid coalescence in Figure 8(a). However, since there are some gas pores formed during the LFP process, the fracture surface of the LFP part contains

quasi-cleavages, slip regimes, sparse dimples, and elongated gas pores, as shown in Figure 8(b) [33,34]. Thus, the parts fabricated by the LFP process have less ductility

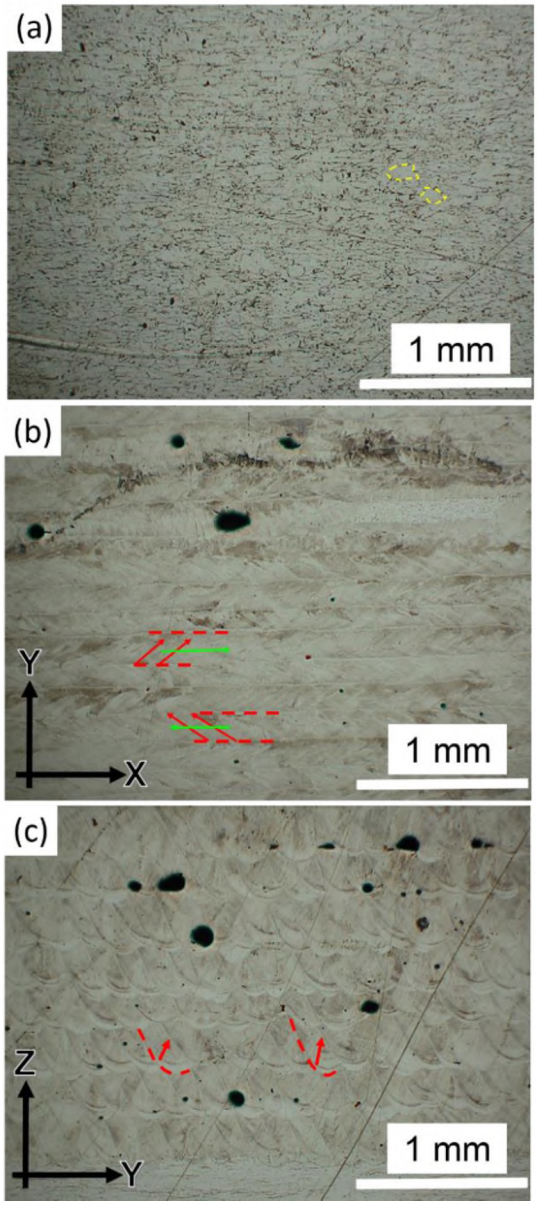

Figure 6. OM images of the etched surface of (a) annealed aluminum part; (b) LFP-fabricated part in X-Y plane; (c) LFP-fabricated part in Y-Z plane. Yellow dashed lines in (a) represent the grain boundary; red dashed lines in (b) & (c) represent the boundry of melt pool; the red arrows in (b) & (c) represent the grain growth direction; green arrows represent the laser scanning direction in (b).

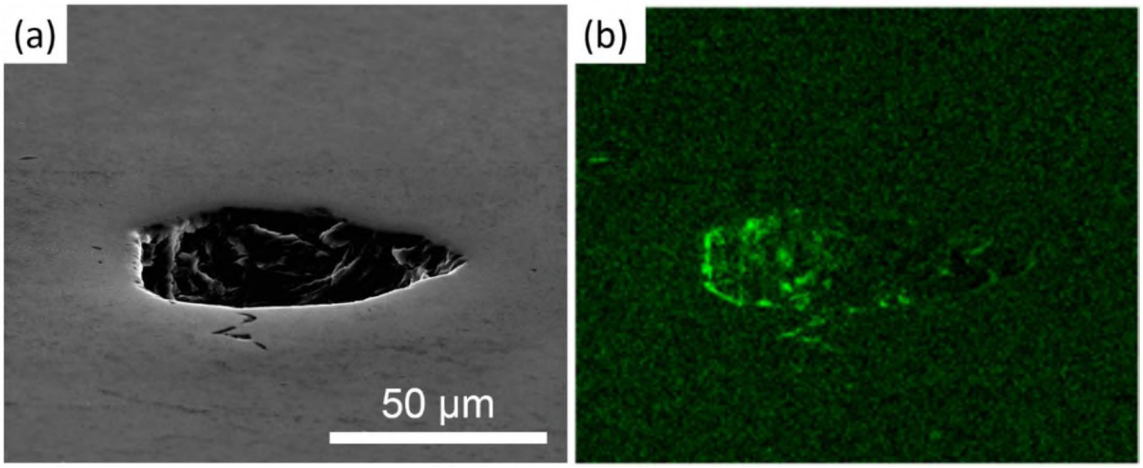

Figure 7. (a) SEM image of a pore of LFP-fabricated specimen and (b) its EDS mapping of oxygen content.

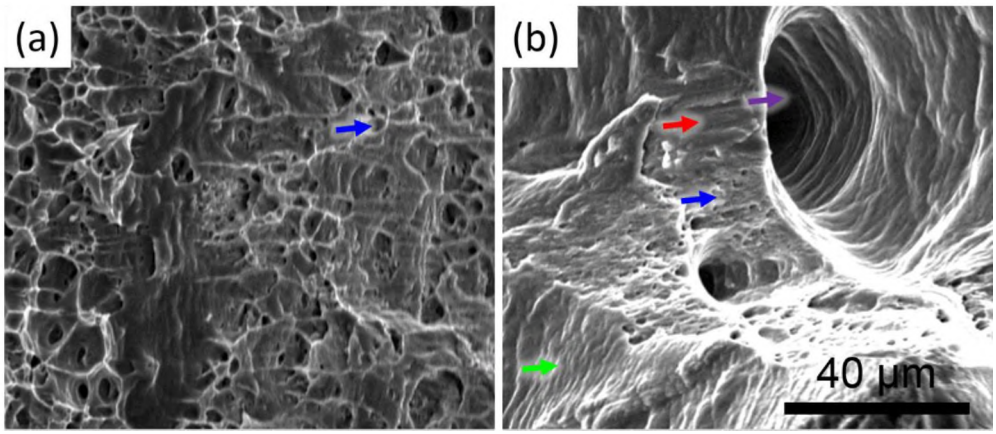

Figure 8. SEM images showing the fracture surface of the tensile aluminum specimens: (a) annealed; (b) LFP-X. The red, green, blue, and purple arrows represent quasi-cleavage, slip regime, dimple, and elongated pore, respectively.

EBSD analysis was performed on the LFP-fabricated and annealed Al-1100 samples to access crystallographic texture and spatial distribution of the Al-1100 grains. The analyses were conducted on the 600 x 600 µm2 polished surfaces on X-Y and Y-Z planes of the LFP-fabricated samples. All EBSD orientation maps and the pole figures acquired from LFP-fabricated samples are presented with respect to the local growth

direction to simplify the discussion. The grain microstructure of the annealed sample was also investigated by using EBSD. Note that only face-centered cubic (f.c.c.) aluminum crystal structure is observed in all EBSD data.

As shown in Figure 9(a), the representative EBSD orientation map reveals the spatial distribution and crystallographic orientations of Al-1100 grains with respect to the local growth direction of the grains on the X-Y plane of the LFP-fabricated sample. The columnar grain structure is observed, with an average grain size of 42.1 ± 10 μm. The growth of columnar grains follows the solidification path toward the heating source. Typically, the grains are grown from the melt pool boundary toward the center of melt pool. Figure 9(a) shows the grain growth direction at a ~45° tilt angle off the laser scanning track because of the temperature gradient of melt pool. This is consistent with the microstructure in Figure 6(b). High density of low-angle grain boundary (LAGB, misorientation angle: 2o-15o) is found in the columnar grains in Figure 9(a), with the subgrain size of 6 ± 3 μm, which is much smaller than the grain size. The variety of subgrain density is related to the local temperature gradient of the melt pool because the cooling rate at the boundary of melt pool is higher than the centerline of melt pool and forms more subgrains at the boundary. The subgrains are observed on the Y-Z plane of LFP-fabricated sample in Figure 9(b) as well. These naturally-formed LAGBs have also been found in the selective laser melting fabricated materials [35]. On the other hand, equiaxed grains are observed in the annealed sample, with an average grain size 20.1 ± 3.5 μm, as shown in Figure 9(c). Little to no LAGBs are found in the annealed sample.

The relationship between grain/subgrain size and mechanical properties were also studied. As reported in the earlier paragraph pertaining to Figure 5, higher YS and UTS

are measured in the LFP-fabricated sample compared with the annealed sample. This attributed to the formation of small subgrains during solidification. The subgrain boundaries inhibit dislocation movement when stress is applied, and hence the mechanical strength of the materials is enhanced. However, pileups of dislocations at grain/subgrain boundaries in the LFP-fabricated sample result in a reduction in ductility, as shown in Figure 5.

Furthermore, the crystallographic texture of the LFP-fabricated sample is presented in the averaged pole figures shown in Figure 9(d). The {001} pole figure intensities are dominated by the regions appearing in red in Figure 9(a), indicating that Al-1100 columnar grains preferentially grow along this orientation. The other intensity clusters in the {001} pole figure, labeled B, C, D, E in Figure 9(d) are associated with symmetrically equivalent poles in the f.c.c. structure, which are inclined by 90o. As expected, the intensity clusters in {111} pole figure are observed 45o-tilt away from {001} poles. The mosaicity in the growth direction is measured to be ~18o from the maxima to minima of the intensity cluster labeled in A, indicating variation of grain orientation.

4. CONCLUSIONS

Additive manufactured parts of Al-1100 aluminum alloy by the laser-foil-printing (LFP) process have been investigated. The process parameter window has been studied through the combination of different levels of power density, scanning speed, and volumetric energy input to find the threshold of power density for stabilizing melt pool

formation during the laser welding process. Al-1100 specimens were built with a density of 99.3% using the LFP process. The yield strength, ultimate tensile strength, and ductility of the Al-1100 specimens fabricated by this additive manufacturing process are measured and compared with the annealed aluminum parts; the yield strength and ultimate tensile strength are 51% and 22% higher, respectively, but the ductility is 54% lower. Electron backscattered diffraction patterns showed low-angle-grain-boundary subgrains formed within high-angle-grain-boundary grains during the fast cooling of the LFP process, with the dominant grain growth orientation of {001}.

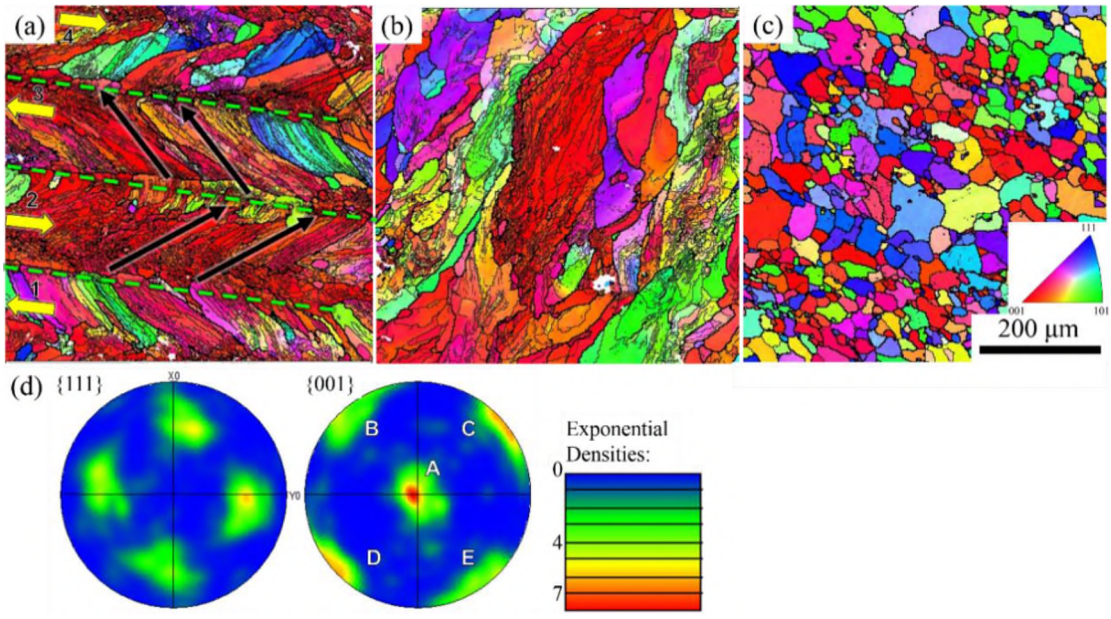

Figure 9. EBSD patterns of (a) X-Y plane of LFP-fabricated aluminum part and (b) Y-Z plane; (c) annealed aluminum part. The scan direction, the grain growth direction, and the melt pool boundaries are marked by yellow arrow, black arrow, and green dashed line, respectively, in (a). Thicker lines and thinner lines in (a)-(c) represent high angle grain boundaries (misorientation angle > 15°, HAGB) and the low angle grain boundaries (misorientation angle between 2° and 15°, LAGB). (d) The poles figures from {001} and {111} reflections were acquired from the area shown in (a).

ACKNOWLEDGEMENTS

This work was supported by the Department of Energy [grant number DE-FE0012272] as well as by the Keith and Pat Bailey Professorship fund from the Missouri University of Science and Technology.

REFERENCES

[1] Thijs L., Verhaeghe F., Craeghs T., Humbeeck J.V., Kruth J.P. A study of the microstructural evolution during selective laser melting of Ti-6Al-4V. Acta Mater. 2010;58:3303-12. doi:10.1016/j.actamat.2010.02.004.

[2] Yap C.Y., Chua C.K., Dong Z.L., Liu Z.H., Zhang D.Q., Loh L.E., Sing S.L. Review of selective laser melting: materials and applications. Appl Phys Rev. 2015;2:0411011. doi:10.1063/1.4935926.

[3] Campbell F.C. Manufacturing technology for aerospace structural materials. 2006. doi:10.1016/B978-1-85617-495-4.X5000-8.

[4] Hirsch J. Recent development in aluminum for automotive applications. T Nonferr Metal S O C. 2014;24:1995-2002. doi:10.1016/S1003-6326(14)63305-7.

[5] Zhang H., Zhu H., Qi T., Hu Z., Zeng X. Selective laser melting of high strength Al-Cu-Mg Alloys: Processing, microstructure and mechanical properties. Mater Sci Eng A. 2016;656:47-54. doi:10.1016/j.msea.2015.12.101.

[6] Gu T., Chen B., Tan C., Feng J. Microstructure evolution and mechanical properties of laser additive manufacturing of high strength Al-Cu-Mg alloy. Opt Laser Technol. 2019;112:140-50. doi:10.1016/j.optlastec.2018.11.008.

[7] Zhang J., Song B., Wei Q., Bourell D., Shi Y. A review of selective laser melting of aluminum alloys: processing microstructure, property and developing trends. J. Mater. Sci. Technol. 2019;35:270-84. doi:10.10116/j.jmst.2018.09.004.

[8] Dinda G.P., Dasgupta A.K., Bhattacharya S., Natu H., Dutta B., Mazumder J. Microstructural Characterization of Laser-Deposited Al 4047 alloy. Metall Mater Trans. A. 2013;44:2233-42. doi:10.1007/s11661-012-1560-3.

[9] Chen B., Moon S.K., Yao X., Bi G., Shen J., Umeda J., Kondoh K. Comparison study on additive manufacturing and powder metallurgy AlSi10Mg alloys. JOM. 2018;70:644-9. doi:10.1007/s11837-018-2793-4.

[10] Kempen K., Thijs L., Humbeeck J.V., Kruth J.P. Processing AlSi10Mg by selective laser melting: parameter optimization and material characterization. Mater Sci Technol. 2015;31:917-23. doi:10.1179/1743284714Y.0000000702.

[11] Thijs L., Kempen K., Kruth J.P., Humbeeck J.V. Fine-structured aluminum products with controllable texture by selective laser melting of pre-alloyed AlSi10Mg powder. Acta Mater. 2013;61:1809-19. doi:10.1016/j.actamat.2012.11.052.

[12] Rana R.S., Purohit R., Das S. Reviews on the influence of alloying elements on the microstructure and mechanical properties of aluminum alloys and aluminum alloy composites. Int J Sci Res. Publ. 2012;2:1-7.

[13] Olakanmi E.O. Selective laser sintering/melting (SLS/SLM) of pure Al, Al-Mg, and Al-Si powders: effect of processing conditions and powder properties. J Mater Process Technol. 2013;213:1387-405. doi:10.1016/j.jmatprotec.2013.03.009.

[14] Jerrard P.G.E., Hao L., Dadbakhsh S., Evans K.E. Consolidation behavior and microstructure characteristics of pure aluminum and alloy powders following selective laser melting processing. Proc of the 36th Int MATADOR Conf. 2010. doi:10.1007/978-1-84996-432-6_108.

[15] Shen Y., Li Y., Chen C., Tsai H.L. 3D printing of large, complex metallic glass structures. Mater Des. 2017;117:213-22. doi:10.1016/j.matdes.2016.12.087.

[16] Chen C., Shen Y., Tsai H.L. A Foil-Based Additive Manufacturing Technology for Metal Parts. J Manuf Sci Eng. 2016;139:024501-1-6. doi:10.1115/1.4034139.

[17] Hung C.H., Sutton A., Li Y., Shen Y., Tsai H.L., Leu M.C. Enhanced mechanical properties for 304L stainless steel parts fabricated by laser-foil-printing additive manufacturing. J Manuf Process. 2019;45:438-46.

[18] Rombouts M., Froyen L., Gusarov A.V., Bentefour E.H., Glorieux C. Photopyroelectric measurement of thermal conductivity of metallic powders. J. Appl. Phys. 2005;97:1–9. doi:10.1063/1.1832740.

[19] Fayazfar H., Salarian M., Rogalsky A., Sarker D., Russo P., Paserin V., Toyserkani E. A critical review of powder-based additive manufacturing of ferrous alloys: Process parameters, microstructure and mechanical properties. Mater Des. 2018;144:98-128. doi:10.1016/j.matdes.2018.02.018.

[20] Dinda G.P., Dasgupta A.K., Bhattacharya S., Natu H., Dutta B., Mazumder J. Microstructural Characterization of Laser-Deposited Al 4047 Alloy. Metall Mater Trans. A. 2013;44A:2233-42. doi:10.1007/s11661-012-1560-3.

[21] ASTM E2627-13, Standard practice for determining average grain size using electron backscatter diffraction (EBSD) in fully recrystallized polycrystalline materials, ASTM International, West Conshohocken, PA, 2013. doi:10.1520/E2627-13.

[22] Wang Z., Palmer T.A., Beese A.M. Effect of processing parameters on microstructure and tensile properties of austenitic stainless steel 304L made by directed energy deposition additive manufacturing. Acta Mater. 2016;110:226-35. doi:10.1016/j.actamat.2016.03.019.

[23] ASTM B209-14, Standard specification for aluminum and aluminum-alloy sheet and plate, West Conshohocken, PA, 2014. doi:10.1520/B0209-14.

[24] Zhou J., Tsai H.L. Porosity formation and prevention in pulsed laser welding. J Heat Transfer. 2007;129:1014-24. doi:10.1115/1.2724846.

[25] Antony K., Arivazhagan N. Studies on energy penetration and Marangoni effect during laser melting process. J Eng Sci Technol. 2015;10:509-25.

[26] Behler K., Berkanns J., Ehrhardt A., Frohn W. Laser beam welding of low weight materials and structures. Mater & Des. 1998;18:261-7. doi:10.1016/S0261-3069(97)00085-X.

[27] Cao X., Wallace W., Poon C., Immarigeon J.P. Research and progress in laser welding of wrought aluminum alloys. I. laser welding processes. Mater Manuf Process. 2003;18:1-22. doi:10.1081/AMP-120017586.

[28] Miyagi M., Wang H., Yoshida R., Kawahito Y., Kawakami H., Shubu T. Effect of alloy element on weld pool dynamics in laser welding of aluminum alloys. Sci Rep. 2018;8:1-10. doi:10.1038/s41598-018-31350-4.

[29] Teng X., Mae H., Bai Y., Wierzbicki T. Pore size and fracture ductility of aluminum low pressure die casting. Eng Fract Mech 2009;76:983-96. doi:10.1016/j.engfracmech.2009.01.001.

[30] Conner R.D., Maire R.E., Johnson W.L. Effect of oxygen concentration upon the ductility of amorphous Zr57Nb5Al10Cu15.4Ni12.6. Mater Sci Eng: A. 2006;419:148-52. doi:10.1016/j.msea.2005.12.009.

[31] Yin H.B., Koster J.N. In-situ observed pore formation during solidification of aluminum. The Iron and Steel Institute of Japan. 2000;40:364-72. doi:10.2355/isijinternational.40.364.

[32] Yousefian P. Pore formation in aluminum castings: theoretical calculations and the extrinsic effect of entrained surface oxide films. Master Theses, ME, UNF. 2017. doi:10.13140/RG.2.2.31160.85769/2.

[33] Fernandino D.O., Boeri R.E. Fracture analysis. ASM Handbook. 2017;1:399-410. doi:10.31399/asm.hb.v01a.a0006323.

[34] Nie F., Dong H., Chen S., Li P., Wang L., Zhao Z., Li X., Zhang H. Microstructure and mechanical properties of pulse MIG welded 6061/A356 aluminum alloy dissimilar butt joints. J Mater Sci Technol. 2016;34:551-60. doi:10.1016/j.jmst.2016.11.004.

[35] Sun Z., Tan X., Tor S.B., Yeong W.Y. Selective laser melting of stainless steel 316L with low porosity and high build rates. Mater Des. 2016;104:197-204. doi:10.1016/j.matdes.2016.05.035.

III. THE EFFECT OF LASER WELDING MODES ON MECHANICAL PROPERTIES AND MICROSTRUCTURE OF 304L STAINLESS STEEL PARTS FABRICATED BY LASER-FOIL-PRINTING ADDITIVE MANUFACTURING

Chia-Hung Hung[a], Wei-Ting Chen[b], M. Hossein Sehhat[a], Ming C. Leu[a]

[a]Department of Mechanical and Aerospace Engineering, Missouri University of Science and Technology, Rolla, MO, USA, 65409

[b]Materials Research Center, Missouri University of Science and Technology, Rolla, MO, USA 65409

ABSTRACT

The success of laser-foil-printing (LFP) additive manufacturing depends critically on the laser welding of sheet metals onto the substrate or the previous layer during the part fabrication process. The welding can be generally categorized into two modes: conduction mode and keyhole mode. In this study, 304L stainless steel parts fabricated by the LFP process using the two laser welding modes are compared. The porosity, microstructure, and tensile properties of the fabricated parts in these two modes are measured and compared in the laser scanning direction (X) and part building direction (Z). The parts fabricated in the conduction mode have a higher density than those fabricated in the keyhole mode. On the tensile properties, both yield strength (YS) and ultimate tensile strength (UTS) have insignificant differences statistically based on the ANOVA analysis between the tensile specimens fabricated with the two welding modes by the LFP process. However, the conduction-mode parts have higher elongation than the keyhole-mode parts in both the X and Z directions, and the difference is especially

significant in the Z-direction. By using the electron backscattered diffraction (EBSD), it was found that the much higher ductility for the conduction-mode parts in the Z-axis direction is mainly due to the distinct grain boundary interface density in the Z-axis direction between the two welding modes.

1. INTRODUCTION

The laser welding process has been widely used to fabricate metallic components for applications in aerospace, automotive and other industries [1,2]. Besides joining of parts, laser welding could also be used in additive manufacturing processes [3,4]. The laser welding process uses a high power laser to heat up and melt two contiguous or lapped metallic pieces, creating a sound bonding between similar [5,6] or dissimilar [7,8] materials. Depending on laser power density and scanning speed, the laser welding mechanism may change from conduction-mode welding (where laser energy is absorbed through the object's surface) to keyhole-mode welding (where laser energy is absorbed through Fresnel absorption and reflection) [8]. The former reflects ~60% of incident laser beam energy at the wavelength of 1.06 μm [9], while the latter can absorb nearly all the laser beam energy [10]. The high laser energy absorption in keyhole-mode welding is due to the multiple reflections of the laser incident beam and the plasma-enhanced coupling effect [11] within a hole at the center of the melt pool, in which the hole is opened by the recoil-pressure of the metal vapor generated by the high laser power density irradiation [12,13].

The formation of melt pools for both welding modes has been simulated and predicted using a numerical model [14,15,16]. The threshold that changes laser welding from conduction-mode welding to keyhole-mode welding can be expressed by the following equation [17]:

$$u_t = \frac{4D}{\sigma}\left(\frac{\sqrt{\pi}kT_b}{\alpha I\sigma}\right)^{-2} \quad (1)$$

where u_t is the keyhole-threshold laser scan speed; D is the thermal diffusivity; σ is the laser spot size; α is the laser absorption coefficient; I is the laser power density; k is the thermal conductivity; and T_b is the boil temperature. According to Eq. (1), for the 304L stainless steel used in this study, the threshold (u_t) can be changed by varying the laser's scan speed, power density, and spot size.

In theory, conduction-mode laser welding should only include a heat conduction mechanism without involving any liquid flow. However, the molten metal inevitably flows during the laser melting process due to the temperature gradients between the center and boundary of a melt pool induced by Gaussian laser beam distribution [18]. Furthermore, the Marangoni convection flow could change in different welding modes [19]: the conduction-mode molten metal flows from the center of a melt pool to the boundary of the melt pool (negative surface tension) while the keyhole-mode molten metal flows from the boundary of a melt pool to the center of the melt pool (positive surface tension) [20]. The aspect ratio (AR), which is the ratio of depth to width of a melt pool, is typically used to distinguish the laser welding mode [21]. As a result, the melt pool created by conduction-mode laser welding is relatively shallow and wide, while the keyhole-mode welding creates a melt pool that is relatively deep and narrow [22].

For additive manufacturing processes, single-track melt pools created by both laser welding modes have been studied on Ti-6Al-4V (Ti64) and 316L [17,23,24] using the laser powder-bed fusion (LPBF) process. LPBF-fabricated Ti64 parts using the conduction-mode laser welding have higher formability (less porosity) than the keyhole-mode laser welding [24]. However, parts fabricated by the keyhole-mode welding have a better combination of strength and ductility (i.e., comparable strength but higher ductility) [24,25]. No research has been conducted thus far to investigate the effect of laser welding mode on mechanical properties of 304L stainless steel (SS) AM parts. The present paper reports an investigation of the relationship between mechanical properties and microstructures in 304L SS parts produced by the two laser welding modes using the laser-foil-printing (LFP) process. The LFP process is a laminated object manufacturing process using foils as the feedstock to fabricate metal parts layer by layer, where each layer of foil is stacked onto the substrate or a previously fabricated layer. A dual-laser system is then used to weld foils and cut the cross-sectional contour for each fabricated layer. This technique has been demonstrated to fabricate high-quality (low-porosity and high-strength) 3D-structural metallic parts with crystalline or amorphous microstructures (e.g., zirconium-based metallic glass, 304L stainless steel, AISI1010 carbon steel, and Al-1100 aluminum alloy) [26,27,28,29].

In this study, single-track laser welding was conducted first using various laser welding speeds to weld 304L SS foils on a stainless-steel substrate at a laser power of 400 W. Based on the aspect ratio of melt pool from the single-track laser welding experiments, optimal process parameters were selected for both welding modes. Then, 304L metallic parts were fabricated by the LFP process using the two laser welding

modes. Tensile properties, porosity, micro hardness, microstructure, and electron back-scattered diffraction were measured or characterized for the LFP-fabricated 304L parts to understand the differences between the parts fabricated by the keyhole and conduction laser welding modes.

2. PROCESS OVERVIEW AND EXPERIMENTAL SETUP

2.1. LASER FOIL PRINTING (LFP)

In this study, the laser-foil-printing (LFP) process was used to fabricate 3-dimensional parts layer by layer using the 304L SS foil as the feedstock. The foil thickness was 125 μm. The LFP system consisted of two laser systems: a continuous-wave (CW) infrared (IR, center wavelength = 1070 nm) fiber laser (IPG YLP-1000) for welding and an ultraviolet (UV, center wavelength = 355 nm) pulsed laser for cutting, as shown in Figure 1. The CW fiber laser subsystem included a galvo-mirror scanner (SCANLAB hurrySCAN-30), and an F-θ lens. The UV pulsed laser (Coherent AVIA-355X) subsystem included optical reflection mirrors, a focal lens, and high-precision Aerotech motor-driven stages. The CW IR fiber laser had a beam quality factor, M2, of 3.04, and a maximum average power output of 1000 W. The focal length of the F-θ lens was 330 mm, and the spot size (σ) was ~160 μm. For the UV laser, its pulse width and maximum average power output were 30 ns and 10 W, respectively. The focal length of the UV lens was 100 mm and the UV spot size was 40 μm. Both laser beams were aligned and focused on the foil surface.

To fabricate a 304L SS part using the LFP process, each layer fabrication included six steps, as illustrated in Figure 2. First, a layer of metal foil was manually placed on the substrate or a previously welded layer (see Figure 2(a)). Next, spot welding was done on the metal foil using the CW fiber laser (see Figure 2(b)) to fix the foil onto the previous layer in order to prevent the foil from possible thermal distortion/curving. The third step was pattern welding, which enables a meander scan strategy (back-and-forth path with a hatch space of 0.1 mm), as shown in Figure 2(c). The foil is welded under an argon shielding atmosphere with ~1% oxygen (O2). The flow rate of argon gas is 11 liters per minute. The fourth step was to cut the pattern's contour using the UV pulsed laser (see Figure 2(d)). After UV laser cutting, the excess foil could be removed (see Figure 2(e)). The surface was then polished as shown in Figure 2(f) to make a flat surface for next-layer fabrication. Note that the foil can be pre-cut into the required shape and dimensions for each layer according to the CAD file of the part and then the cut foils are welded together layer by layer.

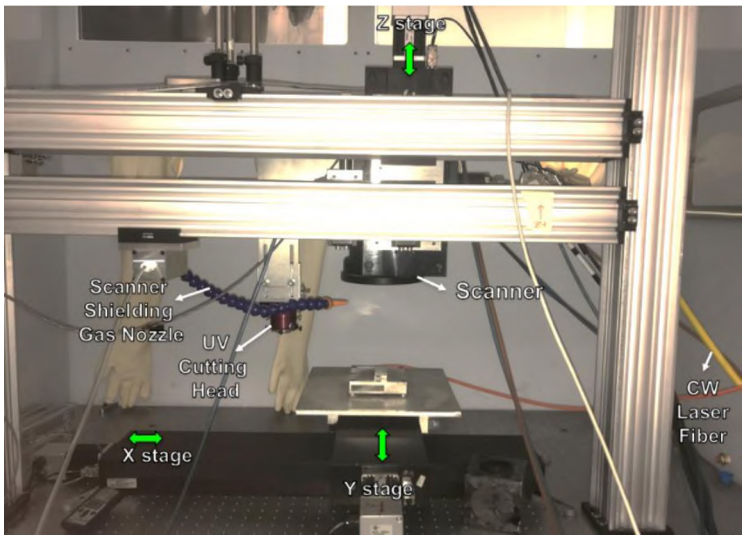

Figure 1. The LFP system constructed and used in the research.

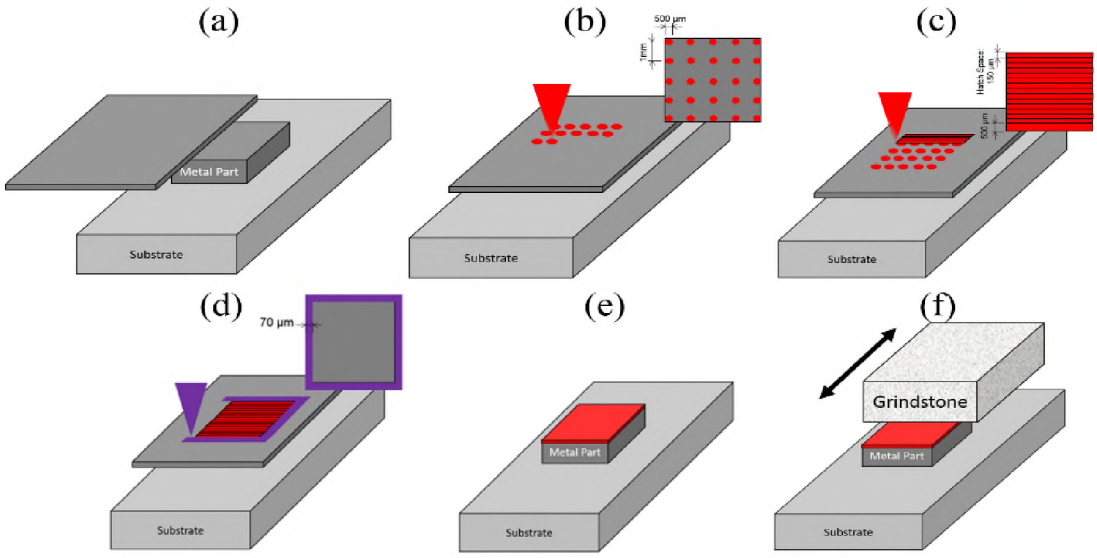

Figure 2. Schematic illustrations of the six steps in the LFP process for the fabrication of each layer: (a) foil feeding; (b) spot welding; (c) pattern welding; (d) contour cutting; (e) excess foil removing; and (f) surface flattening.

In this study, a 12.8-mm-thick 304L SS plate was used as the substrate. A 125 µm thick foil was used for every layer. For spot welding, the laser power was 400 W, the laser dwell time for each spot was 0.3 milliseconds, and the distance between two neighboring spots was 1 mm. For cutting the pattern's contour, the pulse energy was 0.16 millijoules with the pulse repetition rate of 4 kHz, and the cutting speed was 1 mm/s. To apply proper process parameters for conduction-mode and keyhole-mode laser welding in pattern welding, a preliminary study was conducted to investigate the formation of melt pool in the single-track laser welding. Only 304L SS foil was used in this study, and the boiling temperature, thermal conductivity, thermal diffusivity and laser absorption coefficient in Eq. (1) were constant. We set the laser power density (I) and laser spot size (σ) constant to make ut a constant. Thus the melt pools of conduction-mode and keyhole-mode welding could be created at different laser scanning speeds to result in different

aspect ratios of the melt pool. Because ut was 294 mm/s, which could be calculated by substituting the coefficients in Table 1 into Eq. (1), the scanning speeds of 100, 200, 300, and 400 mm/s were used at a constant laser power of 400 W to weld a layer of foil on the substrate to result in various depths and widths of the melt pool for conduction-mode and keyhole-mode welding.

The desirable process parameters for conduction-mode or keyhole-mode laser welding were chosen through a parametric study to build LFP-fabricated 304L SS test parts with the dimensions of 18 mm (length) × 12 mm (width) × 10 mm (height), as shown in Figure 3. In Figure 3(a), the X-axis is parallel to the laser scanning direction; the Y-axis is perpendicular to the laser scanning direction; and the Z-axis is parallel to the part building direction.

Table 1. Properties of 304L SS and laser beam

	Property	304L SS
304L SS [30,31,32,33]	Boiling temperature (K)	3,100
	Thermal conductivity (W m^{-1} K^{-1})	14
	Thermal diffusivity (m^2 s^{-1})	0.37×10^{-6}
	Laser absorption coefficient	0.38
Laser beam	Spot size (mm)	0.16
	Laser power density (W cm^{-2})	4×10^{6}

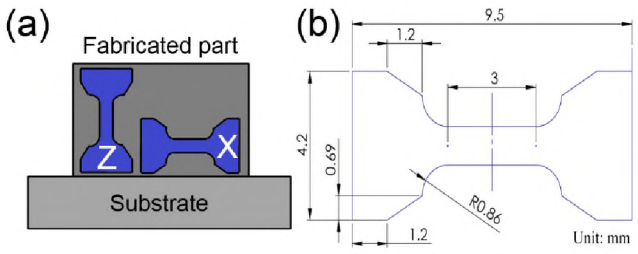

Figure 3. (a) side view of a 304L SS part fabricated by LFP showing how tensile specimens were extracted along the laser scanning direction (X) and layer building direction (Z); (b) dimensions of the tensile specimen.

2.2. CHARACTERIZATION

The LFP-fabricated 304L SS specimens were sliced, polished, and electro-etched for analysis. The polishing procedure followed the standard metallographic techniques using the following: #320 grind paper; 9 μm, 3 μm, and 1 μm diamond suspensions; and 0.04 μm silica. The electro-etching process immersed 304L SS specimens in a diluted nitric solution (70% nitric acid and 30% deionized water) at 1.5 volts. Then the microstructure and the melt pool were characterized by using an optical microscope (OM, Nikon Epiphot 200), and a scanning electron microscope (SEM, Helios Nanolab 600) equipped with a electron backscattered diffraction (EBSD) detector. The porosity was obtained by calculating the area of each pore on the OM images of the cross-sections in the XY and YZ planes with a total area of 21.7 mm2. The total area of pores was measured by ImageJ software [34]. The EBSD patterns had a scanning area of 600 × 600 μm2 with a step size of 2 μm. The average grain size in each EBSD pattern was calculated by following the ASTM E2627-13 standard [35].

The tensile strengths of the LFP-fabricated 304L parts using the two different laser welding modes were measured along the layer building direction (i.e., indicated by "Z") and along the laser scanning direction (i.e., indicated by "X"). The tensile specimens were 1 mm thick and they were cut using wire electrical discharge machining (EDM) as shown in Figure 3(a). An Instron machine was used to measure the tensile specimens with a clip-on extensometer at room temperature with the crosshead speed of 0.015 mm/mm/min (strain rate per minute). Seven LFP-fabricated tensile specimens in the X and Z directions and the conduction-mode and keyhole-mode of laser welding were measured, and the mean values with the standard deviations were reported. The micro-

hardness was measured using a Vickers micro-hardness tester (Struers, Duramin 5) with 2 kgf load and 10 s loading duration following the ASTM E92-17 standard: Standard Test Methods for Vickers Hardness of Metallic Materials [36]. The 2 kgf load could create a wide-range indentation mark to get an average hardness. The reported micro-hardness value was the average of 10 indentation measurements with a standard deviation. The two-way ANOVA statistical analysis was used to analyze the tensile test results with $p<0.001$.

3. RESULTS AND DISCUSSION

3.1. SINGLE-TRACK LASER WELDING

Single-track scan lines were created by welding a foil upon the substrate using the different laser scanning speeds of 100, 200, 300 and 400 mm/s and a constant laser power of 400 W. The top-surface (X-Y plane) and vertical cross-section (Y-Z plane) morphologies are shown in Figure 4. The average depth (D), width (W), and aspect ratio (AR) of the four melt pools with different scanning speeds were also shown in Figure 4. Based on the melt pool geometries in the figure and their ARs, it can be concluded that the laser welding at the scanning speed of 100 mm/s and 200 mm/s were keyhole-mode welding (its shape similar to a keyhole) while the others were conduction-mode laser welding (its shape similar to a semicircle). In the keyhole-mode laser welding, coarse ripples were observed on the surface morphology at the scanning speed of 100 mm/s while fine ripples were observed at the scanning speed of 200 mm/s, as shown in Figures 4(a) and 4(b). The ripples increased surface roughness. Besides ripples, pores were

observed in the sample (e.g., the red arrow mark in Figure 4(e)) obtained at the 100 mm/s scanning speed. From the aspect of laser energy input, the energy input at 100 mm/s scanning speed applies redundant energy, compared to the energy input at 200 mm/s scanning speed, to create sound bonding on the foil thickness of 125 μm between layers, but it could cause side-effects (e.g., foil distortion) during the fabrication of metal parts. Therefore, the scanning speed of 200 mm/s was more desirable than 100 mm/s for keyhole-mode laser welding because pores were not observed and ripples were relatively fine. In the conduction-mode laser welding, coarse ripples were not observed on the surface at both 300 mm/s and 400 mm/s as shown in Figures 4(c) and 4(d) because less power input alleviates the flow of melt pool. Although the melt pool depths in both Figures 4(g) and 4(h) were greater than the layer foil thickness of 125 μm, the larger depth should be selected to prevent potential un-melted defects occurring in multi-layer fabrication due to the existence of melt pool depth fluctuation. Therefore, hereinafter in this study, the scanning speed of 200 mm/s and 300mm/s at the laser power of 400W were selected for the keyhole-mode and conduction-mode laser welding, respectively, to build 304L SS parts using the LFP process.

3.2. MICROSTRUCTURE CHARACTERIZATION

Polished cross-section OM images in the Y-Z plane of LFP-fabricated 304L SS parts using conduction-mode and keyhole-mode laser welding are shown in Figures 5(a) and 5(b), respectively. Their porosities based on pores in the XY and YZ cross-sections were 0.1 % and 0.5 % in the conduction-mode and keyhole mode samples, respectively. Etched cross-sectional OM and SEM images are shown in Figures 5(c)-5(f). In Figures

5(d) and 5(f), pores in keyhole-mode welding specimens were found at the bottom side of melt pool because those pores were formed due to the collapse of keyhole during keyhole-mode laser melting [15]. The size of pores in Figure 5(e) is smaller than 10 μm while the size of pores in Figure 5(f) is ~25 μm. The average depth, width, and aspect ratio of twenty melt pools resulting from the conduction-mode laser welding were 189 ± 19 μm, 285 ± 20 μm, and 0.7, respectively; see Figure 5(e). The average depth, width, and aspect ratio of melt pools resulting from the keyhole-mode laser welding were 363 ± 27 μm, 336 ± 17 μm, 1.1, respectively; see Figure 5(f).

The microstructures of melt pools of conduction-mode and keyhole-mold welded AM parts are shown in Figure 6. In Figures 6(a) and 6(b), dendritic structures were observed in the Y-Z plane of both modes. The microstructures of both modes in the X-Y plane showed cellular structures at the boundaries of melt pools in Figures 6(c) and 6(d), where the cell spacings, i.e., distances between cells, of the conduction-mode and keyhole-mode welding were approximately 0.56 μm and 1.03 μm, respectively. The cell spacing ($\lambda 1$), was estimated from the length of the measured green line divided by the number of cells in Figures 6(c) and 6(d). The cellular structures were found only at the boundaries of melt pools because the temperature gradient of melt pool at the center location was smaller than that at the boundary [29]. The cell spacing could be used to estimate the highest cooling rate of melt pool as follows [37,38]:

$$\lambda_1 = 80\dot{T}^{-0.33} \tag{2}$$

where λ_1 is the cell spacing and $\dot{T}$ is the melt pool cooling rate during solidification. Thus, the cooling rates of conduction-mode and keyhole-mode welding were 3.4×10^6 K/s and 0.53×10^6 K/s, respectively.

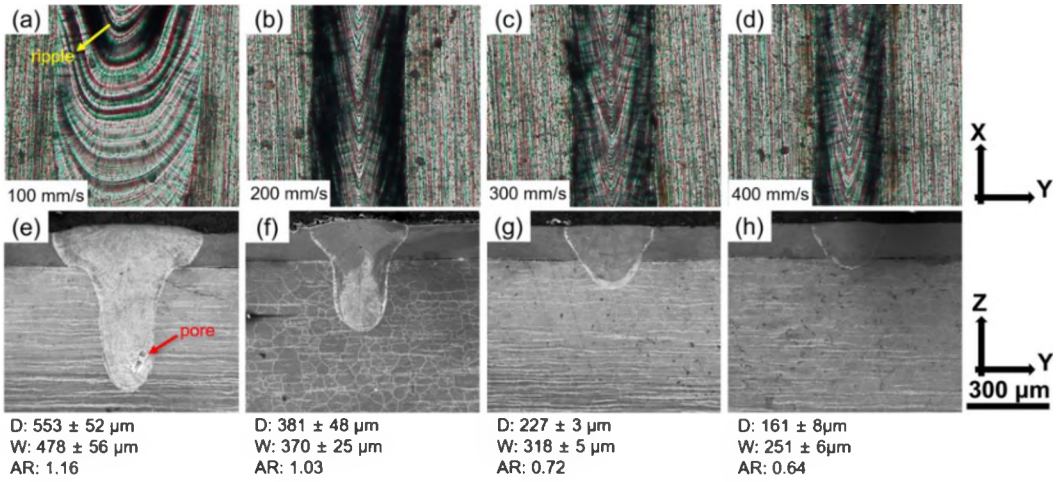

Figure 4. Single-track surface morphology (X-Y plane) OM images at a laser power of 400 W and the scan speed of (a) 100 mm/s, (b) 200 mm/s, (c) 300 mm/s, and (d) 400 mm/s; the corresponding cross-section morphology (Y-Z plane) SEM images are shown in (e)-(h).

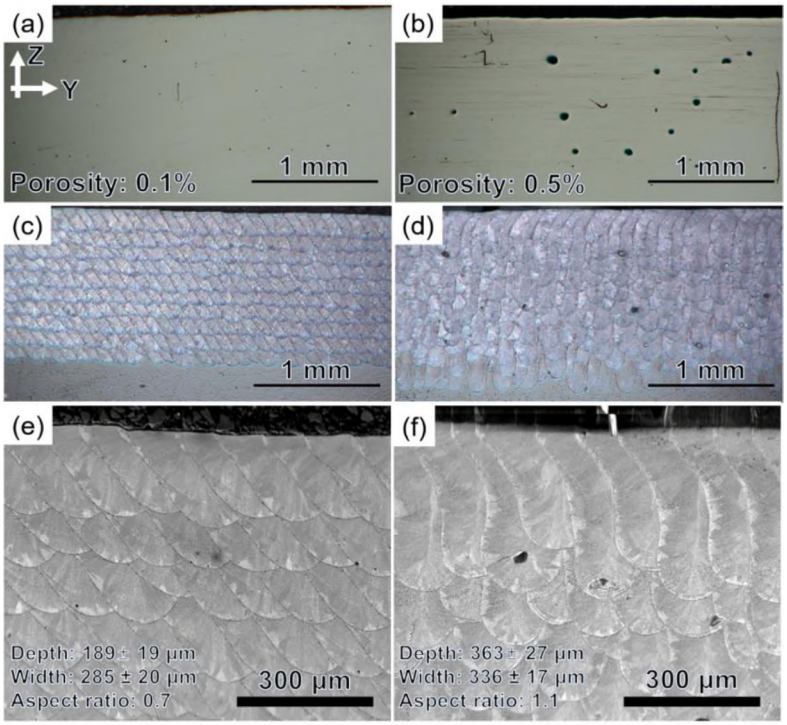

Figure 5. Polished cross-section OM images of (a) conduction mode and (b) keyhole mode; etched cross-section OM images of (c) conduction mode and (d) keyhole mode; etched cross-sectional SEM images in the Y-Z plane of (e) conduction mode and (f) keyhole mode.

3.3.MECHANICAL PROPERTIES

The mechanical properties and stress-strain curves of 304L SS parts made by two welding modes were measured along X (parallel to the laser scanning direction) and Z (parallel to the part building direction) axes by tensile tests using the Instron machine on seven tensile specimens, and the measured results are shown in Figure 7. It can be seen that two welding modes exhibited comparable yield strength (YS) and ultimate tensile strength (UTS) in the same directions, but the ductility of conduction-mode samples was 5% higher (69% vs. 64%) in the X-axis direction and 23% higher (94% vs. 71%) in the Z-axis direction than those of keyhole-mode samples. The YS and UTS in the X-axis direction were higher than those in the Z-axis direction for both welding modes, while the ductility in the Z-axis direction was higher than that the X-axis direction. The ANOVA analysis was used to analyze YS, UTS, and ductility differences between the different welding modes, measurement directions, and their interactions, and the results are given in Table 2. Based on the ANOVA results, there were no statistically significant differences ($p>0.001$) between the two welding modes in YS and UTS. Moreover, the differences in YS and UTS between X and Z directions were significantly different ($p<0.001$) for both welding modes. Furthermore, the ductility was significantly different for both different welding modes and different measurement directions.

Based on the stress-strain curves in Figure 7, the energy absorption per unit volume (Eabsorption) to induce material failure can be calculated using the following equation [39]:

$$E_{absorption} = \int \sigma(\varepsilon)\, d\varepsilon \tag{3}$$

The calculated energy absorption of conduction-X, conduction-Z, keyhole-X, and keyhole-Z were 484±14.9, 615±12.06, 447±23.6, and 471±31.99 MJ/m3, respectively. Thus, the 304L SS parts fabricated by conduction-mode laser welding had higher tensile toughness than the parts fabricated by keyhole-mode laser welding while their YS and UTS were similar. Based on the measured tensile properties, both welding modes formed strong bonding between the bulk metallic piece and thin metallic sheet but keyhole-mode laser welding would excessively apply heat energy input and may deteriorate the mechanical properties (e.g., poor ductility due to pores).

The hardness of LFP-fabricated parts was measured. The Vickers' hardnesses of keyhole-mode welding parts in the X-Y and Y-Z planes were 2.09 ± 0.06 GPa and 2.24 ± 0.08 GPa, respectively. The hardnesses of conduction-mode welding parts in the X-Y and Y-Z planes were 2.14 ± 0.09 GPa and 2.22±0.06 GPa, respectively. The average hardnesses in the Y-Z plane were slightly higher than those in the X-Y plane for both modes. No hardness difference was found between two modes in ANOVA analysis.

3.4.CRYSTALLOGRAPHIC TEXTURE CHARACTERIZATION

The EBSD band contrast and orientation maps for the conduction-mode and keyhole-mode welding samples are shown in Figure 8 for a scanning area of 600 × 600 μm2. The average grain sizes for the conduction-mode samples in the X-Y and Y-Z planes were 8.7 ± 0.5 and 11.9 ± 3.1 μm, respectively, while the average grain sizes for the keyhole-mode samples in the X-Y and Y-Z planes were 7.7 ± 0.5 μm and 9.3 ± 1.6 μm, respectively. The equiaxed grains in the X-Y plane in both modes, as shown in Figures 8(b) and 8(f), were finer than the grains in the Y-Z plane as shown in Figures

8(d) and 8(h). Moreover, the grain structures in the Y-Z plane for the two modes were distinctly different from each other. In Figure 8(d), most grains in the conduction mode grew along the Z-axis direction except for the last layer, while most of the grains in the keyhole mode grew in the direction perpendicular to the Z-axis direction, as shown in Figure 8(h). Therefore, the long axis of the conduction-mode columnar grains was parallel to the Z-axis direction, while the long axis of the keyhole-mode columnar grains was perpendicular to the Z-axis direction. As a result, this preferential grain orientation caused the conduction-mode columnar grains to have lower grain boundary interface density than the keyhole-mode columnar grains in the Z-axis direction. Because of the interface density difference, the resistance for the dislocation movement in the Z-axis direction will be less in the conduction mode than the keyhole mode. Therefore, plastic deformation can occur more easily and thus the ductility is higher in the Z-axis direction for the conduction-mode welding [40]. The difference in grain boundary interface density in the Z-axis direction between the two welding modes is the main contributing factor of the large difference in ductility (71% for keyhole mode vs. 94% for conduction mode) in the Z-axis direction between the two modes in the tensile test. However, there is no great difference in grain boundary interface density in the X-axis direction between the two welding modes, and thus the ductility difference in the X-axis direction is relatively small (64% for keyhole mode vs. 69% for conduction mode) for the two welding modes.

To further investigate the grain structures in the melt pool produced in the two welding modes, the grain structures of a single melt pool were measured by the EBSD, and the results are presented in Figure 9. In this figure, the melt pool is divided into the top zone and the bottom zone. Because of the multiple-layer fabrication, the top zone of

each layer will be re-melted and re-crystalized during the next-layer fabrication while the bottom zone will not be re-melted and thus its grain structure remains unchanged. Consequently, the grain structures of LFP-fabricated parts will be similar to the bottom zone of the melt pool for all layers except the last layer. The grains of the keyhole-mode melt pool grow mostly along the Y-axis direction while the grains of the conduction-mode melt pool grow mostly along the Z-axis direction. This observation qualitatively agrees with Wang's simulation results [41], which presented a similar grain growth behavior of melt pool in the conduction and keyhole welding modes for a single-layer fabrication of laser powder-bed fusion process.

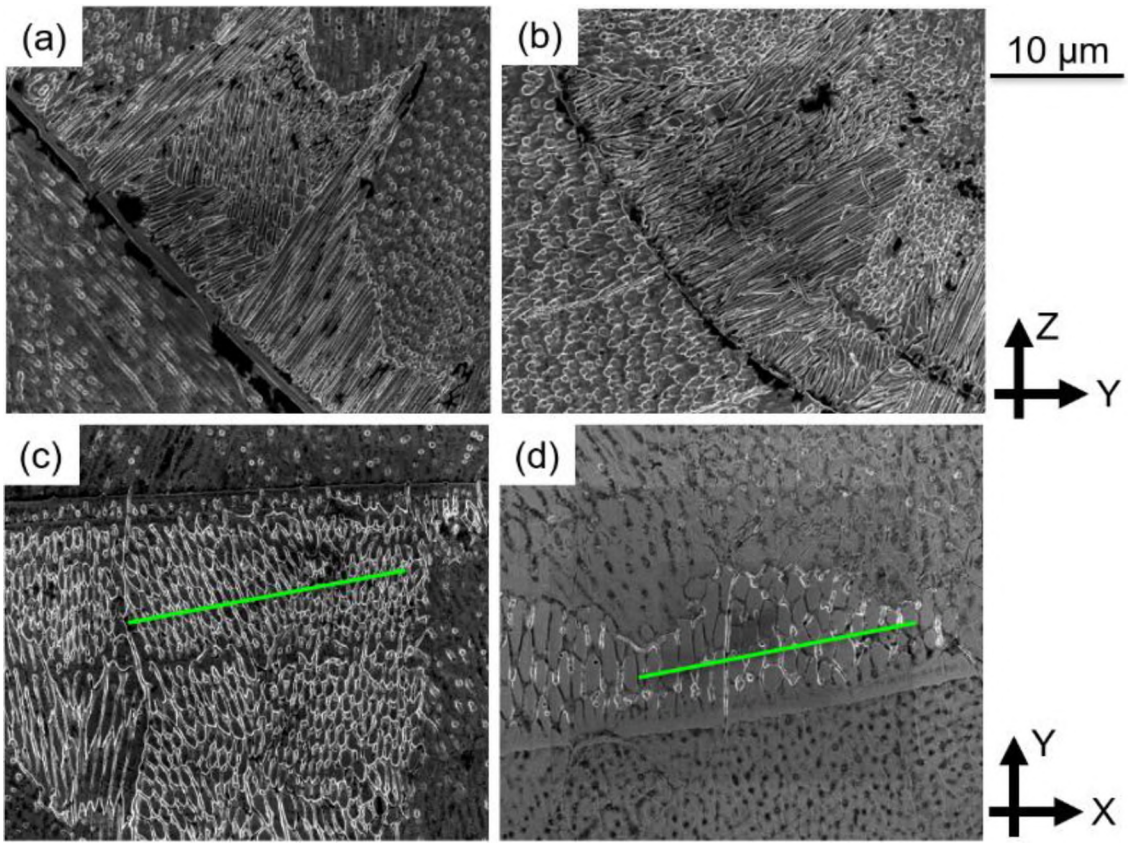

Figure 6. Dendritic microstructure of (a) conduction-mode welded AM part and (b) keyhole-mode welded AM part in the Y-Z plane; cellular microstructure of (c) conduction-mode part and (d) keyhole-mode part in the X-Y plane.

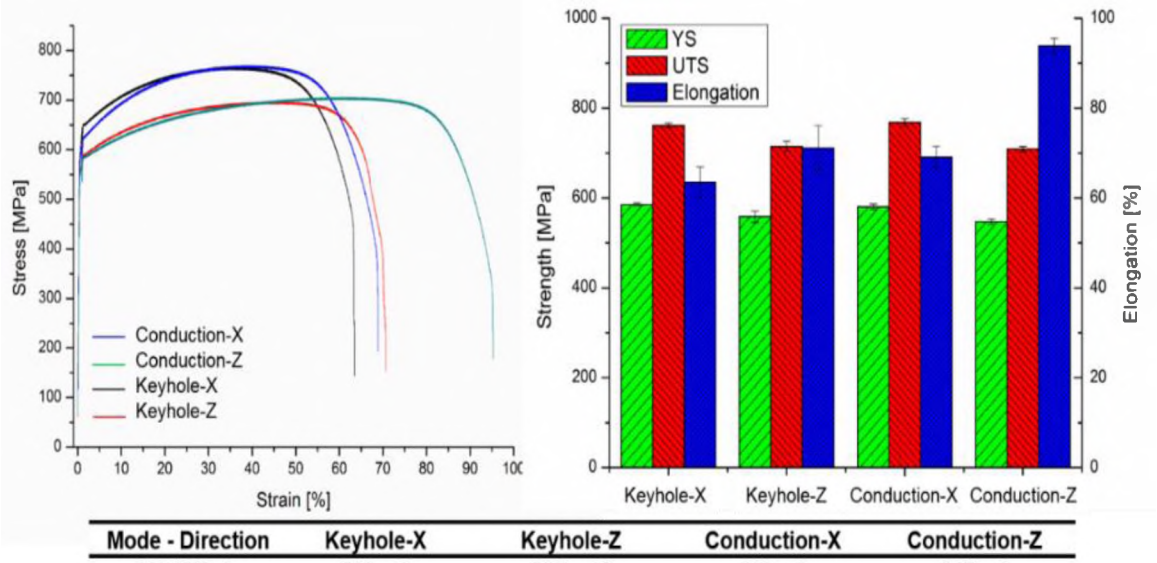

Mode - Direction	Keyhole-X	Keyhole-Z	Conduction-X	Conduction-Z
YS (MPa)	585 ± 3	558 ± 12	580 ± 6	547 ± 6
UTS (MPa)	761 ± 5	715 ± 11	768 ± 8	709 ± 6
Elongation (%)	64 ± 3	71 ± 5	69 ± 3	94 ± 2

Figure 7. Tensile properties of the LFP-fabricated parts using keyhole-mode and conduction-mode welding in the laser scanning direction (X) and in the part building direction (Z).

Table 2. ANOVA analysis of tensile properties

Response	Source	P-Value	R^2
Yield Strength	Mode	0.007	80.9%
	Direction	0.000	
	Mode*Direction	0.305	
Ultimate Tensile Strength	Mode	0.850	92.05
	Direction	0.000	
	Mode*Direction	0.043	
Elongation	Mode	0.000	92.4%
	Direction	0.000	
	Mode*Direction	0.000	

*p<0.001

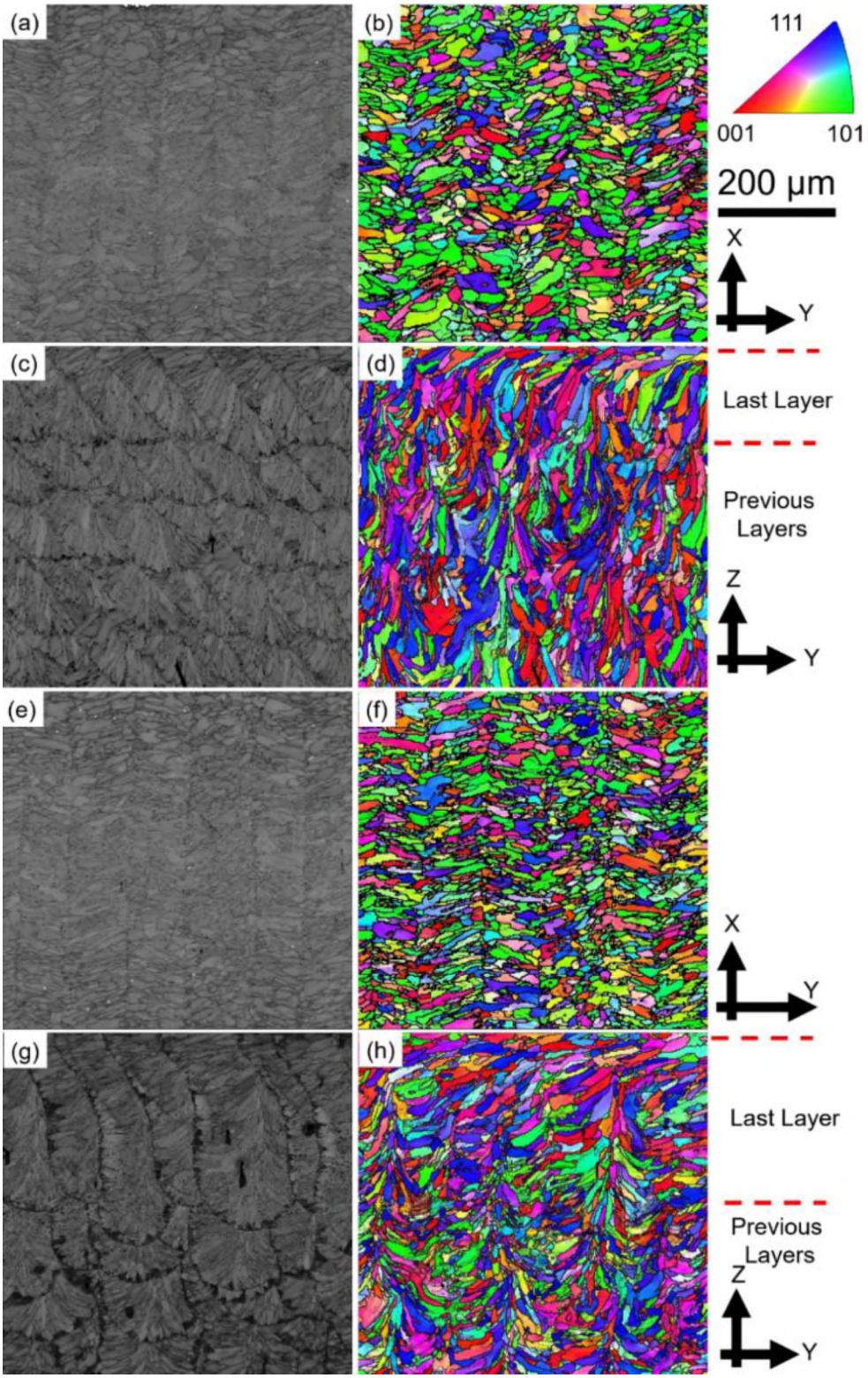

Figure 8. Band contrast and EBSD patterns of (a) & (b): conduction mode in the X-Y plane; (c) & (d): conduction mode in the Y-Z plane; (e) & (f): keyhole mode in the X-Y plane; (g) & (h): keyhole mode in the Y-Z plane.

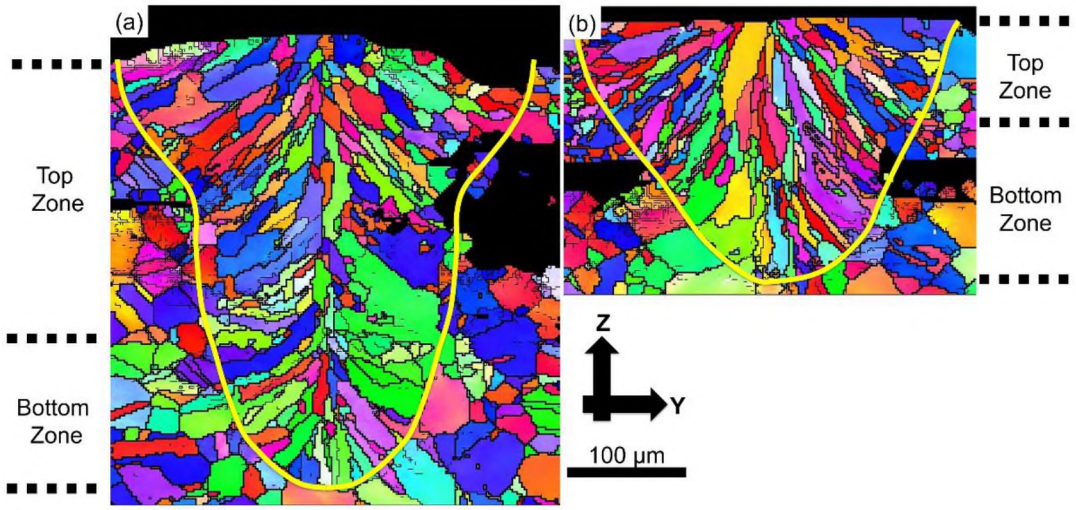

Figure 9. EBSD patterns of a single melt pool using (a) the keyhole-mode and (b) conduction-mode laser welding. The yellow line shows the boundary of melt pool. The dark area indicates no data acquired.

4. CONCLUSION

The 304L SS parts fabricated by the laser-foil-printing process with conduction-mode and keyhole-mode welding have been investigated experimentally, with the porosity, microstructure, and tensile properties of the fabricated parts compared for these two welding modes. The results showed that the parts fabricated in the conduction mode had lower porosity (0.1% vs. 0.5%) than those fabricated in the keyhole mode. Most pores in the keyhole-mode welding parts were found at the bottom of the solidified melt pool due to the keyhole collapse. Microstructure characterization for the fabricated parts by both welding modes showed that dendritic structures existed in the Y-Z plane and cellular structures existed in the X-Y plane, where X-axis is the laser scanning direction and Z-axis is the part building direction. The existence of these two different microstructures is mainly due to the large differences in cooling rates within and on the

boundary of the melt pool. Based on the ANOVA analysis, the yield strength and ultimate tensile strength of the parts are comparable for the two welding modes in both the laser scanning direction and the part building direction. However, the ductility of conduction-mode samples was 5% higher (69% vs. 64%) in the X-axis direction and 23% higher (94% vs. 71%) in the Z-axis direction than those of keyhole-mode samples. The main contributing factor of the large difference in ductility in the Z-axis direction is the substantial difference in grain boundary interface density along the Z-axis direction between the two welding modes, which is verified by the EBSD results that showed most grains resulted from the conduction-mode welding grew in the Z-axis direction while most grains resulted from the keyhole-mode welding grew in the direction perpendicular to the Z-axis.

ACKNOWLEDGEMENTS

This research work was supported by the Department of Energy [grant number DE-FE0012272] and by the Intelligent Systems Center at the Missouri University of Science and Technology. The help and suggestions of Dr. Hai-Lung Tsai on this research are highly appreciated.

REFERENCES

[1] Blackburn J. Laser welding of metals for aerospace and other applications. Woodhead Publishing Limited; 2012. doi:10.1533/9780857095169.1.75.

[2] Graudenz M, Baur M. Application of laser welding in the automotive industry. Handbook of Laser Welding Technologies. 2013:555-74. doi:10.1533/9780857098771.4.555.

[3] Lin TC, Cao C, Sokoluk M, Jiang L, Wang X, Schoenung JM, Lavernia EJ, Li X. Aluminum with dispersed nanoparticles by laser additive manufacturing. Nature Communications 2019;10:1–9. doi:10.1038/s41467-019-12047-2.

[4] Raghavan A, Wei HL, Palmer TA, DebRoy T. Heat transfer and fluid flow in additive manufacturing. Journal of Laser Applications 2013;25:052006. doi:10.2351/1.4817788.

[5] Huang L, Hua X, Wu D, Ye Y. Role of welding speed on keyhole-induced porosity formation based on experimental and numerical study in fiber laser welding of Al alloy. International Journal of Advanced Manufacturing Technology 2019;103:913–25. doi:10.1007/s00170-019-03502-x.

[6] Akman E, Demir A, Canel T, Sinmazçelik T. Laser welding of Ti6Al4V titanium alloys. Journal of Materials Processing Technology 2009;209:3705–13. doi:10.1016/j.jmatprotec.2008.08.026.

[7] Meco S, Pardal G, Ganguly S, Williams S, McPherson N. Application of laser in seam welding of dissimilar steel to aluminum joints for thick structural components. Optics and Lasers in Engineering 2015;67:22–30. doi:10.1016/j.optlaseng.2014.10.006.

[8] Torkamany MJ, Malek Ghaini F, Poursalehi R, Kaplan AFH. Combination of laser keyhole and conduction welding: Dissimilar laser welding of niobium and Ti-6Al-4V. Optics and Lasers in Engineering 2016;79:9–15. doi:10.1016/j.optlaseng.2015.11.001.

[9] Steen W., Mazumder J. (2010) Basic Laser Optics. In: Laser Material Processing. Springer, London. doi:10.1007/978-1-84996-062-5_3.

[10] Steen W., Mazumder J. (2010) Laser Welding. In: Laser Material Processing. Springer, London. doi:10.1007/978-1-84996-062-5_5.

[11] Guo SH, Zou JL, Xiao RS. Characterizations of welding mode transformation process during 1-μm and 10-μm laser welding. AIP Advances 2020;10. doi:10.1063/1.5132776.

[12] Lee JY, Ko SH, Farson DF, Yoo CD. Mechanism of keyhole formation and stability in stationary laser welding. Journal of Physics D: Applied Physics 2002;35:1570–6. doi:10.1088/0022-3727/35/13/320.

[13] Verhaeghe F, Craeghs T, Heulens J, Pandelaers L. A pragmatic model for selective laser melting with evaporation. Acta Materialia 2009;57:6006–12. doi:10.1016/j.actamat.2009.08.027.

[14] Tobar MJ, Lamas MI, Yáñez A, Sánchez-Amaya JM, Boukha Z, Botana FJ. Experimental and simulation studies on laser conduction welding of AA5083 aluminum alloys. Physics Procedia 2010;5:299–308. doi:10.1016/j.phpro.2010.08.056.

[15] Zhou J, Tsai HL, Wang PC. Transport phenomena and keyhole dynamics during pulsed laser welding. Journal of Heat Transfer 2006;128:680–90. doi:10.1115/1.2194043.

[16] Martin AA, Calta NP, Khairallah SA, Wang J, Depond PJ, Fong AY, Thampy V, Guss GM, Kiss AM, Stone KH, Tassone CJ, Weker JN, Toney MF, Buuren TV, Matthews MJ. Dynamics of pore formation during laser powder bed fusion additive manufacturing. Nature Communications 2019;10:1–10. doi:10.1038/s41467-019-10009-2.

[17] King WE, Barth HD, Castillo VM, Gallegos GF, Gibbs JW, Hahn DE, Kamath C Rubenchik AM. Observation of keyhole-mode laser melting in laser powder-bed fusion additive manufacturing. Journal of Materials Processing Technology 2014;214:2915–25. doi:10.1016/j.jmatprotec.2014.06.005.

[18] Hung CH, Chang FY. Curve micromachining on the edges of nitinol biliary stent by ultrashort pulses laser. Optics & Laser Technology. 2017;90:1–6. doi:10.1016/j.optlastec.2016.10.018.

[19] Kou S, Limmaneevichitr C, Wei PS. Oscillatory Marangoni flow: A fundamental study by conduction-mode laser spot welding. Welding Journal 2011;90.

[20] Antony K, Arivazhagan N. Studies on energy penetration and Marangoni effect during laser melting process. Jounral of Engineering Science Technology. 2015;10:509–25.

[21] Sibillano T, Ancona A, Berardi V, Schingaro E, Basile G, Lugarà PM. Optical detection of conduction/keyhole mode transition in laser welding. Journal of Materials Processing Technology. 2007;191:364–7. doi:10.1016/j.jmatprotec.2007.03.075.

[22] Bäuerle D. (2011) Surface Melting. In: Laser Processing and Chemistry. Springer, Berlin, Heidelberg. doi:10.1007/978-3-642-17613-5_10.

[23] Metelkova J, Kinds Y, Kempen K, de Formanoir C, Witvrouw A, Van Hooreweder B. On the influence of laser defocusing in Selective Laser Melting of 316L. Additive Manufacturing 2018;23:161–9. doi:10.1016/j.addma.2018.08.006.

[24] Yang J, Han J, Yu H, Yin J, Gao M, Wang Z, Zeng X. Role of molten pool mode on formability, microstructure and mechanical properties of selective laser melted Ti-6Al-4V alloy. Materials and Design 2016;110:558–70. doi:10.1016/j.matdes.2016.08.036.

[25] Zafari A, Xia K. High Ductility in a fully martensitic microstructure: a paradox in a Ti alloy produced by selective laser melting. Materials Research Letters 2018;6:627–33. doi:10.1080/21663831.2018.1525773.

[26] Li Y, Shen Y, Leu MC, Tsai HL. Mechanical properties of Zr-based bulk metallic glass parts fabricated by laser-foil-printing additive manufacturing. Materials Science and Engineering A 2019;743:404–11. doi:10.1016/j.msea.2018.11.056.

[27] Hung CH, Sutton A, Li Y, Shen Y, Tsai HL, Leu MC. Enhanced mechanical properties for 304L stainless steel parts fabricated by laser-foil-printing additive manufacturing. Journal of Manufacturing Processes 2019;45:438–46. doi:10.1016/j.jmapro.2019.07.030.

[28] Chen C, Shen Y, Tsai HL. A foil-based additive manufacturing technology for metal parts. Journal of Manufacturing Science and Engineering, Transactions of the ASME 2017;139:1–6. doi:10.1115/1.4034139.

[29] Hung CH, Li Y, Sutton A, Chen WT, Gong X, Pan H, Tsai HL, Leu MC. Aluminum Parts Fabricated by Laser-Foil-Printing Additive Manufacturing: Processing, Microstructure, and Mechanical Properties. Materials 2020;13:414. doi:10.3390/ma13020414.

[30] Rai R, Elmer JW, Palmer TA, Debroy T. Heat transfer and fluid flow during keyhole mode laser welding of tantalum, Ti-6Al-4V, 304L stainless steel and vanadium. Journal of Physics D: Applied Physics 2007;40:5753–66. doi:10.1088/0022-3727/40/18/037.

[31] Tepylo N, Huang X, Patnaik PC. Laser-Based Additive Manufacturing Technologies for Aerospace Applications. Advanced Engineering Materials 2019;21:1–35. doi:10.1002/adem.201900617.

[32] Bergström D. The absorption of laser light by rough metal surfaces. Thesis 2008:226.

[33] Graves RS, Kollie TG, McElroy DL, Gilchrist KE. The thermal conductivity of AISI 304L stainless steel. International Journal of Thermophysics 1991;12:409–15. doi:10.1007/BF00500761.

[34] Dinda G.P., Dasgupta A.K., Bhattacharya S., Natu H., Dutta B., Mazumder J. Microstructural Characterization of Laser-Deposited Al 4047 Alloy. Metall Mater Trans. A. 2013;44A:2233-42. doi:10.1007/s11661-012-1560-3.

[35] ASTM E2627-13, Standard practice for determining average grain size using electron backscatter diffraction (EBSD) in fully recrystallized polycrystalline materials, ASTM International, West Conshohocken, PA, 2013. doi:10.1520/E2627-13.

[36] ASTM E92-17, Standard test methods for Vickers hardness and Knoop hardness of metallic materials. ASTM International, West Conshohocken, PA, 2017. doi:10.1520/E0092-17

[37] Fu JW, Yang YS, Guo JJ, Tong WH. Effect of cooling rate on solidification microstructures in AISI 304 stainless steel. Mater Sci Technol. 2008;24:941-4. doi:10.1179/174328408X295962.

[38] Ghayoor M, Lee K, He Y, Chang CH, Paul BK, Pasebani S. Selective laser melting of 304L stainless steel: Role of volumetric energy density on the microstructure, texture and mechanical properties. Additive Manufacturing. 2020;32:101011. doi: 10.1016/j.addma.2019.101011

[39] Conner RD, Choi-Yim H, Johnson WL. Mechanical properties of Zr 57Nb5al10cu15.4Ni12.6 metallic glass matrix particulate composites. J. Mater. Res. 1999;14:3292-7. doi:10.1557/JMR.1999.0445.

[40] Callister W, Rethwisch D. Materials science and engineering: an introduction. 2007;94:188-90. doi:10.1016/0025-5416(87)90343-0.

[41] Wang H, Zou Y. Microscale interaction between laser and metal powder in powder-bed additive manufacturing: Conduction mode versus keyhole mode. Int. J. Heat Mass Transf. 2019;142:118473. doi:10.1016/j.ijheatmasstransfer.2019.118473

IV. DEVELOPMENT AND EXPERIMENTAL STUDY OF AN AUTOMATED LASER-FOIL-PRINTING ADDITIVE MANUFACTURING SYSTEM

Chia-Hung Hung, Tunay Turk, M. Hossein Sehhat, Ming C. Leu

Department of Mechanical and Aerospace Engineering, Missouri University of Science and Technology, Rolla, MO, USA, 65409

ABSTRACT

This paper presents the development and experimental study of a fully automated system using a novel laser additive manufacturing technology, called Laser Foil Printing (LFP), to fabricate metal parts layer-by-layer. Test specimens and parts with different geometries were fabricated from 304L stainless steel foil using this system. The dimensions of the fabricated parts were measured, and the mechanical properties of the test specimens were characterized. The experimental results show that the dimensional accuracy of the LFP fabricated parts are good, and their mechanical strength and ductility are high and repeatable. The mechanical strength is higher than those of parts fabricated by laser powder bed fusion and directed energy deposition technologies.

1. INTRODUCTION

Laser Additive Manufacturing (LAM) has been increasingly used to fabricate a variety of components for industrial applications [1]. The LAM research has been largely focused on using a laser beam to heat up and melt a metal powder (e.g., inconel, titanium, aluminum) to build metallic parts layer by layer. LAM processes can be used to build

metal parts with complex geometries that are difficult to manufacture by traditional processes. However, because of the nature of powder, some drawbacks such as porosity and large powder surface area induced oxidation in the manufactured parts are difficult to overcome [2-4]. Also, the high price of powder is a major cost driver for typical LAM processes, which are often more expensive than traditional manufacturing processes [5].

We have developed a novel LAM process, called Laser Foil Printing (LFP), in recent years for fabricating metal parts layer by layer using metal foil as the feedstock. LFP is a laminated object manufacturing process that utilizes a dual-laser beam system to weld a foil onto the just built layer, forming a strong bond between them, and then to cut a contour of the built layer according to the CAD model. LFP can alleviate the issues associated with powder-based LAM processes due to its inherent advantages including the following : (1) smaller (foil vs. powder) surface area that reduces oxidation, (2) smaller volumetric reduction in the melting and solidification of foil vs. powder, (3) lower cost of metallic material in foil than powder form (e. g., $10-15/kg for 304L SS foil vs. $70-80/kg for 304L SS powder), and (4) relatively clean manufacturing environment with no inhalation and dust explosion hazards [6]. LFP has been demonstrated to fabricate amorphous and crystalline metal parts, including Zr-based metallic glass, 304L stainless steel, Al-1100, and AISI 1010, resulting in high part density and mechanical strength [6,7]. This process has also been demonstrated to build composite sandwich structures [8].

We have developed a novel LAM process, called Laser Foil Printing (LFP), in recent years for fabricating metal parts layer by layer using metal foil as the feedstock. LFP is a laminated object manufacturing process that utilizes a dual-laser beam system to

weld a foil onto the just built layer, forming a strong bond between them, and then to cut a contour of the built layer according to the CAD model. LFP can alleviate the issues associated with powder-based LAM processes due to its inherent advantages including the following : (1) smaller (foil vs. powder) surface area that reduces oxidation, (2) smaller volumetric reduction in the melting and solidification of foil vs. powder, (3) lower cost of metallic material in foil than powder form (e. g., $10-15/kg for 304L SS foil vs. $70-80/kg for 304L SS powder), and (4) relatively clean manufacturing environment with no inhalation and dust explosion hazards [6]. LFP has been demonstrated to fabricate amorphous and crystalline metal parts, including Zr-based metallic glass, 304L stainless steel, Al-1100, and AISI 1010, resulting in high part density and mechanical strength [6,7]. This process has also been demonstrated to build composite sandwich structures [8].

In the study described in the present paper, a fully automated LFP system was developed and used to fabricate 304L SS parts with various geometries. Part dimensions were measured using an optical microscope, and the part's mechanical properties were measured and characterized using standard tensile tests. The results show that LFP fabricated parts have higher strengths than those fabricated by the laser powder bed fusion (L-PBF) and directed energy deposition (DED) processes, and the ductilities of parts fabricated by the LFP, L-PBF and DED processes are comparable.

2. PROCESS OVERVIEW, CONSTRUCTED SYSTEM AND EXPERIMENTAL MEASUREMENTS

2.1. OVERVIEW OF LASER FOIL PRINTING (LFP) PROCESS AND SYSTEM

In our previous LFP studies [6,7,8], the metal parts were fabricated semi-automatically using an LFP system that consisted of a dual-laser subsystem (having an infrared laser and an ultraviolet laser) with an X-Y moving table and a clamping plate for fabrication of each layer. The spot welding, pattern welding, and laser cutting are performed automatically, but mechanical polishing and foil placement are done manually.

In the current study, we developed and constructed a fully automated LFP system that consists of the dual-laser subsystem, a 3-axis gantry subsystem with X-Y-Z moving stages, a roller-to-roller foil supply subsystem, and a foil clamping subsystem, as shown in Figure 1. One of two lasers is a continuous-wave IR fiber laser (IPG YLP-1000), with central wavelength = 1070 nm, for laser welding with the laser beam directed by a galvo-mirror scanner (SCANLAB hurrySCAN-30). The maximum power of this laser is 1000 W, its beam quality factor (M2) is 3.04, the F-θ lens focal length is 330 mm, and the laser spot size is ~160 μm. The other laser is a UV pulsed laser, with central wavelength = 355nm, for laser cutting. The maximum power of this laser is 10 W, and its pulse frequency and duration are 100 kHz and 30 ns, respectively. The focal length of the laser cutting head is 100 mm and the laser spot size is 40 μm. The IR scanner and the UV cutting head are aligned.

As shown in Figure 1, the roller-to-roller foil supply subsystem advances the foil supply after the fabrication of each layer. This subsystem consists of a stepper motor with two idler rollers to transport foil from the left-side roller to the right-side roller. The left-

side roller has a magnetic brake (IBT MC5-38) to apply a tension force for flattening the foil. The stepper motor is installed at the right-side roller and is used to pull the foil from the left to the right. The foil clamping subsystem consists of a clamping plate and a two-rail linear stage, and is used to clamp the supplied foil onto the substrate or a previously fabricated layer for the laser spot welding.

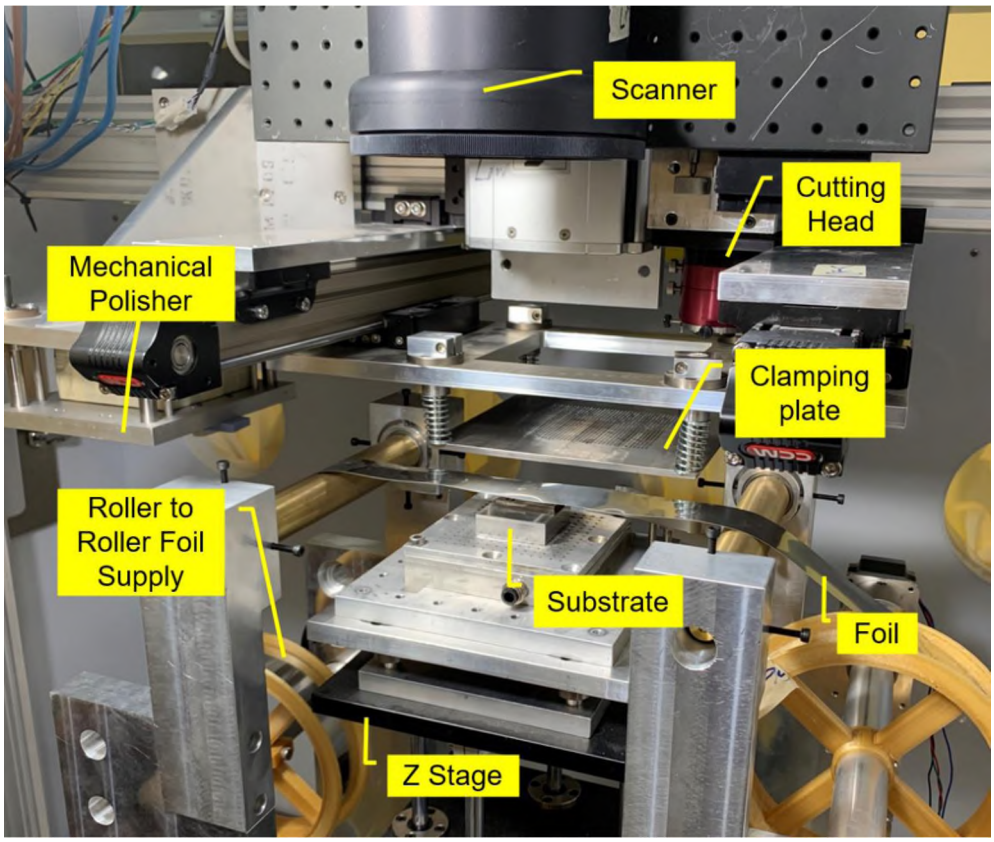

Figure 1. The automated Laser Foil Printing (LFP) system.

2.2. AUTOMATED LASER FOIL PRINTING PROCESS STEPS

To automatically fabricate a metal part using the automated LFP system, there are six steps for fabricating every layer, as illustrated in Figure 2. First, a new layer of metal foil is transported to the location on top of the substrate or a previously built layer as

shown in Figure 2(a). Then the clamping plate is transported to the foil location and a force is applied to clamp the foil. The clamping plate has a large number of small holes. Then the IR laser beam passes through these holes to perform spot welding to fix the foil onto the substrate or a previous layer; see Figure 2(b). After laser spot welding, the clamping plate moves away, and the next step is laser pattern welding (Figure 2(c)), which welds a selective area of foil onto the previous layer. The pattern welding is done under an argon shielding atmosphere with ~1% oxygen to prevent oxidation. The spot welding and pattern welding are both performed using an IR fiber laser. The next step is to cut a contour from the welded pattern using a UV pulsed laser; see Figure 2(d). After the UV cutting, the un-welded portion of the foil is removed; see Figure 2(e). The welded surface is then polished to arrive at a flat surface using the mechanical polisher, as shown in Figure 2(f), for the next-layer fabrication. The mechanical polishing is done by using a #80 grit grindstone. These six steps are repeated for each layer until the part fabrication is completed.

2.3. EXPERIMENTAL MEASUREMENTS

The 304L SS foil (Ulbrich Co.) used as the feedstock had the thickness of 0.125 mm. The dimensions of LFP fabricated 304L parts were measured using an optical microscope (OM, Nikon Epiphot 200). The yield strength (YS), ultimate tensile strength (UTS), and ductility of the fabricated parts were measured along the laser scan direction (X-axis) using tensile tests. The YS is the stress value at the strain of 0.2%; the UTS is the highest stress value in the tensile test; the ductility is the strain value at the break point. In order to eliminate the surface roughness effect on the mechanical properties, the

tensile specimens were cut from the LFP fabricated parts using wire electrical discharge machining (EDM). The miniature tensile bar has dimensions shown in Figure 3, following ASTM standards [7,9]. An Instron machine was used to measure the tensile specimens with a clip-on extensometer at the crosshead speed of 0.015 mm/mm/min (strain rate per minute). The YS, UTS and ductility were measured from eight LFP fabricated tensile specimens in the laser scan direction, and the mean values and standard deviations were reported. A surface profiler (Gocator 2300 series) was used to measure 2D surface profiles perpendicular to the laser scan direction (Y-axis) of the fabricated specimens. There were 1280 data points captured within a measured length of 12 mm in each surface profile. From each surface profile the distance between the highest point and the lowest point, Rt, can be obtained.

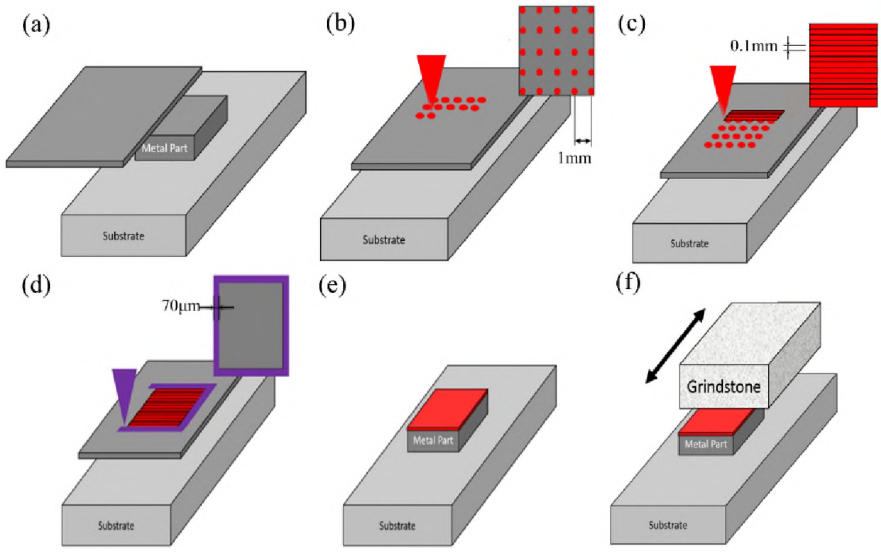

Figure 2. Key LFP process steps: (a) foil feeding, (b) spot welding, (c) pattern welding, (d) contour cutting, (e)excess foil removal, and (f) surface polishing.

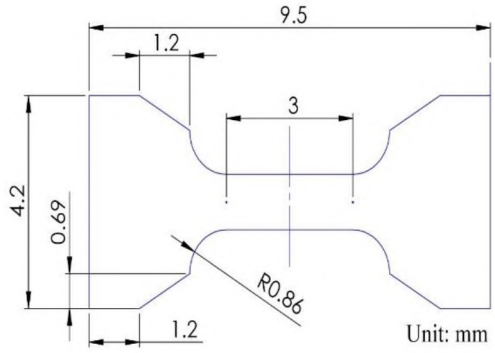

Figure 3. The dimensions of the tensile bar. The measurement unit is mm.

3. RESULTS AND DISCUSSION

3.1. MECHANICAL POLISHING

The mechanical polishing used a force of 3 kilograms with 30 strokes to remove the elevated edges caused by the contour cutting process in each layer. During the UV laser cutting, the cutting debris produced 50-100 μm burrs at the edges. If the elevated edges caused by the burrs were not removed, the foil would be burned in building the next layer because these elevated edges would form air gaps, preventing the laser energy from effectively conducting to the built layer underneath.

Figure 4 shows the surface profiles measured before and after the mechanical polishing, after the contour cutting, at two different X locations in a direction perpendicular to the laser scan direction. The Z-axis in Figure 4 is along the layer building direction. The elevated edges can be clearly seen in the surface profiles of Figures 4(a) and 4(c). These edges were removed after mechanical polishing, as shown in Figures 4(b) and 4(d). The R_t values are 126.5 μm and 73.5 μm, respectively, in Figures 4(a) and 4(b), and they are 164.2 μm and 95.0 μm, respectively, in Figures 4(c) and 4(d).

The mechanical polishing resulted in the reduction of R_t to <100 μm, which was small enough for successful pattern welding in building the next layer.

3.2. TEST PARTS' GEOMETRIES AND DIMENSIONS

Test parts were fabricated with 304L SS by using the automated LFP system. As examples, Figures 5 and 6 show two fabricated parts and their CAD models. The 5 mm-thick rectangular plate with an internal channel in Figure 5 was used to demonstrate the capability of the LFP system to fabricate a 3D part with internal features. Table 1 gives the measured data for several linear dimensions, in terms of the mean and standard deviation (STD) values calculated from six measurements. The differences between the measured means and the CAD model dimensions ranged from 0 mm to 0.06 mm, and the standard deviations of the measured data ranged from 0.01 mm to 0.07 mm. Figure 6 shows a 2 mm-thick rectangular plate with notches and rounded edges, including the LFP fabricated part and its CAD model. Table 2 gives the means and standard deviations of the measured data for one linear dimension, one radius of rounded edge, and four angles of notches in comparison with their values from the CAD model. From the data in Tables 1 and 2, it can be stated that the dimensional accuracy of parts fabricated by the LFP system needs further improvement. It should also be noted that the part's dimensional accuracy is mainly governed by the positional accuracy of the X-Y-Z moving stages in the gantry and the fineness of UV laser cutting, and the dimensional accuracy can be improved by using a gantry with better positional accuracy and a UV laser with finer beam quality.

3.3. MECHANICAL PROPERTIES

The stress-strain curves of eight 304L SS tensile specimens along the laser scan direction were measured by standard tensile tests. The obtained stress-strain curves are shown in Figure 7, and the derived mechanical properties are summarized in Table 3. The consistency of measurement can be observed from stress-strain curves in Figure 7. From the data in Table 3 it can be seen that the yield strength (YS) at 0.2 % strain for the eight specimens ranged between 617 MPa and 639 MPa, with a mean of 632 MPa and a standard deviation (STD) of 7.5 MPa. The ultimate tensile strength (UTS) ranged between 808 MPa and 822 MPa, with a mean of 815 MPa and a STD of 5 MPa. The strain at the break point ranged between 67% and 72 %, with a mean of 69% and a STD of 1.7%.

The measured mechanical properties of the LFP fabricated specimens are compared with the mechanical properties of parts fabricated by the laser powder bed fusion (L-PBF) process and the directed energy deposition (DED) process, two of the most popular laser additive manufacturing (LAM) processes. Both L-PBF and DED processes use metal powder as the feedstock to fabricate metal parts, while the LFP process uses metal foil as the feedstock. The UTS and ductility of 304L SS parts fabricated by these three LAM processes are compared in Figure 8, with the data for the L-PBF and DED processes taken from the literature [6,10-14]. It can be seen from this figure that the UTS of L-PBF fabricated parts ranged between 665 MPa and 712 MPa and its ductility ranged between 36% and 72%. For DED fabricated parts, the UTS ranged between 710 MPa and 730 MPa and the ductility ranged between 51% and 59%. In comparison, for our LFP fabricated parts, the UTS ranged between 761 MPa and 816

MPa and the ductility ranged between 64% and 69%. Therefore, the UTS of the LFP fabricated parts is 10%-20% higher than the UTS of parts fabricated by the L-PBF and DED processes. In terms of ductility, it can be seen from Figure 8 that the ductilities of parts fabricated by these three LAM processes are comparable. The differences in UTS between metal parts fabricated by LFP vs. L-PBF/DED are mainly due to the difference in thermal conductivity between metal foil and metal powder. Thermal conductivity is much higher for metal foil than for metal powder, thus the cooling and solidification of melt pool is faster in the LFP process vs. the L-PBF and DED processes. Specifically, the thermal conductivity coefficient of 304L powder (0.186 Wm-1K-1) is only ~1.3% of the thermal conductivity coefficient of 304L foil (~14 Wm-1K-1) [15].

Also included in Figure 8 is the data of UTS and ductility of 304L SS parts fabricated by the semi-automatic LFP system from our previous research, in order to show the differences between the present automated LFP system and the previous semi-automated LFP system. From Figure 8 it can be seen that the UTS and ductility of parts fabricated by the automated LFP system are both slightly higher than those resulted from the semi-automated LFP system. This is due to higher process consistency in the building of every layer by the automated LFP system vs. the semi-automated LFP system.

The cooling rate of melt pool affects the grain growth behaviour during solidification, resulting in varying mechanical properties of the part after solidification. We have reported previously that LFP fabricated parts have finer grains than L-PBF fabricated parts because of faster cooling of the melt pool, which shortens the solidification time and grows a finer grain structure [6]. The higher strength in the LFP fabricated parts is mainly attributed to the finer grains. According to the Hall-Patch

relationship [16], parts with finer grains have higher strength yet can still have ductile property comparable to parts with coarser grains.

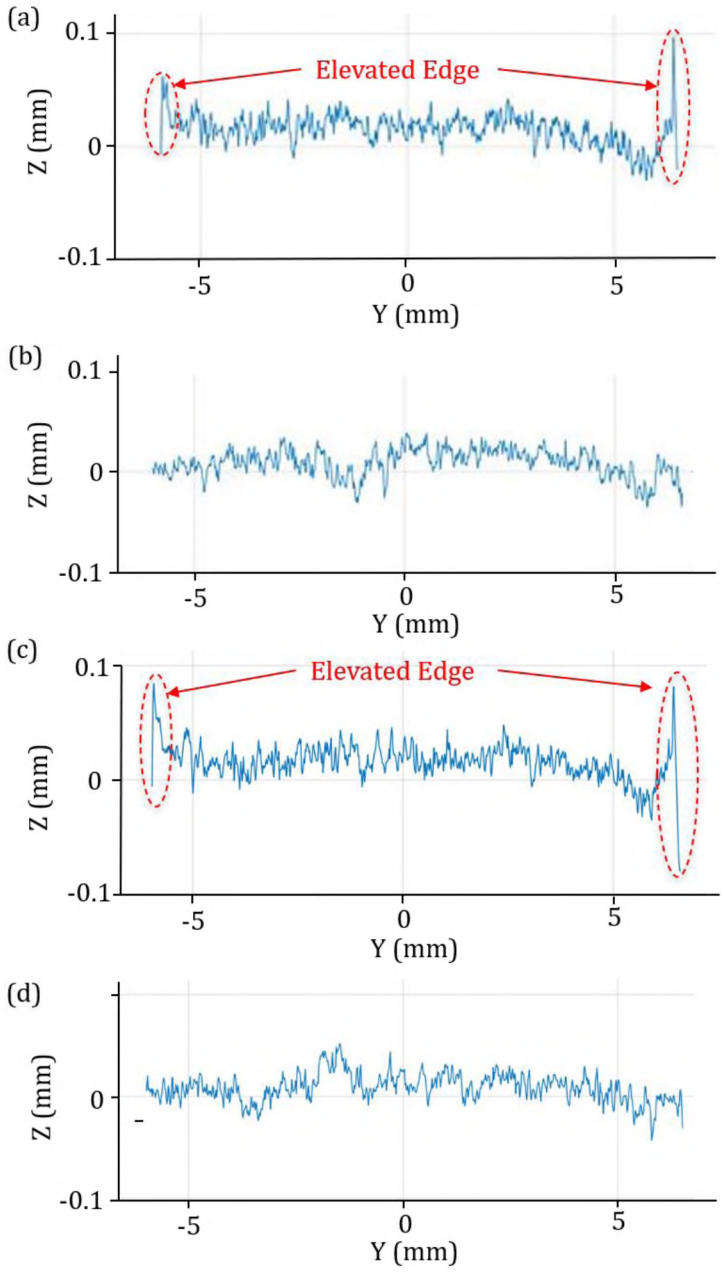

Figure 4. Surface profiles of a built layer at two different locations: (a, c) after contour cutting, and (b, d) after mechanical polishing.

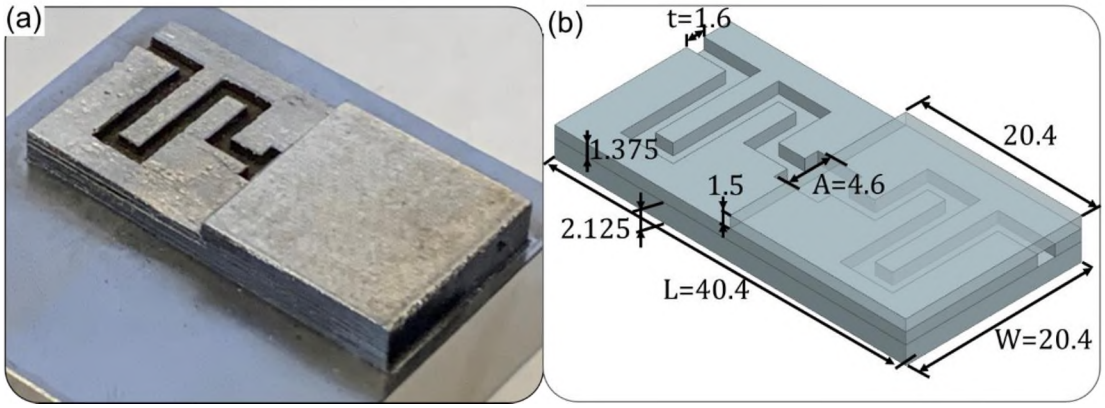

Figure 5. A rectangular plate with an internal channel.

Table 1. Measurements for the rectangular plate with an internal channel.

Measurements	L	W	t	A
CAD Design (mm)	40.4	20.4	1.6	4.6
Mean (mm)	40.39	20.46	1.61	4.6
Standard Deviation (mm)	0.04	0.01	0.02	0.07

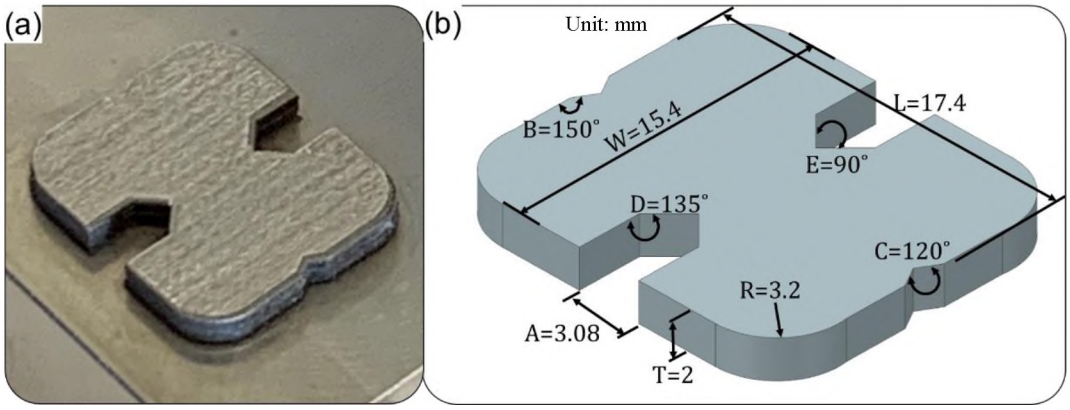

Figure 6. A rectangular plate with notches and rounded corners.

Table 2. Measurements for the rectangular plate with notches and rounded corners.

Measurements	R	A	B	C	D	E
CAD Design	3.2 mm	3.08 mm	150 °	120 °	135 °	90 °
Mean	3.32 mm	3.05 mm	145.37 °	112.76 °	132.7 °	91.26 °
Standard Deviation	0.19 mm	0.03 mm	1.42 °	2.53 °	1.73 °	0.95 °

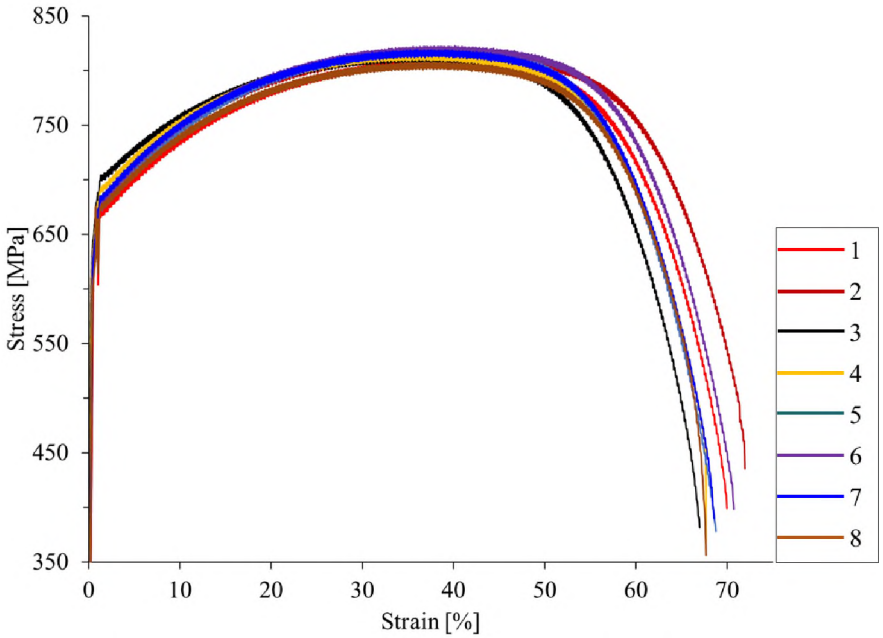

Figure 7. Stress-strain curves of eight LFP fabricated tensile specimens.

Table 3. Tensile properties of LFP test specimens.

Sample	1	2	3	4	5	6	7	8	Mean	STD	Error
YS (MPa)	630	636	632	636	625	638	639	617	632	7.5	1.2%
UTS (MPa)	810	817	814	816	821	822	819	808	816	5	0.6%
Strain (%)	70	72	67	68	69	71	69	68	69	1.7	2.5%

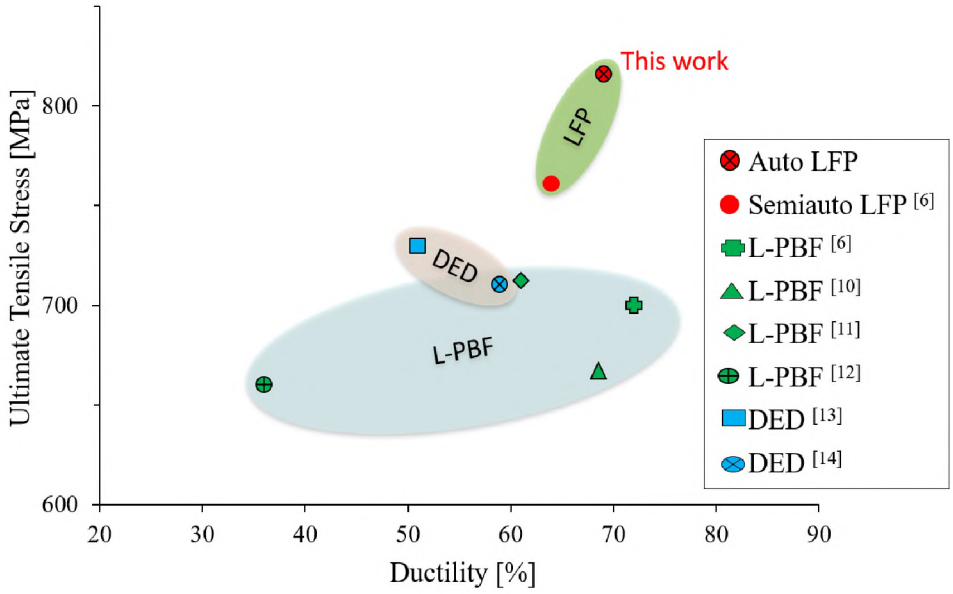

Figure 8. Ultimate tensile strength vs. ductility of 304 SS parts fabricated by LFP, L-PBF and DED processes.

4. CONCLUSION

In this paper we have presented the development of a fully automated system for the Laser Foil Printing (LFP) process and experimental studies using this additive manufacturing system to fabricate 304L SS parts with metal foil as the feedstock. The elevated edges caused by UV laser cutting were removed by mechanical polishing to prevent foil burning during the IR laser pattern welding process in the building of each layer. To study the dimensional accuracy of parts fabricated by the LFP system, one rectangular plate with an internal channel and another rectangular plate with notches and rounded edges were fabricated by this system. To study the dimension accuracy of LFP fabricated parts, linear dimensions, radius of rounded edge, and angles of notches of two representative parts were measured by optical microscopy. The yield strength, ultimate

tensile strength, and ductility were measured using standard tensile tests with miniature specimens. The measured results were compared with those available from the literature for the Laser Powder Bed Fusion (L-PFB) and Directed Energy Deposition (DED) processes. The comparisons showed that the LFP process fabricates parts with higher ultimate tensile strength and comparable ductility in comparison to the L-PBF and DED processes.

ACKNOWLEDGEMENTS

This research work was supported by the Department of Energy [grant number DE-FE0012272] and by the Intelligent Systems Center at the Missouri University of Science and Technology.

REFERENCES

[1] Schmidt, M., Merklein, M., Bourell, D., Dimitrov, D., Hausotte, T., Wegener, K., Overmeyer, L., Vollertsen, F., Levy, G.N., 2017, Laser Based Additive Manufacturing in Industry and Academia, CIRP Annals – Manufacturing Technology, 66(2):561-583.

[2] Jerrard, P.G.E., Hao, L., Dadbakhsh, S., Evans, K.E., 2010, Consolidation Behavior and Microstructure Characteristics of Pure Aluminum and Alloy Powders Following Selective Laser Melting Processing, Proceedings of the 36th International MATADOR Conference. pp.487-490.

[3] Mower TM, Long MJ (2016) Mechanical behavior of additive manufactured, powder-bed laser-fused materials. Materials Science and Engineering A, 651, pp.198–213.

[4] Behdani, B., Senter, M., Mason, L., Leu, M.C., Park J., 2020, Numerical Study on the Temperature-Dependent Viscosity Effect on the Strand Shape in Extrusion-Based Additive Manufacturing, Journal of Manufacturing and Materials Processing, 4(2), 46.

[5] Thomas, D.S., Gilbert, S.W., 2014, Costs and Cost Effectiveness of Additive Manufacturing, NIST Special Publication 1176.

[6] Hung, C.H., Sutton, A., Li, Y., Shen, Y., Tsai, H.L., Leu, M.C., 2019, Enhanced Mechanical Properties for 304L Stainless Steel Parts Fabricated by Laser-Foil-Printing Additive Manufacturing, Journal of Manufacturing Processes, 45:438–446.

[7] Hung, C.H., Chen, W.T., Sehhat, M.H., Leu, M.C., 2021, The Effect of Laser Welding Modes on Mechanical Properties and Microstructure of 304L Stainless Steel Parts Fabricated by Laser-Foil-Printing Additive Manufacturing, International Journal of Advanced Manufacturing Technology. 112:867-877.

[8] Li Y., Shen Y, Hung C.H., Leu M.C., Tsai H.L., 2018, Additive Manufacturing of Zr-Based Metallic Glass Structures on 304 Stainless Steel Substrates via V/Ti/Zr Intermediate Layers. Materials Science and Engineering: A, 729:185-195.

[9] Kolhatkar, A., Karthik, V., Chaitanya, G., Kumar, A., Ramchandran, D., 2019, Development and Validation of a Miniature Tensile Specimen for Determination of Mechanical Properties, Journal of Testing and Evaluation, 47(5):3417-3431.

[10] Ho, J., Chen, W., Chen, Z., Zhang, K., Huang, A., 2020, Microstructure, Tensile Properties and Mechanical Anisotropy of Selective Laser Melted 304L Stainless Steel, Journal of Materials Science & Technology, 48:63–71.

[11] Nguyen, Q.B., Zhu, Z., Ng, F.L., Chua, B.W., Nai, S.M.L., Wei, J., 2019, High Mechanical Strengths and Ductility of Stainless Steel 304L Fabricated Using Selective Laser Melting, Journal of Materials Science & Technology, 35(2):388–394.

[12] Ghayoor, M., Lee, K., He, Y., Chang, C.H., Paul, B.K., Pasebani, S., 2020, Selective Laser Melting of 304L Stainless Steel: Role of Volumetric Energy Density on the Microstructure, Texture and Mechanical Properties, Additive Manufacturing, 32, 101011.

[13] Smith, T.R., Sugar, J.D., Marchi, C.S., Schoenung, J.M., 2017, Orientation Effects on Fatigue Behavior of Additively Manufactured Stainless Steel, Proceedings of ASME 2017 Pressure Vessels and Piping Conference, Waikoloa, Hawaii.

[14] Griffith, M.L., Ensz, M.T., Puskar, J.D., Robino, C.V., Brooks, J.A., Philliber, J.A., Smugeresky, E., Hofmeister, W.H., 2000, Understanding the Microstructure and Properties of Components Fabricated by Laser Engineered Net Shaping (LENS), MRS Proceedings, 625.

[15] Pujula, M., Sánchez-Rodríguez, D., Lopez-Olmedo, J.P., Farjas, J., Roura, P., 2016, Measuring Thermal Conductivity of Powders with Differential Scanning Calorimetry, Journal Thermal Analysis and Calorimetry, 125:571–577.

[16] Gil, F.J., Ginebra, M.P., Manero, J.M., Planell, J.A., 2001, Formation of α-Widmanstätten Structure: Effects of Grain Size and Cooling Rate on the Widmanstätten Morphologies and on the Mechanical Properties in Ti6Al4V Alloy, Journal of Alloys and Compounds, 329:142–152.

SECTION

2. CONCLUSIONS AND FUTURE WORK

2.1. CONCLUSIONS

In this dissertation, 304L stainless steel and Al-1100 aluminum alloy parts were fabricated by the Laser Foil Printing (LFP) additive manufacturing process. The LFP process parameters for both 304L SS and Al-1100 materials were investigated and were used to fabricate dense parts with high strength and ductility. The parts' mechanical properties, microstructure, grain structure, and porosity were characterized, analyzed, and compared with those of parts fabricated by the Laser Powder Bed Fusion (L-PBF) process. The main results are summarized below:

1. The tensile test results show that LFP fabricated parts have higher strength than L-PBF fabricated parts due to the higher cooling rate of melt pool. Because of higher thermal conductivity of metal foil vs. metal powder, the melt pool has faster cooling in LFP, forming finer grains during the solidification process. As a result, the strength of LFP parts was found to be 10~15% higher than the strength of L-PBF parts. The oxygen content of LFP parts measured was 75% lower than that of L-PBF parts due to the ~10 times difference in surface area per unit volume between powder and foil.

2. Highly dense (relative density > 99%) Al-1100 aluminum alloy parts can be fabricated by the LFP process with proper process parameters. The strength of those LFP fabricated Al-1100 parts was found to be higher than annealed

aluminum parts. The electron backscattered diffraction maps of LFP fabricated Al-1100 parts showed low-angle-grain-boundary subgrains formed within high-angle-grain-boundary grains due to the fast cooling of the LFP process. The dominant grain growth in the LFP of Al-1100 aluminum alloy was {001}.

3. 304L SS parts fabricated by LFP with conduction-mode and keyhole-mode laser welding were characterized and compared. Their cross-sectional views show that the parts fabricated in the keyhole mode had higher porosity (0.5% vs. 0.1%) than those fabricated in the conduction mode. Pores in keyhole-mode welding parts were usually found at the bottom of solidified melt pool because collapse of melt-pool wall occurred only in keyhole-mode laser welding. Based on ANOVA analysis, their yield strength and ultimate tensile strength were comparable while the ductility of conduction-mode specimens was 23% higher than that of keyhole-mode welding specimens in the layer building direction, which is due to difference in their grain structures. The electron backscattered diffraction maps showed that the conduction-mode grains had lower grain boundary interface density in the layer building direction than the keyhole-mode grains, which promotes dislocation movement along the layer building direction in the conduction-mode welding.

4. The development of a fully automated LFP system and experimental studies with this system have shown that 304L SS parts with various geometries can be fabricated by the automated LFP system. The elevated edges generated due to UV laser cutting were removed by mechanical polishing after fabricating

each year, in order to prevent the supply foil from burning in the IR laser patterning process in building the next layer. The dimensions of the fabricated parts were measured and confirmed to be accurate. The part's mechanical properties were measured and compared with numbers available from existing literature for the Laser Powder Bed Fusion (L-PBF) and Direct Energy Deposition (DED) processes. The results indicated that the LFP parts have higher strength and comparable ductility compared with those parts fabricated by the L-PBF and DED technologies.

2.2. FUTURE WORK

Extensive studies are still needed in order to fully understand the processability of LFP for different metals (e.g., Ti6Al4V titanium alloys, IN718 inconel alloys, AA-6061 and AA-7075 aluminum alloys) that are popularly used in industrial and aerospace applications.

To further understand the effect of thermal conductivity difference on the creation and solidification of melt pools between using powder and using foil as the feedstock, measurements of cooling rates during the LFP and L-PBF processes in layer building are needed, which can be done using a high-speed thermal camera. The finite element method of analysis can be used to simulate the thermal history of melt-pool heating and cooling and compare the simulation results with the experimental data.

The process parameters of LFP including laser power, scan strategy, scan speed, hatch space, etc. could alter the heating-and-cooling thermal history, which may generate thermally induced residual stresses in the LFP-fabricated parts. To understand the

relations among residual stress, thermal history, and process parameters, finite element analysis could be used to select proper process parameters to minimize residual stresses. The residual stresses resulted from different process parameters can be measured experimentally by X-ray diffraction methodology and compare with predictions from finite element analysis.

In the current LFP automation system, a mechanical polisher is used to remove the elevated edges resulted from laser cutting in order to automatically build the part layer by layer. Mechanical polishing is a relatively time-consuming way to remove the elevated edges, which could be explored by use of laser polishing using one of the lasers in the existing LFP system to increase the efficiency of layer building.

BIBLIOGRAPHY

[1] Frazier WE, Polakovics D, Koegel W. Qualifying of metallic materials and structures for aerospace applications. JOM 2001;53:16–8.

[2] Thijs L, Verhaeghe F, Craeghs T, Humbeeck J Van, Kruth JP. A study of the microstructural evolution during selective laser melting of Ti-6Al-4V. Acta Mater. 2010;58:3303–12.

[3] ASTM F2792, Standard Terminology for Additive Manufacturing Technologies, ASTM, 2014.

[4] Yap CY, Chua CK, Dong ZL, Liu ZH, Zhang DQ, Loh LE, Sing SL. Review of selective laser melting: materials and applications. Appl Phys Rev. 2015;2:0411011.

[5] Shen Y, Li Y, Chen C, Tsai HL. 3D printing of large, complex metallic glass structures. Mater Des. 2017;117:213-22.

[6] Chen C, Shen Y, Tsai HL. A Foil-Based Additive Manufacturing Technology for Metal Parts. J Manuf Sci Eng. 2016;139:024501-1-6.

[7] Li Y, Shen Y, Leu MC, Tsai HL. Mechanical properties of Zr-based bulk metallic glass parts fabricated by laser-foil-printing additive manufacturing. J. Mater. Sci. Eng. A. 2019;743:404-11.

[8] Li Y, Shen Y, Chen C, Leu MC, Tsai HL. Building metallic glass structures on crystalline metal substrates by laser-foil-printing additive manufacturing. J. Mater. Process Tech. 2017;248:249–61.

[9] Li Y, Shen Y, Leu MC, Tsai HL. Building Zr-based metallic glass part on Ti-6Al-4V substrate by laser-foil-printing additive manufacturing. J. Mater. Process Tech. 2017;248:249–61.

[10] Li Y, Shen Y, Hung CH, Leu MC, Tsai HL. Additive manufacturing of Zr-based metallic glass structures on 304 stainless steel substrates via V/Ti/Zr intermediate layers. J. Mater. Sci. Eng. A. 2018;729:185–195.

[11] Kwok CT, Lo KH, Chan WK, Cheng FT, Man HC. Effect of laser surface melting on intergranular corrosion behaviour of aged austenitic and duplex stainless steels. Corros. Sci. 2011;53:1581–91.

[12] Abd-Elghany K, Bourell DL. Property evaluation of 304L stainless steel fabricated by selective laser melting. Rapid Prototyping. 2012;18:420-8.

[13] Nguyen QB, Zhu Z, Ng FL, Chua BW, Nai SML Wei J. High mechanical strengths and ductility of stainless steel 304L fabricated using selective laser melting. J. Mater. Sci. Technol. 2019;35:388-94.

[14] Ghayoor M, Lee K, He Y, Chang CH, Paul BK, Pasebani S. Selective laser melting of 304L stainless steel: role of volumetric energy density on the microstructure, texture and mechanical properties. Addit. Manuf. 2020;32:101011.

[15] Hou J, Chen W, Chen Z, Zhang K, Huang A. Microstructure, tensile properties and mechanical anisotropy of selective laser melted 304L stainless steel. J. Mater. Sci. Tech. 2020;48:63–71.

[16] Li R, Liu J, Shi Y, Wang L, Jiang W. Balling behavior of stainless steel and nickel powder during selective laser melting process. Adv. Mfg. Tech. 2012;59:1025–35.

[17] Spierings AB, Levy G. Comparison of density of stainless steel 316L parts produced with selective laser melting using different powder grades. Proc. SFF Sym. 2009:324-53.

[18] Graves RS, Kollie TG, McElroy DL, Gilchrist KE. The thermal conductivity of AISI 304L stainless steel. Int. J. Thermophys. 1991;12:409–15.

[19] Rombouts M, Froyen L, Gusarov A V., Bentefour EH, Glorieux C. Photopyroelectric measurement of thermal conductivity of metallic powders. J. Appl. Phys. 2005;97:1–9.

[20] Pujula M, Sánchez-Rodríguez D, Lopez-Olmedo JP, Farjas J, Roura P. Measuring thermal conductivity of powders with differential scanning calorimetry. J. Therm. Anal. Calorim. 2016;125:571–7.

[21] Liu Y, Yang Y, Mai S, Wang D, Song C. Investigation into spatter behavior during selective laser melting of AISI 316L stainless steel powder. Mater. Des. 2015;87:797–806.

[22] Wang L, Pratt P, Felicelli SD, El Kadiri H, Berry JT, Wang PT, Horstemeyer MF. Pore Formation in Laser-Assisted Powder Deposition Process. J. Mfg. Sci. Eng. 2009;131:51008.

[23] Campbell F.C. Manufacturing technology for aerospace structural materials. 2006.

[24] Hirsch J. Recent development in aluminum for automotive applications. T. Nonferr. Metal. S. O. C. 2014;24:1995-2002.

[25] Zhang H., Zhu H., Qi T., Hu Z., Zeng X. Selective laser melting of high strength Al-Cu-Mg Alloys: Processing, microstructure and mechanical properties. Mater. Sci. Eng. A. 2016;656:47-54.

[26] Gu T., Chen B., Tan C., Feng J. Microstructure evolution and mechanical properties of laser additive manufacturing of high strength Al-Cu-Mg alloy. Opt. Laser. Technol. 2019;112:140-50.

[27] Zhang J., Song B., Wei Q., Bourell D., Shi Y. A review of selective laser melting of aluminum alloys: processing microstructure, property and developing trends. J. Mater. Sci. Technol. 2019;35:270-84.

[28] Dinda G.P., Dasgupta A.K., Bhattacharya S., Natu H., Dutta B., Mazumder J. Microstructural Characterization of Laser-Deposited Al 4047 alloy. Metall. Mater. Trans. A. 2013;44:2233-42.

[29] Chen B., Moon S.K., Yao X., Bi G., Shen J., Umeda J., Kondoh K. Comparison study on additive manufacturing and powder metallurgy AlSi10Mg alloys. J.O.M. 2018;70:644-9.

[30] Kempen K., Thijs L., Humbeeck J.V., Kruth J.P. Processing AlSi10Mg by selective laser melting: parameter optimization and material characterization. Mater. Sci. Technol. 2015;31:917-23.

[31] Thijs L., Kempen K., Kruth J.P., Humbeeck J.V. Fine-structured aluminum products with controllable texture by selective laser melting of pre-alloyed AlSi10Mg powder. Acta Mater. 2013;61:1809-19.

[32] Rana R.S., Purohit R., Das S. Reviews on the influence of alloying elements on the microstructure and mechanical properties of aluminum alloys and aluminum alloy composites. Int. J. Sci. Res. Publ. 2012;2:1-7.

[33] Olakanmi E.O. Selective laser sintering/melting (SLS/SLM) of pure Al, Al-Mg, and Al-Si powders: effect of processing conditions and powder properties. J. Mater. Process. Technol. 2013;213:1387-405.

[34] Jerrard P.G.E., Hao L., Dadbakhsh S., Evans K.E. Consolidation behavior and microstructure characteristics of pure aluminum and alloy powders following selective laser melting processing. Proc of the 36th Int MATADOR Conf. 2010.

[35] Torkamany MJ, Malek Ghaini F, Poursalehi R, Kaplan AFH. Combination of laser keyhole and conduction welding: Dissimilar laser welding of niobium and Ti-6Al-4V. Optics and Lasers in Engineering 2016;79:9–15.

[36] Steen W., Mazumder J. (2010) Basic Laser Optics. In: Laser Material Processing. Springer, London.

[37] Steen W., Mazumder J. (2010) Laser Welding. In: Laser Material Processing. Springer, London.

[38] Guo SH, Zou JL, Xiao RS. Characterizations of welding mode transformation process during 1- μ m and 10- μ m laser welding. AIP Advances 2020;10.

[39] Lee JY, Ko SH, Farson DF, Yoo CD. Mechanism of keyhole formation and stability in stationary laser welding. Journal of Physics D: Applied Physics 2002;35:1570–6.

[40] Verhaeghe F, Craeghs T, Heulens J, Pandelaers L. A pragmatic model for selective laser melting with evaporation. Acta Materialia 2009;57:6006–12.

[41] Metelkova J, Kinds Y, Kempen K, de Formanoir C, Witvrouw A, Van Hooreweder B. On the influence of laser defocusing in Selective Laser Melting of 316L. Additive Manufacturing 2018;23:161–9.

[42] Yang J, Han J, Yu H, Yin J, Gao M, Wang Z, Zeng X. Role of molten pool mode on formability, microstructure and mechanical properties of selective laser melted Ti-6Al-4V alloy. Materials and Design 2016;110:558–70.

[43] King WE, Barth HD, Castillo VM, Gallegos GF, Gibbs JW, Hahn DE, Kamath C, Rubenchik AM. Observation of keyhole-mode laser melting in laser powder-bed fusion additive manufacturing. Journal of Materials Processing Technology 2014;214:2915–25.

[44] Zafari A, Xia K. High Ductility in a fully martensitic microstructure: a paradox in a Ti alloy produced by selective laser melting. Materials Research Letters 2018;6:627–33.

VITA

Chia-Hung Hung was born on August 9th, 1989 in the New Taipei City, Taiwan. He earned his Bachelor degree of Science in June 2011and his Master degree of Science in July 2014 in Mechanical Engineering at National Taiwan University of Science and Technology. During his studies in Master degree at National Taiwan University of Science and Technology, he received the scholarship from Ministry of Education of Taiwan to sponsor him to conduct advanced laser micromachining research under Dr. Hai-Lung Tsai's supervision as a visiting graduate student from 2013-2014 in Mechanical Engineering at Missouri University of Science and Technology.

After receiving Research Assistantship from Dr. Ming C. Leu to pursue his Ph.D. in Mechanical Engineering at Missouri University of Science and Technology, Chia-Hung started conducting research in newly developed additive manufacturing, called Laser Foil Printing in 2016. He learned wide-ranging experiences in process parameter optimization, material characterization, and process automation in Laser Foil Printing additive manufacturing.

In May of 2021, Chia-Hung received his Ph.D. in Mechanical Engineering under the supervision of Dr. Ming C. Leu at the Missouri University of Science and Technology, Rolla, MO, USA.